



**Universidad Autónoma de Madrid**

**Facultad de Ciencias**

**Departamento de Física Aplicada**

**Hybrid nanostructures for applications in  
photonics: photovoltaic and light-sensing devices**

*By*

*Rehab Ramadan Shehata*

*Supervisor: Raúl José Martín Palma*

*A thesis submitted for a degree of doctor of philosophy*

*Madrid, 2022*



Universidad Autónoma  
de Madrid



# Contents

<b>Contents</b>	<b>I</b>
<b>Acknowledgement</b>	<b>V</b>
<b>Abstract</b>	<b>VII</b>
<b>Resumen</b>	<b>VIII</b>
<b>Global summary and outline</b>	<b>IX</b>
<b>Candidate's contributions to the published manuscripts</b>	<b>XIII</b>
<b>1. General introduction</b>	<b>XVII</b>
<b>1.1. Energy bandgap of semiconductor materials and Light trapping</b>	<b>1</b>
<b>1.2. Crystalline silicon and photodetection applications</b>	<b>2</b>
<b>1.3. Nanomaterials and hybrid nanostructures for enhancing optoelectronic behavior</b>	<b>3</b>
1.3.1. Fundamentals of nanostructured porous silicon	3
1.3.2. Noble metal nanoparticles for light trapping applications	5
1.3.3. Hybrid materials and photovoltaic properties	6
<b>1.4. References related to general introduction</b>	<b>9</b>
<b>1.5. Abbreviations in the general introduction</b>	<b>12</b>
<b>2. Effect of electrolyte pH value and current density on the electrodeposition of silver nanoparticles into porous silicon</b>	<b>13</b>
<b>1 Introduction</b>	<b>14</b>
<b>2 Experimental</b>	<b>15</b>
2.1 Fabrication of nanoporous silicon layers	15
2.2 Infiltration of AgNPs into nanoPS	15
2.3 Morphological Characterization	15
2.4 Optical Reflectance Measurement	15
<b>3 Experimental results</b>	<b>16</b>
3.1 Morphology	16
3.1.1 Effect of the electrolyte pH value	16
3.1.2 Effect of the infiltration current density	17
3.2 Optical behavior	18
<b>4 Conclusions</b>	<b>19</b>
<b>References</b>	<b>20</b>

photovoltaic devices	50
<b>Introduction</b>	<b>51</b>
<b>Experimental</b>	<b>52</b>
Fabrication of the active nanoPS layers	52
Infiltration of AgNPs	53
Spin coating of TiO <sub>2</sub> thin films	53
Fabrication of Au micropatterned top contact by UV Lithography	53
Characterization techniques	53
<b>Experimental results</b>	<b>54</b>
<b>Morphology</b>	<b>54</b>
<b>Optical properties</b>	<b>54</b>
Reflectance spectra	54
<b>Determination of the bandgap of the TiO<sub>2</sub> thin films</b>	<b>56</b>
<b>Energy band diagrams</b>	<b>57</b>
<b>Photovoltaic properties</b>	<b>58</b>
Photocurrent response characterization	58
Current-voltage characterization under illumination	59
<b>Conclusions</b>	<b>61</b>
<b>References</b>	<b>61</b>
<b>Abbreviations in chapter 5</b>	<b>64</b>
<b>6. Self-powered broadband hybrid organic-inorganic photodetectors based on     PEDOT:PSS and silicon micro-nanostructures</b>	<b>65</b>
<b>1. Introduction</b>	<b>66</b>
<b>2. Experimental</b>	<b>67</b>
<b>2.1 Electrochemical etching of nanoPS layer</b>	<b>67</b>
<b>2.2 Fabrication of (Si+nanoPS micro-arrays) structures</b>	<b>67</b>
<b>2.3 Spin coating of PEDOT:PSS thin films</b>	<b>67</b>
<b>2.4 Device configurations</b>	<b>67</b>
<b>2.5 Characterization techniques</b>	<b>68</b>
<b>3. Results and discussion</b>	<b>69</b>
<b>3.1 Morphological characterization</b>	<b>69</b>
<b>3.2 Optical behaviour</b>	<b>70</b>
<b>3.3 Electrical conduction and carrier transport characteristics</b>	<b>70</b>

<b>3.4 Optoelectronic properties and photoresponse</b>	<b>72</b>
<b>3.4.1 Current- voltage characteristic under illumination</b>	<b>72</b>
<b>3.4.2 Energy band diagrams</b>	<b>72</b>
<b>3.4.3 Time-dependent photoresponse analysis</b>	<b>73</b>
<b>3.4.4 Spectral responsivity</b>	<b>75</b>
<b>4. Conclusions</b>	<b>77</b>
<b>References</b>	<b>77</b>
<b>Abbreviations in chapter 6</b>	<b>79</b>
<b>General conclusions</b>	<b>80</b>
<b>Conclusiones generales</b>	<b>82</b>
<b>Future investigation</b>	<b>86</b>
<b>List of publications included in the Thesis</b>	<b>87</b>
<b>Publications not included in the Thesis</b>	<b>88</b>

## **Acknowledgement**

*This dissertation would not have been possible without the guidance and the help of several individuals who in one way or another contributed and extended their valuable assistance in the preparation and completion of this study.*

*Primarily, my utmost gratitude to my supervisor Prof. Raúl J. Martín-Palma whose sincerity and encouragement I will never forget, kindness, help, scientific contributions with researchers from different places and guided me to complete this research work. In addition, I want to deeply thank Prof. Miguel Manso Silvan (my tutor) for his assistance to start working in the lab and for his always help to learn new experiments. I could not start my work in UAM without his support and encouragement. My deep thanks to Prof. Kamal Abdelhady, Minia University, Egypt. He was my supervisor in the master degree and my co-supervisor in my PhD thesis. Nevertheless, he was died before defending my thesis. He was very kind and helpful, not only with me but with my family too. Other thanks to Prof. Vicente Torres Costa for his cooperation and guidance during the optoelectronic measurements. From Spain to the USA, I would like to thank prof. Akhlesh Lakhtakia, department of Materials Science and Engineering, Pennsylvania State University for his contribution to characterizing my samples in his lab.*

*Special gratitude to every party that contributed to the financing of my research project to obtain my PhD degree from UAM University. I am indebted to the Egyptian Ministry of Higher Education, Missions Section for their support to start my PhD project. In addition, my great thanks to UAM University for the financial support through the predoctoral FPI-UAM grant to complete my research project.*

*Technical assistance is the basis of scientific research. I will never forget the technical assistance that Luis gave me. He is a genius person who loves his work and is quick to respond to all of us with his wonderful ideas. Not only Luis, but also Dr Valentine, who contributed significantly to the completion of this work through technical assistance.*

## *Acknowledgement*

---

*A special thanks to my workmates, Chloe, Paola, Ruth, Nelson, Inma, Rodrigo, Gabriel and Emma for their respect, kind and cooperation during the work. Other thanks to the friends who I met in Spain, Shreen, Khaola, Marito, Rania, Nourhan, Susan, Shrouk and a special thanks to Hala. She is like my sister. Thanks, Hala for your encouragement and helps to finish work papers. I hope you will defend your thesis soon.*

*Last but not the least; I would like to thank all my family. My parents, thanks to you for everything you offered to me " God bless you all the time". My brothers and sisters (Medhat, Negm, Nema, Abdelrahman and Shahd), thanks for your love, help, advice and encouragement. I give special thanks to my husband Mahmoud for his patience, assistance and encouragement. My little son Abdallah, you are the best thing in my life. Thank you for giving me the time to work.*

## **Hybrid nanostructures for applications in photonics: photovoltaic and light-sensing devices**

### **Abstract**

Subwavelength nanostructures are of great interest for the manipulation of the effective refractive index of the materials used in photonic and plasmonic devices. In the current work, we decided to explore the use of nanostructured porous silicon (nanoPS) and hybrid nanostructures aiming at enhancing the optoelectronic properties of photonic devices based on silicon. First, we fabricated nanoPS and hybrid nanostructures of nanoPS combined with Ag metallic nanoparticles (nanoPS+AgNPs) onto silicon substrates. The optical characteristics as functions of the wavelength, angle of incidence, and polarization state of incident light were studied. The experimental results show a broadband optical absorption characteristic of the hybrid layers, which will be useful in light-harvesting devices. In addition, an accurate determination of the electrical properties of Si-based metal–insulator–semiconductor (MIS) Schottky barrier diodes was carried out. The results show a remarkable improvement in the performance of the MIS Schottky barrier diodes upon the addition of hybrid nanoPS layers with embedded Ag nanoparticles, opening the way to their use as photovoltaic devices. The key performance parameters of the MIS Schottky-junction solar cells were determined. A remarkable enhancement in the overall performance of the solar cells upon the addition of nanoPS and AgNPs layers to the basic structure is observed.

From another perspective, hybrid organic-inorganic self-powered photodetectors with three different configurations were fabricated and their optoelectronic performance was determined. In these devices, poly(3,4-ethylenedioxythiophene) polystyrene sulfonate (PEDOT:PSS) is the organic layer and the inorganic layer is based on Si. The performance of the devices was greatly improved by modifying the structure of the active layer to be Si+nanoPS micro-arrays instead of single nanoPS layers or flat Si layers. This improved behavior is associated to the combined effect of an effective reduction of the reflectance due to the presence of nanoPS and an improvement of the electrical conduction given by the presence of heavily-doped Si regions.

## **Nanoestructuras híbridas para aplicaciones en fotónica: dispositivos fotovoltaicos y sensores de luz**

### **Resumen**

Las nanoestructuras con dimensiones inferior que la longitud de onda son de gran interés para la manipulación del índice de refracción efectivo de los materiales utilizado en dispositivos fotónicos y plasmónicos. En este trabajo, decidimos explorar el uso de silicio poroso nanoestructurado (nanoPS) y nanoestructuras híbridas con el objetivo de mejorar las propiedades optoelectrónicas de varios dispositivos fotónicos basados en silicio. Primero, fabricamos silicio poroso nanoestructurado (nanoPS) y nanoestructuras híbridas de nanoPS combinadas con nanopartículas metálicas Ag (nanoPS + AgNP) sobre sustratos de silicio. Se estudiaron las características ópticas en función de la longitud de onda, el ángulo de incidencia y el estado de polarización de la luz incidente. Los resultados experimentales muestran una característica de absorción óptica de banda ancha de las estructuras híbridas, que será útil en dispositivos de captación de luz. Además, se llevó a cabo la determinación precisa de las propiedades eléctricas de los diodos de barrera Schottky de metal-aislante-semiconductor (MIS). Los resultados muestran una mejora notable en el rendimiento de los diodos de barrera MIS Schottky tras la adición de capas nanoPS híbridas con nanopartículas de Ag integradas, abriendo el camino para su uso como dispositivos fotovoltaicos. Se determinaron los parámetros clave de rendimiento de las células solares de unión Schottky MIS. Se observó una mejora notable en el rendimiento general de las células solares tras la adición de capas nanoPS y AgNPs a la estructura básica.

Desde otra perspectiva, se fabricaron fotodetectores híbridos orgánicos-inorgánicos autoamplificados con tres configuraciones diferentes y se determinó su rendimiento optoelectrónico. En estos dispositivos, PEDOT: PSS es la capa orgánica y la capa inorgánica se basa en Si. El rendimiento de los dispositivos mejoró en gran medida al modificar la estructura de la capa activa para que sean micromatrices Si+nanoPS en lugar de capas de nanoPS individuales o capas planas de Si. Este comportamiento mejorado está asociado al efecto combinado de una reducción efectiva de la reflectancia debido a la presencia de nanoPS y una mejora de la conducción eléctrica dada por la presencia de regiones de Si fuertemente dopadas.



## **Global summary and outline**

Nanostructured porous silicon (nanoPS) shows many additional properties beyond photo- and electro-luminescence, which have led to several successful applications in different fields ranging from microelectronics to biomedicine [1]. NanoPS can be described quite simply as an amorphous matrix in which silicon nanocrystals are embedded [2-5]. The morphology of nanoPS depends strongly on the specific fabrication parameters, including electrolyte composition and fabrication current density [6]. The complex-valued effective refractive index of nanoPS is therefore dependent on the electrochemical fabrication parameters [7]. Control over the refractive index allows the use of nanoPS in tunable photonic structures made entirely of silicon [8]. However, two primary competing recombination mechanisms are possible after the fabrication of nanoPS on Si, namely radiative recombination through the surface states (surface recombination) and radiative recombination through oxygen vacancies [9]. This way, passivating the surface of nanoPS would lead to an enhancement of the generation of electron/hole pairs by reducing the surface recombination rates. Moreover, nanoPS shows low surface electrical conduction, most likely due to the formation of the nanopores in the heavily-doped regions of the Si substrate, leading to an effective reduction of the doping concentration [10].

Nanoparticles (NPs) of noble metals usually enhance the efficiency of photovoltaic devices by reducing reflection and increasing light trapping. However, the specific optical behavior depends on the density of NPs, as well as their shape and size [11]. In some cases, the presence of metal NPs results in high reflectivity due to a large surface density, which can reach their percolation threshold and even form a quasi-continuous thin film [12, 13]. Nevertheless, a large surface density of nanoparticles would result in improved electrical conduction.

Within this context and given the increasing attention being received by subwavelength nanostructures for photonic and plasmonic applications [14, 15], we decided to explore the use of nanoPS and Ag nanoparticles (AgNPs) in hybrid nanostructures for the development of enhanced photovoltaic devices. Furthermore, TiO<sub>2</sub> thin films are used as a passivation layer to prevent nanoPS from oxidation.

Self-powered photodetectors possess high potential for use in numerous applications in such diverse fields as optical communications, biomedicine, gas sensing, and video imaging [16]. Depending on their wavelength response, there are selective and broadband photodetectors.

Part of the present work was devoted to combine in one device the good electrical properties of Si and the optical enhancement provided by nanoPS. In this line, integrated micro-nanostructures consisting of ordered micro-arrays of nanoPS on the surface of Si, i.e., Si+nanoPS micro-arrays were fabricated for their subsequent use as self-powered photodetectors. Moreover, PEDOT:PSS layers serve at the same time as a transparent conductors, anti-reflective coatings and hole transport layers [17].

**In Chapter 2:** “Effect of electrolyte pH value and current density on the electrodeposition of silver nanoparticles into porous silicon”

Nanostructured porous silicon (nanoPS) layers effectively reduce the overall reflectance of bulk silicon, due to a reduction of the effective refractive index as a consequence of combining silicon with air. The reflectance of hybrid nanoPS+AgNPs structures can be lower than that of nanoPS due to plasmonic effects or higher if a continuous Ag layer is formed. This will depend on the size, shape and density of the infiltrated AgNPs. In this study, a combination of electrochemical etching of Si and electrodeposition of silver nanoparticles (AgNPs) for the development of hybrid structures (nanoPS+AgNPs), is presented. In particular, AgNPs with different sizes and shapes were infiltrated into nanoPS layers using different electrolyte pH values and infiltration current densities. Furthermore, the effect of the fabrication parameters on the optical properties of the nanoPS layers and the hybrid nanoPS+AgNPs structures was studied. Accordingly, this work establishes a relationship between the size and morphology of the AgNPs and the optical properties of the hybrid nanoPS+AgNPs structures. Depending on the intended application, the characteristic features of the deposited AgNPs can be optimized by setting the appropriate electrolyte pH value and infiltration current density.

**In Chapter 3:** “Hybrid nanostructured porous silicon-silver layers for wideband optical absorption”

Given the increasing attention being received by subwavelength nanostructures for photonic and plasmonic applications, the use of nanoPS and hybrid nanoPS+AgNPs layers grown onto silicon as wideband optical absorbers is explored. Therefore, it was experimentally investigated the dependence of optical absorption characteristics of nanoPS and hybrid nanoPS+AgNPs layers on the thickness and porosity of nanoPS layers and the amount of silver infiltrating the

pores of nanoPS. More specifically, the reflection and absorption characteristics of the nanoPS and hybrid nanoPS+AgNPs layers were measured as functions of the wavelength, angle of incidence, and polarization state of incident light. The experimental data show that the absorption characteristics of the hybrid nanoPS+AgNPs layers can be controlled by selecting the appropriate combination of thickness and porosity of the nanoPS layers, together with the density of infiltrant silver nanoparticles. The wideband optical absorption characteristics of the hybrid nanoPS+AgNPs layers are expected to contribute to increased efficiency of light-harvesting devices and photodetectors given by increased field-of-view for both *s*- and *p*-polarization states of incident light over a broad spectral regime.

**In Chapter 4:** “Electrical characterization of MIS Schottky barrier diodes based on nanostructured porous silicon and silver nanoparticles with applications in solar cells”

The electrical properties of photovoltaic devices are of utmost importance to predict and optimize their overall optoelectronic performance. Within this context, alternating current (AC) and direct current (DC) electrical characteristics of Si-based metal–insulator–semiconductor (MIS) Schottky barrier diodes with the basic structure Al/Si/TiO<sub>2</sub>/NiCr were studied, aiming at using them as photovoltaic devices. The basic diode structure was modified by adding nanoPS layers and by infiltrating AgNPs into the nanoPS layers, leading to Al/Si+nanoPS/TiO<sub>2</sub>/NiCr and Al/Si+nanoPS+AgNPs/TiO<sub>2</sub>/NiCr structures, respectively. The AC electrical properties were studied using a combination of electrochemical impedance spectroscopy and Mott–Schottky analysis, while the DC electrical properties were determined from current-voltage measurements. From the AC electrical characterization, an equivalent electric model was proposed. Additionally, Mott–Schottky analysis allowed the determination of such parameters as the flat-band potential, carrier doping density, and the type of the conduction (p or n). While, the DC electrical properties allowed us to determine several key diode parameters, namely reverse saturation current, ideality factor, parasitic series and shunt resistances, and barrier height.

**In Chapter 5:** “Hybrid porous silicon/silver nanostructures for the development of enhanced photovoltaic devices”

In the present work, the optoelectronic performance of the three different MIS Schottky diodes studied in the previous chapter are analyzed. The diodes include a device with the structure

Al/Si/TiO<sub>2</sub>/Au and two modified ones. The first variation includes a nanoPS layer, leading to the structure Al/Si/nanoPS/TiO<sub>2</sub>/Au, while the second one includes AgNPs embedded into the nanoPS layer, leading to the structure Al/Si/nanoPS+AgNPs/TiO<sub>2</sub>/Au. The modified devices constitute two strategies that are implemented to improve light absorption and minimizing the carrier recombination rates of flat Si.

**In Chapter 6:** ‘‘Self-powered broadband hybrid organic-inorganic photodetectors based on PEDOT: PSS and silicon micro-nanostructures’’

The main aim of this work is to combine the good electrical properties of Si and the optical enhancement provided by nanoPS in one device. In this line, integrated micro-nanostructures consisting of ordered micro-arrays of nanoPS on the surface of Si, i.e., Si+nanoPS micro-arrays, were fabricated for their subsequent use as self-powered photodetectors. Three configurations of hybrid organic-inorganic PEDOT:PSS (poly(3,4- ethylenedioxythiophene) polystyrene sulfonate)-Si self-powered photodetectors were fabricated and studied. The basic structure is Au/PEDOT:PSS/Si/Al, and two variants aimed at improving the optical performance of the devices: Au/PEDOT:PSS/nanoPS/Si/Al and Au/PEDOT:PSS/(Si+nanoPS micro-arrays)/Si/Al. The PEDOT:PSS layer serves at the same time as a transparent conductor, anti-reflective coating and hole transport layer [17], while Si, nanoPS/Si, and (Si+nanoPS micro-arrays)/Si are the photodetector active layers, respectively. The morphology, optical properties, and electrical transport properties of the three different photodetector configurations were analyzed. Furthermore, we compared their photoresponse in a wide range of incident light powers. The stability and reproducibility to pulsed light were examined at 0 V. Finally, the spectral responsivity was analyzed in a broad wavelength range.

## **Candidate's contribution to the published manuscripts listed in the thesis**

### **1- Candidate's contribution in chapter 2 "Effect of electrolyte pH value and current density on the electrodeposition of silver nanoparticles into porous silicon"**

---

- Fabricated the nanoPS and hybrid nanoPS+AgNPs layers.
- Devise the modified method for infiltration of Ag nanoparticles inside nanoPS layers.
- Managed to control the size and density of the infiltrated AgNPs.
- Acquired the FESEM and EDX analysis.
- Was in charge of the overall reflectance optical characterization.
- Prepared the first draft of the manuscript.
- Edit the manuscript according to the co-authors and referees comments.
- Wrote the first draft for the referee's response.

### **2- Candidate's contribution in chapter 3 "Hybrid nanostructured porous silicon-silver layers for wideband optical absorption"**

---

- Fabricated the nanoPS and hybrid nanoPS+AgNPs layers.
- Optimized the size of AgNPs for enhancing the optical absorption
- Acquired the FESEM images.
- Was in charge of the overall optical reflectance characterization.
- Shared with the co-authors in reviewing the manuscript.

### **3- Candidate's contribution in chapter 4 "Electrical characterization of MIS Schottky barrier diodes based on nanostructured porous silicon and silver nanoparticles with applications in solar cells"**

---

- Fabricated the nanocomposites of nanoPS and hybrid nanoPS+AgNPs layers, TiO<sub>2</sub> layer, and implementation of the three different structures of Schottky diodes.
- Acquired the FESEM images.

- Was in charge of the AC and DC electrical measurements and the fitting process of EIS results and I-V curves.
- Prepared the first draft of the manuscript.
- Edit the manuscript according to the co-authors and referees comments.
- Wrote the first draft for the referee's response.

**4- Candidate's contribution in chapter 5 "Hybrid porous silicon/silver nanostructures for the development of enhanced photovoltaic devices"**

---

- Fabricated the nanocomposites of nanoPS and hybrid nanoPS+AgNPs layers, TiO<sub>2</sub> layer, Au patterned electrode and implementation of the three different structures of photovoltaic devices.
- Come up with the idea of using TiO<sub>2</sub> thin films as passivation layers, which leads to improving the performance of the devices.
- Acquired the FESEM images.
- Was in charge of the overall reflectance optical characterization and all the optoelectronic measurements.
- Prepared the first draft of the manuscript.
- Edit the manuscript according to the co-authors and referees comments.
- Wrote the first draft for the referee's response.

**5- Candidate's contribution in chapter 6 "Self-powered broadband hybrid organic-inorganic photodetectors based on PEDOT: PSS and silicon micro-nanostructures"**

---

- Fabricated the nanoPS layers and the hybrid Si+nanoPS micro-arrays structures, spin coating of PEDOT:PSS thin films and implementation of the three different structures of organic-inorganic photodetectors.
- Devise the idea of using combined nanostructures for enhancing the broadband performance of the photodetectors.
- Acquired the FESEM images.
- Was in charge of the optical behavior of the three devices, in addition to all the electrical and optoelectronic measurements.

- Prepared the first draft of the manuscript.
- Edit the manuscript according to the co-authors and referees comments.
- Wrote the first draft for the referee's response.

## **Chapter 1:**

# **General introduction**

---



### **1. General introduction**

Photonics is the science of light. It is the technology of manipulating light by generation, emission or control [18]. Photonic technology is applicable in a variety of electronic engineering fields. For instance, photovoltaics (PVs), light-emitting diodes, optical communications, laser, optical amplifiers, smart windows and photodetectors [19].

Solar cells are mainly based on semiconductor materials, which are classified into two classes. (1) Elemental semiconductors (group IV in the periodic table), i.e. silicon, germanium, diamond, etc. (2) Compound semiconductors, i.e. IV-IV (SiC), III-V (GaAs, InP, InSb, GaN), and II-VI (CdTe, ZnS, ZnSe, etc.). Furthermore, impurities (p or n) can introduce into the intrinsic semiconductor material to improve its electrical properties, i.e boron-doped Si or phosphorus-doped Si [20-22]. Light absorption by the semiconductor materials in PV applications is one of the main requirements to obtain a high conversion efficiency.

#### **1.1. Energy bandgap of semiconductor materials and Light trapping**

Absorption of light by a semiconductor material is mainly depend on its energy bandgap ( $E_g$ ). When the energy of the incident photon equals or greater than the bandgap of the semiconductor, the photon will be absorbed and an electron will be excited into the conduction band [23]. That generation of charge carriers (electron-hole pair) is the basis of the photovoltaic effect. Moreover, semiconductor materials are divided into direct bandgap and indirect bandgap semiconductors [23]. Direct bandgap semiconductors characterized by a large absorption coefficient ( $\alpha$ ) due to the minimum of the conduction band occurs at the same wavevector ( $k$ ) as the maximum of the valence band. However, the indirect bandgap semiconductors characterized by a smaller  $\alpha$  due to the minimum of the conduction band doesn't occur at the same wavevector as the top of the valence band (conduction and valence bands are not vertically aligned) as illustrated in figure 1.1.

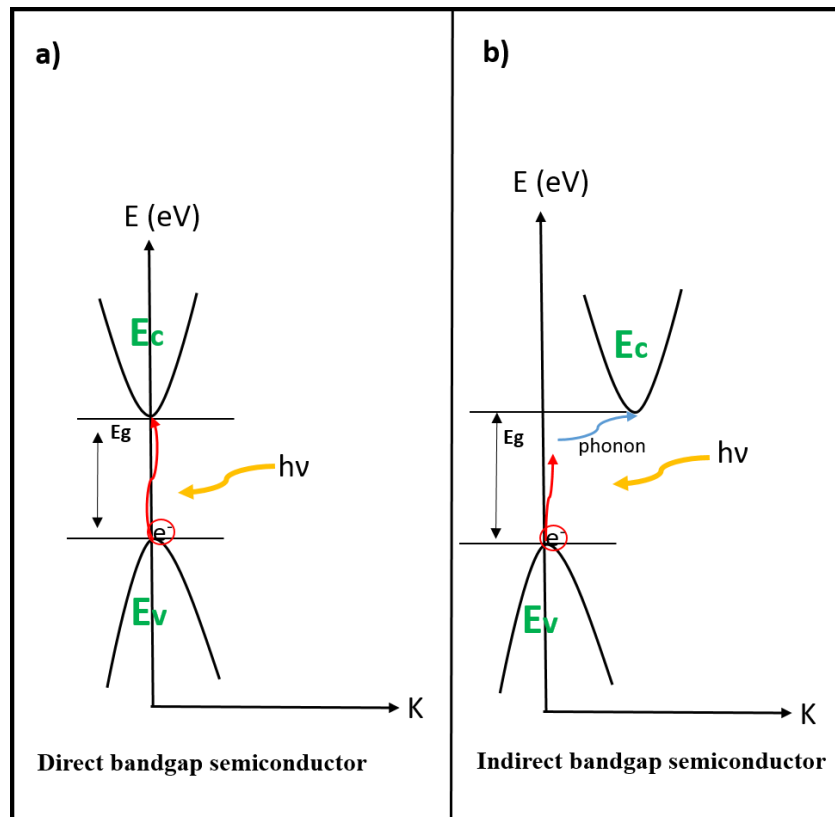


Figure 1.1. Illustration of energy band structure and light absorption. (a) Direct bandgap semiconductor. (b) Indirect bandgap semiconductor assisted with phonon absorption.

Absorption of light is larger for direct bandgap semiconductors than indirect bandgap materials. Regarding a direct bandgap semiconductor, light absorption occurs when the energy and momentum of an empty state in the conduction band equals that of an electron in the valence band plus that of the incident photon. While, for an indirect bandgap semiconductor, the energy and momentum of the empty state in the conduction band are not equal to that of an electron in the valence band plus the energy of the incident photon. As a result, light absorption needs the help of another particle, namely a phonon to cause light trapping [24].

### 1.2. Crystalline silicon and photodetection applications

Despite all the available alternatives and the intense research in the field of photodetection, silicon is likely to remain the dominant PV material for the foreseeable future, given its abundance in the earth's crust, long-term stability, well-established technology (having its

origins in the semiconductor industry), and relatively low cost [25]. However, crystalline silicon still has several drawbacks that limit its performance. These include optical losses and the indirect bandgap character of Si, which causes an increase of the carrier recombination rates [26, 27], as well as thermal and quantum losses [27]. These drawbacks can be tackled by using multi-bandgap devices or adjusting the bandgap of silicon. Multi-junctions as p-n heterojunctions, metal-semiconductor (MS) Schottky junctions and MIS Schottky junctions. A different approach to achieve an efficient photovoltaic conversion of solar energy goes through the development of MS Schottky junction solar cells based on crystalline Si, basically because of their structural simplicity and therefore convenient realization [28]. Moreover, these solar cells are inexpensive compared to solar cells based on diffused p-n junctions. Moreover, they overcome the issues related to high temperature diffusion. However, MS solar cells usually show lower conversion efficiencies compared to p-n junction solar cells of the same materials due to their typically low open-circuit voltage [29]. However, MIS junctions show increased open-circuit voltage due to tunnelling through the insulating layer of the majority carriers or diffusion current due to the minority carriers [30, 31], thus improving the overall conversion efficiency of Schottky-barrier solar cells. As for the bandgap of silicon can be adjusted by performing nanostructures on the silicon surface. In particular, various nanostructures were performed on the Si wafer surface, including Si nanowires [32-34], quantum dots [35], and porous silicon [36], as well as periodic, random, and pyramidal surface texturing [37, 38].

### **1.3. Nanomaterials and hybrid nanostructures for enhancing optoelectronic behavior**

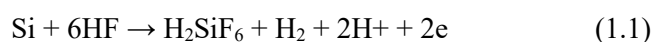
There are several number of ways that nanostructures can potentially improve the optoelectronic performance by improving light trapping. The mechanism behind the increase in light trapping by the nanostructures depends on the shape and size of the intended nanostructures [39]. This section focuses on the advantages of applying mono and hybrid nanostructures for enhancing the performance of photovoltaic devices. In more details, the nanoPS, metallic NPs, and hybrid nanostructures.

#### **1.3.1. Fundamentals of nanostructured porous silicon**

## 1. General introduction

Uhlir is the first scientist who discovered porous silicon in 1956 by chance. He was performing electropolishing experiments on silicon wafers in hydrofluoric (HF) acid electrolyte. He noticed that, under the appropriate conditions of applied current density and electrolyte composition, a nanostructured porous silicon (nanoPS) layer was produced [40]. Since then, NanoPS material was investigated as a good candidate in different fields ranging from microelectronics to biomedicine [1].

Electrochemical etching in hydrofluoric acid is one of the most common methods to perform nanoPS with different dimensions [41]. The reaction during anodization process can be expressed as:



During the pores formation, two of the four available silicon electrons participate in an interface charge transfer. While the remaining two electrons are affected by corrosive hydrogen formation. There are three classifications of porous materials according to the diameter of the pores as shown in figure 1.3. Accordingly, the size of the pores can be adjusted as a function of the applied current density (J). Where the size of the pores increases with increasing J.

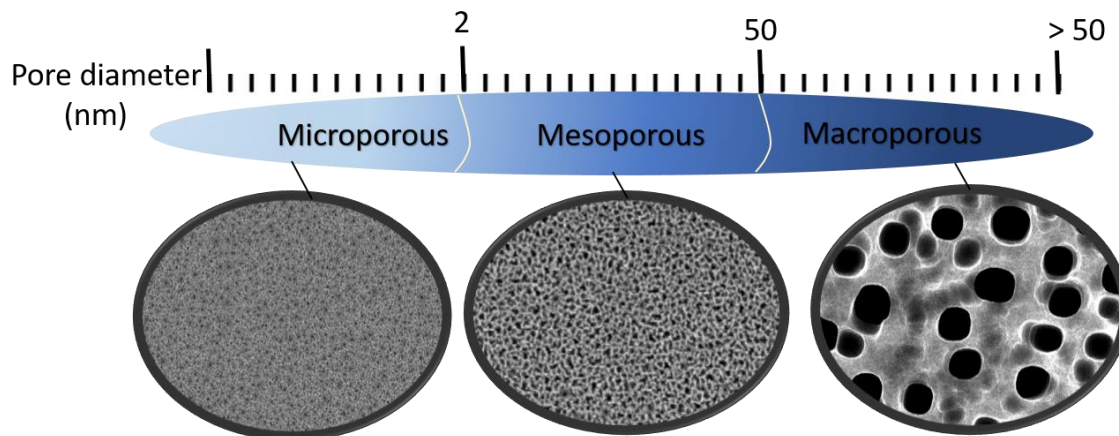


Figure 1.3. Classifications of porous materials according to the diameter of the pores.

NanoPS can be described quite simply as an amorphous matrix in which silicon nanocrystals are embedded [2-5]. The morphology and optical absorption of a nanoPS sample depends strongly on the specific fabrication parameters, including electrolyte composition and fabrication current density [6]. The complex-valued effective refractive index of nanoPS is therefore dependent on the electrochemical fabrication parameters [7]. Control over the

## ***1. General introduction***

---

refractive index allows the use of nanoPS for tunable photonic structures made entirely of silicon [8]. However, the electrical conduction decreases by creating voids in the crystal structure of Si. Moreover, nanoPS undergoes a spontaneous oxidation under ambient atmosphere, which cause a degradation of surface structures and electrical conduction over ageing [42]. In addition to two recombination mechanisms are possible after the fabrication of nanoPS on Si, namely radiative recombination through the surface states (surface recombination) and radiative recombination through the oxygen vacancies [9]. This way, passivating the surface of nanoPS leads to an enhancement of the generation of electron/hole pairs by reducing the surface recombination rates. Therefore, passivation of nanoPS surfaces stabilize the functional properties of porous silicon based devices. Chemical modification of nanoPS surface is an effective method for surface passivation. For instance by oxidation [43, 44], nitradation [45], or by halogenation processes [46]. Metals as In, Cu and Ag is an alternative method to stabilize the physical properties of nanoPS, as previously studied [47, 48]. Moreover, surface treatment by noble metal ions as Pt and Pb showed an effective way to passivate the surface of nanoPS [49].

### 1.3.2. Noble metal nanoparticles for light trapping applications

Noble metal nanoparticles (NPs) (i.e. Ag, Au, Pt) with sizes ranging from a few nanometers to several hundreds of nanometers, have properties that differ significantly from those of bulk materials [50]. The unique physical and chemical properties of noble metals NPs allow them to be exploited in a wide variety of applications in such diverse fields as biomedicine, energy harvesting and gas sensing [51-54]. In the case of low-dimension materials, these properties greatly depend on the surface to volume ratio [55]. Since NPs possess a large surface to volume ratio, their electrical, optical, and magnetic properties remarkably depart from their bulk properties [56-58]. Accordingly, the size and shape of NPs need to be precisely controlled for the target application. However, other features such as their size distribution, state of aggregation, and arrangement over a surface need also to be accurately controlled. In this regard, numerous physical and chemical methods have been developed to synthesize noble metal NPs with controlled properties [59, 60].

Nobel metal NPs usually enhance the efficiency of photovoltaic devices by reducing reflection and increasing light trapping within the device. The strong interaction between metal NPs and

light leads to an increase in the electric field around the particles. As a result, the particles effectively concentrate the light in the surrounding medium and electron-hole pair are generated. This phenomena is called surface plasmon resonance (SPR), figure 1.2.a. However, the specific optical behavior depends on the density of NPs, as well as their shape and size [11]. In some cases, the presence of metal NPs results in high reflectivity due to a large surface density of nanoparticles, which can reach their percolation threshold and even form a quasi-continuous thin film [12, 13], figure 1.2.b. Nevertheless, a large surface density of nanoparticles would result in improved electrical conduction.

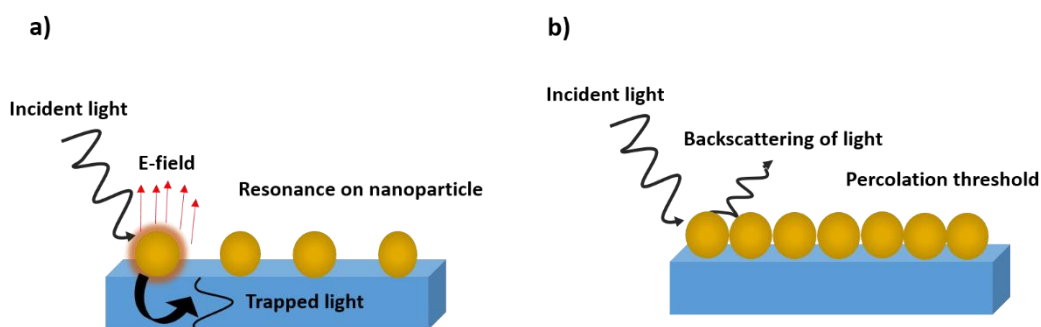
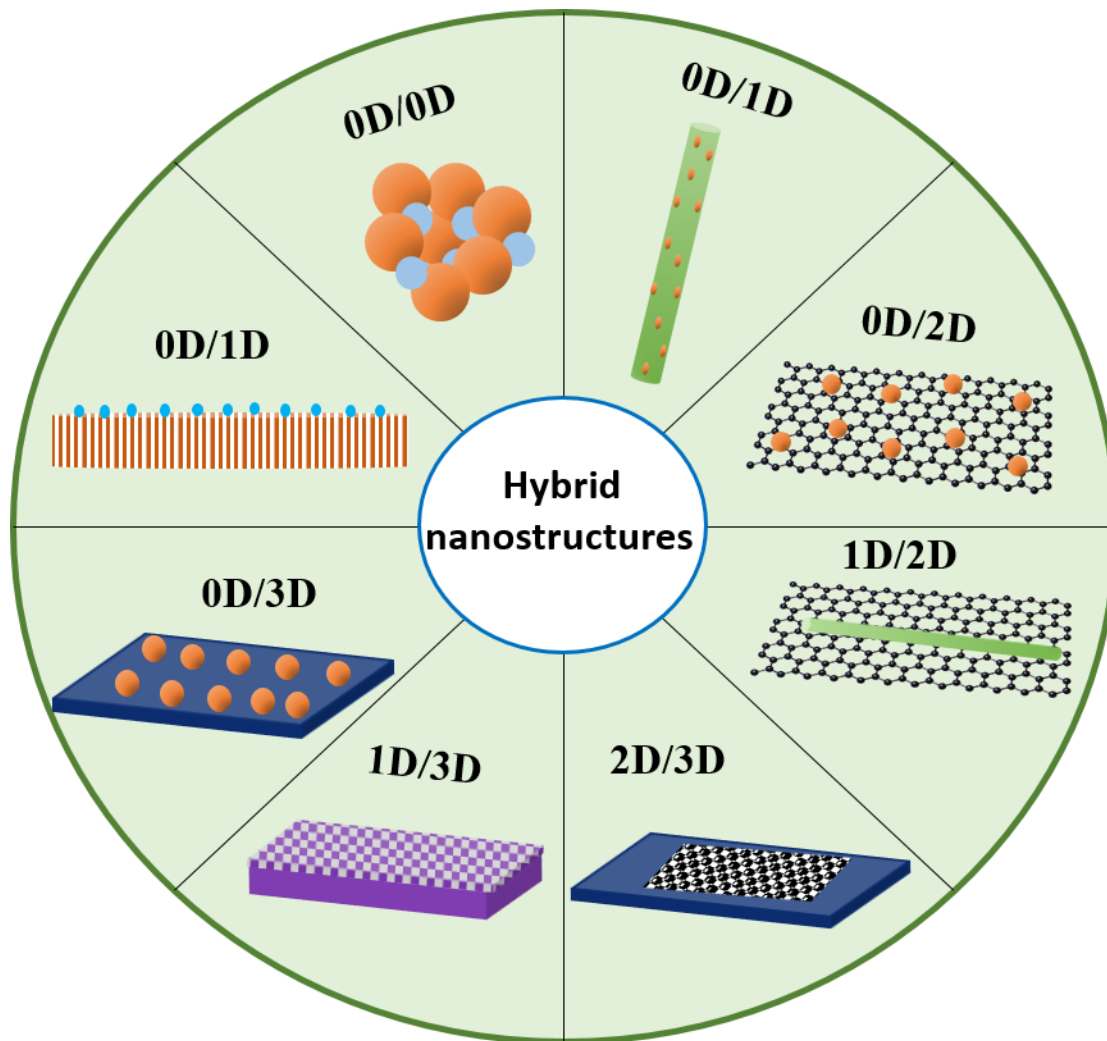


Figure 1.2. Effect of density of metal NPs on light trapping. a) Generation of SPR effect by NPs and b) Backscattering of light by the metal NPs due to percolation threshold.

### 1.3.3. Hybrid materials and photovoltaic properties

There is a wide range of materials that are used in hybrid systems to improve the optoelectronic performance of photovoltaic applications. These materials include metals nanostructures, metal oxides, organic materials, etc. The morphology of these materials is versatile. There are zero-dimensional (0D) (i.e. quantum dots or nanoparticles), one-dimensional (1D) (i.e. nanowires or nanorods), two-dimensional (2D) (i.e. nanosheets) and three-dimensional (3D) as networks or thin films [61-63][64-66]. So far, hybrid nanostructures could be an integration between 0D/1D, 1D/1D, 0D/2D, 1D/2D, 2D/2D and 3D materials, figure 1.3.



**Figure 1.3.** Schematic representation of different hybrid nanostructures suitable for enhancing optoelectronic performance of photonic devices.

Owing to the advantages of low cost, simple fabrication, compact size, and device stability, hybrid nanostructures greatly improve the optoelectronic performance of photodetectors compared with a single structure. For instance, the combination of two structures with good electrical conduction and the other has a good optical absorption leads to an integrated system combining good electrical conduction and optical absorption in the same device. As a result, an enhancement in the optoelectronic performance of the photodetectors. Another strategy is the combination between two materials and one of them contribute to passivating the surface of the other material from oxidation. This leads to an improvement in the stability of the devices. From another perspective, the combination of two nanostructures can facilitate the

## ***1. General introduction***

---

separation between charge carriers and increase the charges lifetime. As a result, an enhancement in the photodetection performance in terms of photocurrent and efficiency. Moreover, a combination of two nanostructures of different photoemission has a great effect on light-emitting diodes. In this case, broadband emission will result from the combination between two different structures, instead of narrow emission by single nanostructured material.



## 1.4. References related to general introduction

- [1] L. Canham, Handbook of porous silicon, Springer2014.
- [2] R. Martín-Palma, L. Pascual, P. Herrero, J. Martínez-Duart, Direct determination of grain sizes, lattice parameters, and mismatch of porous silicon, Applied physics letters, 81 (2002) 25-27.
- [3] R. Martín-Palma, L. Pascual, A. Landa, P. Herrero, J. Martínez-Duart, High-resolution transmission electron microscopic analysis of porous silicon/ silicon interface, Applied physics letters, 85 (2004) 2517-2519.
- [4] R. Martín-Palma, L. Pascual, P. Herrero, J. Martínez-Duart, Monte Carlo determination of crystallite size of porous silicon from x-ray line broadening, Applied Physics Letters, 87 (2005) 211906.
- [5] L. Pascual, R. Martín-Palma, A. Landa-Cánovas, P. Herrero, J. Martínez-Duart, Lattice distortion in nanostructured porous silicon, Applied Physics Letters, 87 (2005) 251921.
- [6] M.J. Sailor, Porous silicon in practice: preparation, characterization and applications, John Wiley & Sons2012.
- [7] V. Torres-Costa, R. Martín-Palma, J. Martínez-Duart, Optical constants of porous silicon films and multilayers determined by genetic algorithms, Journal of applied physics, 96 (2004) 4197-4203.
- [8] V. Torres-Costa, R. Martín-Palma, Application of nanostructured porous silicon in the field of optics. A review, Journal of materials science, 45 (2010) 2823-2838.
- [9] I. Iatsunskiy, M. Pavlenko, R. Viter, M. Jancelewicz, G. Nowaczyk, I. Baleviciute, K. Załęski, S. Jurga, A. Ramanavicius, V. Smyntyna, Tailoring the structural, optical, and photoluminescence properties of porous silicon/TiO<sub>2</sub> nanostructures, The Journal of Physical Chemistry C, 119 (2015) 7164-7171.
- [10] M. Chavarria, F. Fonthal, Electrical Investigation of Porous Silicon/p-Si Heterojunction Prepared by Electrochemical Etching, ECS Journal of Solid State Science and Technology, 5 (2016) P3172-P3175.
- [11] J. Mock, M. Barbic, D. Smith, D. Schultz, S. Schultz, Shape effects in plasmon resonance of individual colloidal silver nanoparticles, The Journal of Chemical Physics, 116 (2002) 6755-6759.
- [12] D. McLachlan, A. Priou, I. Chenerie, E. Issac, F. Henry, Modeling the permittivity of composite materials with a general effective medium equation, Journal of Electromagnetic Waves and Applications, 6 (1992) 1099-1131.
- [13] T.G. Mackay, A. Lakhtakia, Percolation thresholds in the homogenization of spheroidal particles oriented in two directions, Optics communications, 259 (2006) 727-737.
- [14] H.A. Atwater, A. Polman, Plasmonics for improved photovoltaic devices, Materials for sustainable energy: A collection of peer-reviewed research and review articles from nature publishing group, (2011) 1-11.
- [15] J. Oh, H.-C. Yuan, H.M. Branz, An 18.2%-efficient black-silicon solar cell achieved through control of carrier recombination in nanostructures, Nature nanotechnology, 7 (2012) 743-748.
- [16] H.S. Nalwa, Photodetectors and fiber optics, Elsevier2012.
- [17] J.P. Thomas, K.T. Leung, Defect-minimized PEDOT: PSS/planar-Si solar cell with very high efficiency, Advanced Functional Materials, 24 (2014) 4978-4985.
- [18] A.R. Jha, A.R. Jha, D.A. Jha, Infrared technology: applications to electrooptics, photonic devices, and sensors, Wiley New York2000.
- [19] S.L. Chuang, Physics of photonic devices, John Wiley & Sons2012.
- [20] F. Omnes, Introduction to semiconductor photodetectors, Optoelectronic Sensors, (2009) 1-14.
- [21] B. Zaidi, Introductory chapter: Introduction to photovoltaic effect, Solar Panels and Photovoltaic Materials, (2018) 1-8.
- [22] J. Nelson, The physics of solar cells, World Scientific Publishing Company2003.
- [23] B. Sapoval, C. Hermann, Physics of semiconductors, Springer Science & Business Media2003.
- [24] E. Rosencher, B. Vinter, Optoelectronics, Cambridge University Press2002.
- [25] S.S. de la Morena, G. Recio-Sánchez, V. Torres-Costa, R. Martín-Palma, Hybrid gold/porous silicon thin films for plasmonic solar cells, Scripta Materialia, 74 (2014) 33-37.

- [26] D. Pascual Sánchez, Crystalline silicon Heterojunction solar cells, Universitat Politècnica de Catalunya, 2015.
- [27] L. Zhou, L. Xiao, H. Yang, J. Liu, X. Yu, Greatly Enhanced Photovoltaic Performance of Crystalline Silicon Solar Cells via Metal Oxide, *Nanomaterials*, 8 (2018) 505.
- [28] M. Farhat, S. Kais, F. Alharbi, Plasmonically enhanced Schottky photovoltaic devices, *Scientific reports*, 7 (2017) 14253.
- [29] D.L. Pulfrey, MIS solar cells: A review, *IEEE Transactions on Electron Devices*, 25 (1978) 1308-1317.
- [30] J. Shewchun, D. Burk, M.B. Spitzer, MIS and SIS solar cells, *IEEE Transactions on Electron Devices*, 27 (1980) 705-716.
- [31] B. Sharma, Metal-semiconductor Schottky barrier junctions and their applications, Springer Science & Business Media 2013.
- [32] X. Wang, K.Q. Peng, X.J. Pan, X. Chen, Y. Yang, L. Li, X.M. Meng, W.J. Zhang, S.T. Lee, High-Performance Silicon Nanowire Array Photoelectrochemical Solar Cells through Surface Passivation and Modification, *Angewandte Chemie International Edition*, 50 (2011) 9861-9865.
- [33] E. Garnett, P. Yang, Light trapping in silicon nanowire solar cells, *Nano letters*, 10 (2010) 1082-1087.
- [34] K.Q. Peng, S.T. Lee, Silicon nanowires for photovoltaic solar energy conversion, *Advanced Materials*, 23 (2011) 198-215.
- [35] K.E. Jasim, Quantum dots solar cells, *Solar Cells-New Approaches and Reviews*, (2015).
- [36] J.H. Kim, D.H. Shin, H.S. Lee, C.W. Jang, J.M. Kim, S.W. Seo, S. Kim, S.-H. Choi, Enhancement of efficiency in graphene/porous silicon solar cells by co-doping graphene with gold nanoparticles and bis (trifluoromethanesulfonyl)-amide, *Journal of Materials Chemistry C*, 5 (2017) 9005-9011.
- [37] R. Dewan, V. Jovanov, S. Hamraz, D. Knipp, Analyzing periodic and random textured silicon thin film solar cells by Rigorous Coupled Wave Analysis, *Scientific reports*, 4 (2014) 6029.
- [38] B.W. Schneider, N.N. Lal, S. Baker-Finch, T.P. White, Pyramidal surface textures for light trapping and antireflection in perovskite-on-silicon tandem solar cells, *Optics express*, 22 (2014) A1422-A1430.
- [39] A. Kamble, K. Mokurala, A. Gupta, S. Mallick, P. Bhargava, Synthesis of Cu<sub>2</sub>NiSnS<sub>4</sub> nanoparticles by hot injection method for photovoltaic applications, *Materials Letters*, 137 (2014) 440-443.
- [40] E. Xifré Pérez, Design, fabrication and characterization of porous silicon multilayer optical devices, Universitat Rovira i Virgili, 2007.
- [41] G. Korotcenkov, Porous silicon: from formation to application: formation and properties, Volume One, CRC Press 2016.
- [42] R. Martín-Palma, J. Pérez-Rigueiro, R. Guerrero-Lemus, J. Moreno, J. Martínez-Duart, Ageing of aluminum electrical contacts to porous silicon, *Journal of applied physics*, 85 (1999) 583-586.
- [43] E. Petrova, K. Bogoslovskaya, L. Balagurov, G. Kochoradze, Room temperature oxidation of porous silicon in air, *Materials Science and Engineering: B*, 69 (2000) 152-156.
- [44] V. Petrova-Koch, T. Muschik, A. Kux, B. Meyer, F. Koch, V. Lehmann, Rapid-thermal-oxidized porous Si- The superior photoluminescent Si, *Applied physics letters*, 61 (1992) 943-945.
- [45] R.C. Anderson, R.S. Muller, C.W. Tobias, Chemical surface modification of porous silicon, *Journal of the Electrochemical Society*, 140 (1993) 1393.
- [46] J.M. Lauerhaas, M.J. Sailor, The effects of halogen exposure on the photoluminescence of porous silicon, *MRS Online Proceedings Library Archive*, 298 (1993).
- [47] D. Andsager, J. Hilliard, M.H. Nayfeh, Behavior of porous silicon emission spectra during quenching by immersion in metal ion solutions, *Applied physics letters*, 64 (1994) 1141-1143.
- [48] P. Steiner, F. Kozlowski, M. Wielunski, W. Lang, Enhanced blue-light emission from an indium-treated porous silicon device, *Japanese journal of applied physics*, 33 (1994) 6075.
- [49] J. Kanungo, S. Maji, A.K. Mandal, S. Sen, E. Bontempi, A. Balamurugan, A. Tyagi, K. Uvdal, S. Sinha, H. Saha, Surface treatment of nanoporous silicon with noble metal ions and characterizations, *Applied surface science*, 256 (2010) 4231-4240.

- [50] K.L. Kelly, E. Coronado, L.L. Zhao, G.C. Schatz, *The optical properties of metal nanoparticles: the influence of size, shape, and dielectric environment*, ACS Publications, 2003.
- [51] J. Conde, G. Doria, P. Baptista, *Noble metal nanoparticles applications in cancer*, *Journal of drug delivery*, 2012 (2012).
- [52] H. Malekzad, P.S. Zangabad, H. Mirshekari, M. Karimi, M.R. Hamblin, *Noble metal nanoparticles in biosensors: recent studies and applications*, *Nanotechnology reviews*, 6 (2017) 301-329.
- [53] R. Mishra, K. Rajanna, *Metal-oxide thin film with Pt, Au and Ag nano-particles for gas sensing applications*, *Sensors and Materials*, 17 (2005) 433-440.
- [54] R. Ramadan, M. Manso-Silvan, R.J. Martın-Palma, *Hybrid porous silicon/silver nanostructures for the development of enhanced photovoltaic devices*, *Journal of Materials Science*, 55 (2020) 5458-5470.
- [55] X.-F. Zhang, Z.-G. Liu, W. Shen, S. Gurunathan, *Silver nanoparticles: synthesis, characterization, properties, applications, and therapeutic approaches*, *International journal of molecular sciences*, 17 (2016) 1534.
- [56] L.B. Anigol, J.S. Charantimath, P.M. Gurubasavaraj, *Effect of concentration and ph on the size of silver nanoparticles synthesized by green chemistry*, *Org. Med. Chem. Int. J.*, 3 (2017) 1-5.
- [57] R.J.M. Palma, A. Lakhtakia, *Nanotechnology: A Crash Course*, SPIE, 2010.
- [58] F. Agullo-Rueda, R. Martın-Palma, J. Martınez-Duart, *NANOTECHNOLOGY FOR MICROELECTRONICS AND OPTOELECTRONICS*, Elsevier Academic Press, 2017.
- [59] G. Suriati, M. Mariatti, A. Azizan, *Synthesis of silver nanoparticles by chemical reduction method: Effect of reducing agent and surfactant concentration*, *International journal of automotive and mechanical engineering*, 10 (2014) 1920.
- [60] T. Torimoto, K.-i. Okazaki, T. Kiyama, K. Hirahara, N. Tanaka, S. Kuwabata, *Sputter deposition onto ionic liquids: Simple and clean synthesis of highly dispersed ultrafine metal nanoparticles*, *Applied physics letters*, 89 (2006) 243117.
- [61] S. Perera, R. Mariano, K. Vu, N. Nour, O. Seitz, Y. Chabal, K. Balkus, *Hydrothermal synthesis of graphene-TiO<sub>2</sub> nanotube composites with enhanced photocatalytic activity*. *ACS Catal* 2: 949–956, 2012.
- [62] H. Park, S. Chang, J. Jean, J.J. Cheng, P.T. Araujo, M. Wang, M.G. Bawendi, M.S. Dresselhaus, V. Bulovic, J. Kong, *Graphene cathode-based ZnO nanowire hybrid solar cells*, *Nano letters*, 13 (2013) 233-239.
- [63] W. Lu, C.M. Lieber, *Nanoelectronics from the bottom up*, *Nanoscience And Technology: A Collection of Reviews from Nature Journals*, (2010) 137-146.
- [64] C. Han, Z. Chen, N. Zhang, J.C. Colmenares, Y.J. Xu, *Hierarchically CdS decorated 1D ZnO nanorods-2D graphene hybrids: low temperature synthesis and enhanced photocatalytic performance*, *Advanced Functional Materials*, 25 (2015) 221-229.
- [65] Y. Li, H. Wang, L. Xie, Y. Liang, G. Hong, H. Dai, *MoS<sub>2</sub> nanoparticles grown on graphene: an advanced catalyst for the hydrogen evolution reaction*, *Journal of the American Chemical Society*, 133 (2011) 7296-7299.
- [66] W. Tian, D. Liu, F. Cao, L. Li, *Hybrid nanostructures for photodetectors*, *Advanced Optical Materials*, 5 (2017) 1600468.

## 1.5. Abbreviations in the general introduction

NanoPS	Nanostructured porous Silicon
AgNPs	Silver nanoparticles
MIS	metal-insulator-semiconductor
PEDOT:PSS	poly(3,4- ethylenedioxythiophene) polystyrene sulfonate
NPs	Nanoparticles
AC	Alternating current
DC	Direct current
PV	photovoltaic
$E_g$	Energy gap
$\alpha$	absorption coefficient
K	wavevector
MS	metal-semiconductor
HF	hydrofluoric
J	current density
SPR	surface plasmon resonance
0D	zero-dimensional
1D	one-dimensional
2D	two-dimensional
3D	three-dimensional

## **Chapter 2:**

### **Effect of electrolyte pH value and current density on the electrodeposition of silver nanoparticles into porous silicon.**

R. Ramadan, R. J. Martín-Palma, *journal of nanophotonics*, 14(4), (2020), 040501

---

# Effect of electrolyte pH value and current density on the electrodeposition of silver nanoparticles into porous silicon

Rehab Ramadan<sup>a,b,\*</sup> and Raúl J. Martín-Palma<sup>a,c</sup>

<sup>a</sup>Universidad Autónoma de Madrid, Departamento de Física Aplicada, Madrid, Spain

<sup>b</sup>Minia University, Department of Physics, Faculty of Science, Minia, Egypt

<sup>c</sup>Instituto de Ciencia de Materiales Nicolás Cabrera, Madrid, Spain

**Abstract.** Nanostructured porous silicon (PS) can be used as a template for the growth of noble metal nanoparticles for the subsequent development of metal/semiconductor hybrid structures with application in several fields. The current work reports on the electrodeposition of silver nanoparticles (AgNPs) into columnar PS layers. In particular, the size, morphology, and surface density of the AgNPs grown into PS were studied as a function of the electrolyte pH value and the infiltration current density. Furthermore, the optical properties of the hybrid PS + AgNPs structures were analyzed. The experimental results show a remarkable reduction in the size of AgNPs and increased growth rate upon reducing the acidity of the electrolyte and upon increasing the current density. In addition, a remarkable reduction of the average reflectance is observed under specific fabrication conditions. In particular, as the pH values of the electrolyte increase, the optical reflectance decreases. This relation is attributed to the reduction in the AgNPs size. On the other hand, increasing the infiltration current density increases the average reflectance due to increasing surface density of the AgNPs. These results demonstrate that the size and shape of AgNPs can be controlled by adjusting the applied infiltration current density and the pH value of the electrolyte depending on the intended application. © 2020 Society of Photo-Optical Instrumentation Engineers (SPIE) [DOI: [10.1117/1.JNP.14.040501](https://doi.org/10.1117/1.JNP.14.040501)]

**Keywords:** porous silicon; silver nanoparticles; electrolyte pH value; infiltration current density; optical properties.

Paper 20085L received Jun. 24, 2020; accepted for publication Oct. 20, 2020; published online Nov. 3, 2020.

## 1 Introduction

The unique physical and chemical properties of noble metals allow them to be exploited in a wide variety of applications in such diverse fields as biomedicine, energy harvesting, and gas sensing.<sup>1-4</sup> In the case of low-dimension materials, these properties greatly depend on the surface-to-volume ratio.<sup>5</sup> Since nanoparticles (NPs) possess a large surface to volume ratio, their electrical, optical, and magnetic properties remarkably depart from their bulk properties.<sup>6-8</sup> Accordingly, the size and shape of NPs need to be precisely controlled for the target application. But other features such as their size distribution, state of aggregation, and arrangement over a surface need also to be accurately controlled. In this regard, numerous physical and chemical methods have been developed to synthesize noble metal NPs with controlled properties.<sup>9,10</sup> Electrochemical infiltration is one of the most effective techniques used to control the characteristic features of the synthesized material. Some of the key fabrication parameters include time of infiltration, electrolyte pH value, infiltration current density, and processing temperature.<sup>11-14</sup>

NPs can be deposited on a variety of materials, flat or rough, such as glass, ceramic, silicon wafers, aluminum foil, copper sheet, and plastic.<sup>15</sup> In particular, porous silicon (PS) has been extensively used for the infiltration of several NPs, including silver, gold, copper, dielectric

\*Address all correspondence to Rehab Ramadan, [rehab.ramadan@uam.es](mailto:rehab.ramadan@uam.es)

materials, and liquid crystals.<sup>16–20</sup> The optical, electrical, and thermal properties of PS can be rather easily adjusted by changing its porosity and pore shape.<sup>21,22</sup> For this reason, PS has been demonstrated as a versatile material with applications in fields ranging from optoelectronics to biomedicine.

In this study, a combination of electrochemical etching of Si and electrodeposition of silver nanoparticles (AgNPs) for the development of hybrid structures PS + AgNPs is presented. In particular, AgNPs with different sizes and shapes were infiltrated into PS layers using different electrolyte pH values and infiltration current densities. Furthermore, the effect of the fabrication parameters on the optical properties of the PS layers and the hybrid PS + AgNPs structures was studied. Accordingly, this work will serve to establish a relationship between the size and morphology of the AgNPs and the optical properties of the hybrid PS + AgNPs structures.

## 2 Experimental

### 2.1 Fabrication of Porous Silicon Layers

PS layers were electrochemically etched from heavily boron-doped (p-type) crystalline silicon wafers, with orientation  $\langle 100 \rangle$  and resistivity 0.01 to 0.02  $\Omega \cdot \text{cm}$ . Typically, a silicon chip with an area of  $1.5 \times 1.5 \text{ cm}^2$  was mounted in a sample holder with a circular area of about  $1.23 \text{ cm}^2$ , exposed to the etching solution. The etching solution consists of a 1:2 HF (48%)/ethanol (99%) mixture. Before the etching process, the substrate was cleaned by immersion in ethanol to remove any contaminations. The applied current density was fixed at 80 mA/cm<sup>2</sup> and the anodization time was 11 s, leading to columnar nanostructured PS layers. After the fabrication process, each sample was rinsed in ethanol and dried with a mild stream of dry nitrogen. The fabrication process of the experimental setup was schematically described in a previous work.<sup>23</sup>

### 2.2 Infiltration of AgNPs into PS

AgNPs were infiltrated into the nanostructured columnar PS layers by the electrochemical deposition method. The AgNPs were cathodically electrodeposited using a Bio-Logic SP-150 potentiostat. The aqueous solution was composed of 0.1 mM silver nitrate (the salt), 0.25 mM sodium citrate (the stabilizer), 0.01 M to 0.02 M nitric acid (control the electrolyte acidity), and 1000 ml distilled water (the solvent). The current work is devoted to study the effect of the electrolyte pH value and infiltration current density on the morphology, size, and density on the infiltrated AgNPs. For that, three different target pH values of the electrolyte were selected as (1.7, 2.0, and 3.0). The pH values were controlled by adjusting nitric acid concentration. Regarding the electrodeposition parameters, the infiltration current density ( $J$ ) was varied between 10 nA/cm<sup>2</sup> and 1  $\mu\text{A}/\text{cm}^2$ . Meanwhile, the infiltration time was fixed constant at 12 min.

### 2.3 Morphological Characterization

Cross-sectional and top-view images of the samples were acquired using a Philips XL 30S-FEG field emission scanning electron microscope (FESEM) operated at 10 kV. An energy dispersive spectroscopy (EDS) x-ray analyzer (Inca X-sight 7558, Oxford Instruments, London, UK) coupled to the microscope was used to determine the elemental compositions of the hybrid PS + AgNPs structure. The structure and sizes of the pores of PS and the AgNPs were determined from these FESEM images using the ImageJ software.

### 2.4 Optical Reflectance Measurement

The overall reflectance spectra in the wavelength range (250 to 900 nm) were acquired using a double-beam spectrophotometer (V-560, JASCO International, Tokyo, Japan) equipped with an integrating sphere in order to collect both diffuse and specular reflections, with unpolarized light being 10 deg (i.e., almost normal incidence) on the sample.

### 3 Experimental Results

#### 3.1 Morphology

##### 3.1.1 Effect of the electrolyte pH value

The morphology, size, distribution, and growth rate of metal NPs grown by electrochemical deposition methods generally depend on several factors. These include the specific fabrication parameters, electrolyte pH value, and the surface of growth. The current work is devoted to studying the effect of pH values and infiltration current density on the characteristic features of AgNPs, grown into columnar PS layers. Figure 1 shows typical cross-sectional FESEM images of hybrid PS + AgNPs structures for various electrolyte pH values (1.7, 2.0, and 3.0). Since alkaline media are well-known to degrade PS, acidic electrolytes controlled by nitric acid solvent were used for the infiltration of the AgNPs into the PS layers. Figure 1(a) shows that for pH = 1.7, relatively large agglomerates of AgNPs grow on the surface of the PS layers. Additionally, the size of the infiltrated AgNPs has been observed to decrease upon the reduction in the electrolyte acidity (pH values increasing from 2.0 to 3.0), as shown in Figs. 1(b) and 1(c). This behavior is attributed to increased reaction rate upon increasing the pH values and a subsequent increase in the nucleation rate.<sup>6</sup> In other words, the increase in the reaction rate leads to increased dissolution rate by reducing the chelating agent concentration (nitric acid).<sup>24</sup> In the aqueous electrolyte, chelating agents have a ring-like center to form at least two bonds with the metal ions. Therefore, increasing the electrolyte acidity hinders the release of small particles, given a reduction in the nucleation rate and growth of large NPs [Fig. 1(a)]. The same behavior was previously observed for AgNPs synthesized by green chemistry methods for a wide range of pH values (3, 5, 7, 9, and 11).<sup>6</sup> The EDS analysis shown in Fig. 1(d) confirms the infiltration of the large AgNPs into the PS layer.

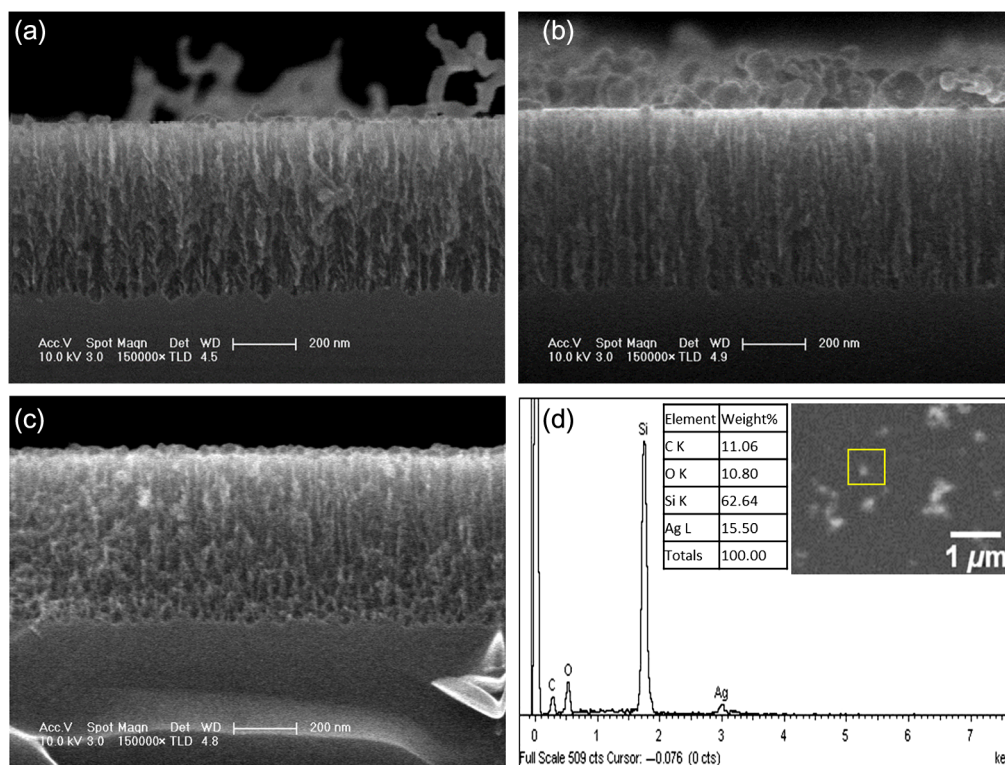


**Fig. 1** Cross sectional FESEM images of hybrid PS + AgNPs structures. The aqueous solutions were prepared at different pH values: (a) pH = 1.7, (b) pH = 2.0, and (c) pH = 3.0. (d) Typical EDS spectrum of a PS layer conjugated with AgNPs.



### 3.1.2 Effect of the infiltration current density

In electrodeposition processes, the infiltration current density ( $J$ ) is one of the key parameters and has a direct effect on the size and morphology of the deposited nanostructures. Figure 2 shows the effect of  $J$  on the size and distribution of the electrodeposited AgNPs. When the lowest deposition current density ( $10 \text{ nA/cm}^2$ ) is used, the AgNPs tend to aggregate, as observed in Fig. 2(a). However, under a higher current density ( $30 \text{ nA/cm}^2$ ), the dissolution rate increases and NPs with sizes in the 20- to 55-nm diameter range start to cover the PS surface more homogeneously, as shown in Fig. 2(b). Furthermore, at  $1 \mu\text{A/cm}^2$ , the infiltrated AgNPs have spherical shapes with typical diameters between 6 and 30 nm. In summary, the size and distribution of the AgNPs remarkably changes with increasing current density.

This behavior might be attributed to three main mechanisms.<sup>25</sup> (1) The nucleation rate increases with increasing current density. (2) Generation of a nonuniform electric field due to the unequal conductivity of PS given by its typical random distribution of nanopores. Upon increasing the applied current density, the generated electric field increases. This leads to an increased growth rate of smaller NPs on the PS surface. (3) Shift in reaction control from kinetic control (charge transfer control) to mass transfer control (diffusion control). Charge transfer control is defined by activation control because at specific applied current densities, ions tend to move fast toward the cathode surface. As a result, the growth rate becomes higher than the nucleation rate so that agglomeration of NPs takes place. However, mass transfer control results in the formation of diffusion-limited aggregates or dendrites so that small AgNPs grow.<sup>26</sup> In addition, the interaction between the infiltrated NPs with the surface of PS is very low at low infiltration current densities, which is attributed to the low electrical conductivity of PS. As a result, the infiltrated NPs tend to agglomerate. Increasing the electrical current density helps the NPs to localize into the surface of PS and increases the growth rate. These observations agree with previous results on electrodeposited maghemite ( $\gamma\text{-Fe}_2\text{O}_3$ ) NPs. In this case, the sizes of the NPs decreased from  $\sim 23$  to 7 nm after increasing the current density from 150 to 2000  $\text{mA/cm}^2$ ,

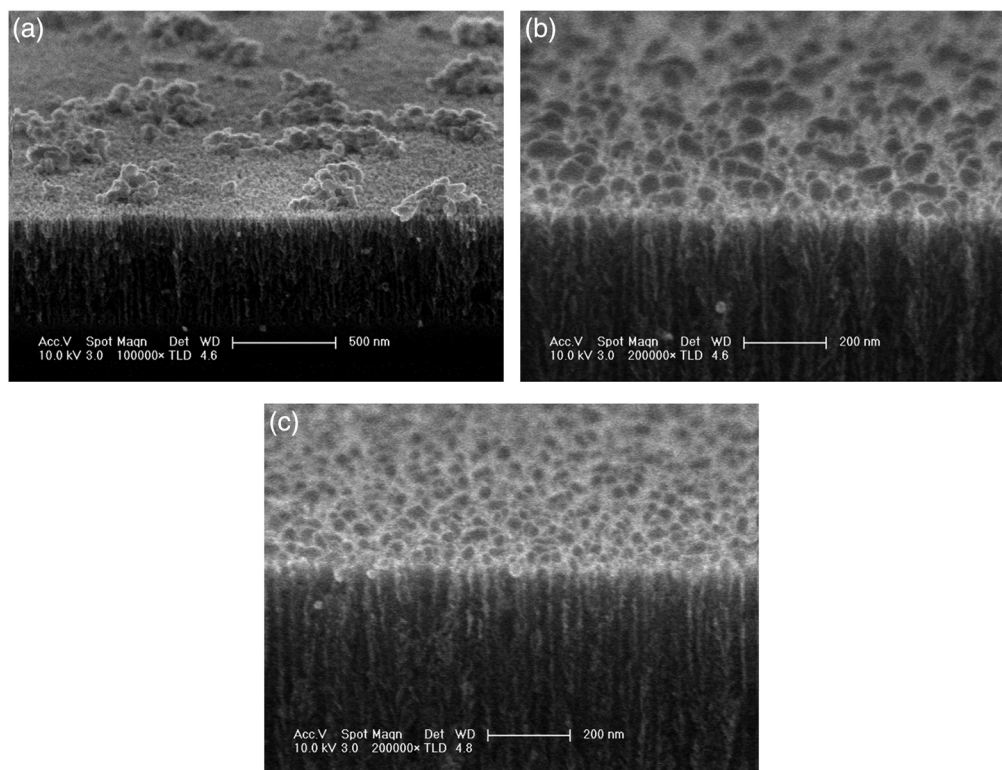


**Fig. 2** Tilted cross-sectional FESEM images of hybrid PS+AgNPs structures. The AgNPs were synthesized at different infiltration current densities ( $J$ ) for 12 min, with constant electrolyte pH value ( $\text{pH} = 3.0$ ). (a)  $J = 10 \text{ nA/cm}^2$ , (b)  $J = 30 \text{ nA/cm}^2$ , and (c)  $J = 1 \mu\text{A/cm}^2$

and the production rate increased from 0.1 to 2.5 g h<sup>-1</sup> cm<sup>-2</sup>.<sup>25</sup> These results demonstrate that the size and shape of AgNPs can be controlled by adjusting the applied infiltration current density and the pH value of the electrolyte depending on the intended application.

### 3.2 Optical Behavior

Figure 3 shows the reflectance spectra of PS layers grown onto silicon substrates, as well as different hybrid PS + AgNPs structures. As previously discussed, changing the pH value of the silver nitrate electrolyte (2.0 or 3.0) results in AgNPs with different sizes and distributions, as shown in Fig. 1.

PS is described as a mixture of silicon nanocrystallites, air (the nanopores), and amorphous silicon.<sup>27,28</sup> Therefore, PS can be used to fabricate antireflective coatings since its effective refractive index can be controlled by adjusting its constituents.<sup>29</sup> As such, a remarkable reduction of the average reflectance can be obtained using the appropriate fabrication conditions. Furthermore, an additional reflection reduction in specific wavelength ranges can be obtained taking advantage of plasmonic effects produced by metallic NPs, such as Au or Ag.<sup>17,23</sup> However, the specific optical behavior depends on the density and morphology of the infiltrated NPs.<sup>30</sup> Nevertheless, in some cases, the presence of metal NPs leads to increased reflectance, as is the case of hybrid PS + AgNPs structures fabricated using solutions with pH = 2.0. This increase in reflectance is attributed to a large surface density of the AgNPs as portrayed in Fig. 1(b). A large increase in the surface density of the AgNPs leads to reaching the percolation threshold or even to form a quasicontinuous film,<sup>31</sup> thus preventing the manifestation of plasmonic effects and effectively increasing reflectance.

Figure 4 shows the effect of the infiltration current density on the average reflectance in the 250- to 900-nm wavelength range for samples fabricated using electrolytes with pH values of 2.0 and 3.0. The experimental results show that increasing the infiltration current density for a constant deposition time (12 min) leads to increased average reflectance for the two pH values. The reason behind this effect is that under the appropriate infiltration current density, the deposited AgNPs interact with the PS surface and the dissolution rate increases. As a result, the growth rate on the PS surface increases and the AgNPs are more regularly distributed, which might lead to reaching the percolation threshold. On the other hand, at low values of deposition current density, the NPs tend to agglomerate and clusters of AgNPs appear in defined areas over the PS surface. As a result, the average reflectance decreases according to the distribution and surface density of AgNPs on the PS surface. In addition, the average reflectance decreased with increasing pH values of the electrolytes used for NP infiltration. This behavior is attributed to a reduction of the size of the infiltrated NPs for higher pH values due to increased dissolution rate.

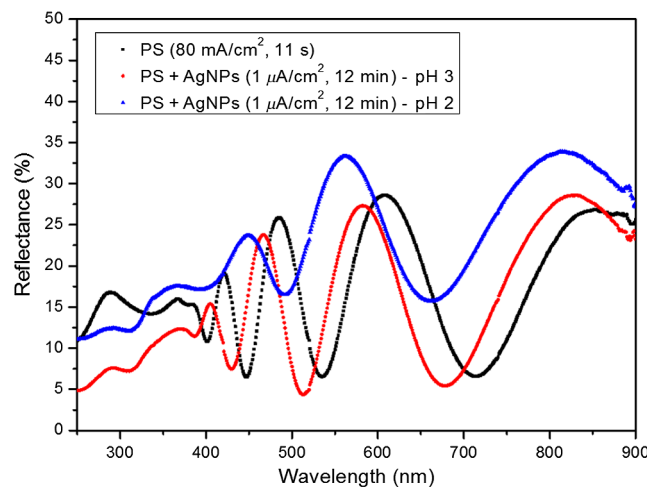


**Fig. 3** Overall reflectance of PS and hybrid PS + AgNPs structures using electrolytes with pH values of 2 and 3. Both the infiltration current densities of the AgNPs and the electrodeposition times were the same, i.e., 1  $\mu\text{A}/\text{cm}^2$  and 12 min.

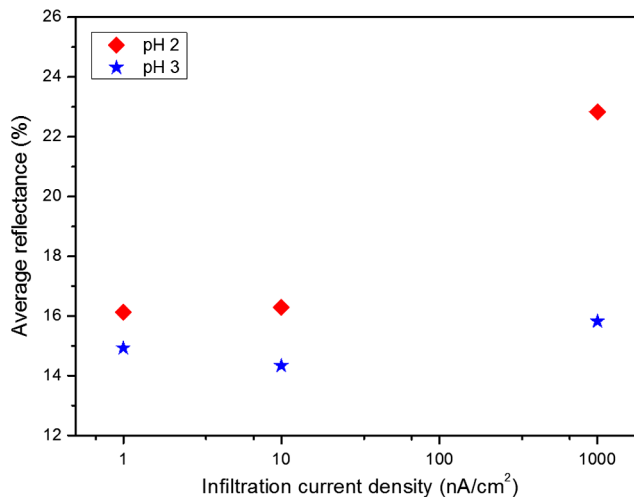


**Fig. 4** Average reflectance in the 250 to 900 nm wavelength range as a function of the infiltration current density for hybrid PS + AgNPs structures. The AgNPs were infiltrated using electrolytes with pH values of 2 and 3. The deposition time remained constant (12 min).

## 4 Conclusions

Nanostructured columnar PS layers were used as templates for the subsequent electrodeposition of AgNPs. It was found that changing the electrodeposition parameters led to the growth of AgNPs with different characteristics. The effect of the electrolyte pH values and infiltration current densities were analyzed by FESEM and UV–visible spectrometry. The experimental results show that the size of the infiltrated AgNPs decreases upon the reduction in the electrolyte acidity as well as upon increasing the infiltration current density. This behavior is a result of the increase in the reaction rate by reducing the electrolyte acidity and the increase in the dissolution rate upon increasing the infiltration current density. By increasing the nucleation rate, the AgNPs start to distribute more homogeneously on the PS surface.

Additionally, the overall optical reflectance of the hybrid PS + AgNPs structures was studied as a function of the AgNPs fabrication parameters (electrolyte pH values and infiltration current densities). PS layers effectively reduce the overall reflectance of bulk silicon, due to a reduction of the effective refractive index as a consequence of combining silicon with air. The reflectance of the hybrid PS + AgNPs structures can be lower than that of PS due to plasmonic effects or higher if a continuous Ag layer is formed. This will depend on the size, shape, and density of the infiltrated AgNPs. Increasing the acidity of the electrolyte or the infiltration current density leads to higher overall reflectance of the hybrid nanostructures. This behavior is attributed to the increase in the size of the deposited AgNPs upon increasing the electrolyte acidity. In addition, increasing the infiltration current density leads to higher dissolution rate which in turn results in larger density of AgNPs.

In all, the hybrid PS + AgNPs structures might be of interest for use in different fields, such as solar energy harvesting or biomedicine. Depending on the intended application, the characteristic features of the deposited AgNPs can be easily optimized by setting the appropriate electrolyte pH value and infiltration current density.

## Acknowledgments

The authors are thankful to Mr. Luis García Pelayo and Dr. Valentin Constantin Nistor for technical support. This research was partially funded by the Universidad Autónoma de Madrid and the Cultural Affairs and Missions Sector, Ministry of Higher Education. This work was part of ATTRACT that has received funding from the European Union's Horizon 2020 Research and Innovation Program. The authors declare no conflicts of interest.

## References

1. J. Conde, G. Doria, and P. Baptista, "Noble metal nanoparticles applications in cancer," *J. Drug Delivery* **2012**, 1–12 (2012).
2. H. Malekzad et al., "Noble metal nanoparticles in biosensors: recent studies and applications," *Nanotechnol. Rev.* **6**, 301–329 (2017).
3. M. A. Carpenter, S. Mathur, and A. Kolmakov, "Metal oxide nanomaterials for chemical sensors," Springer Science & Business Media, New York (2005).
4. R. Ramadan, M. Manso-Silván, and R. J. Martín-Palma, "Hybrid porous silicon/silver nanostructures for the development of enhanced photovoltaic devices," *J. Mater. Sci.* **55**, 5458–5470 (2020).
5. X.-F. Zhang et al., "Silver nanoparticles: synthesis, characterization, properties, applications, and therapeutic approaches," *Int. J. Mol. Sci.* **17**, 1534 (2016).
6. L. B. Anigol, J. S. Charantimath, and P. M. Gurubasavaraj, "Effect of concentration and pH on the size of silver nanoparticles synthesized by green chemistry," *Org. Med. Chem. Int. J.* **3**, 1–5 (2017).
7. R. J. M. Palma and A. Lakhtakia, *Nanotechnology: A Crash Course*, SPIE Press, Bellingham, Washington, DC (2010).
8. F. Agulló-Rueda, R. Martín-Palma, and J. Martínez-Duart, *Nanotechnology for Microelectronics and Optoelectronics*, Elsevier, Academic Press (2017).
9. G. Suriati, M. Mariatti, and A. Azizan, "Synthesis of silver nanoparticles by chemical reduction method: effect of reducing agent and surfactant concentration," *Int. J. Automot. Mech. Eng.* **10**, 1920 (2014).
10. T. Torimoto et al., "Sputter deposition onto ionic liquids: simple and clean synthesis of highly dispersed ultrafine metal nanoparticles," *Appl. Phys. Lett.* **89**, 243117 (2006).
11. A. Suresh et al., "Effect of pH on structural and electrical properties of electrodeposited Bi<sub>2</sub>Te<sub>3</sub> thin films," *J. Electron. Mater.* **38**, 449–452 (2009).
12. T. M. Day, P. R. Unwin, and J. V. Macpherson, "Factors controlling the electrodeposition of metal nanoparticles on pristine single walled carbon nanotubes," *Nano Lett.* **7**, 51–57 (2007).
13. K. Lepkova, J. Clohessy, and V. Cunnane, "The pH-controlled synthesis of a gold nanoparticle/polymer matrix via electrodeposition at a liquid–liquid interface," *J. Phys. Condens. Mater* **19**, 375106 (2007).
14. M. Alqadi et al., "pH effect on the aggregation of silver nanoparticles synthesized by chemical reduction," *Mater. Sci.-Pol.* **32**, 107–111 (2014).
15. A. R. Markelonis et al., "Nanoparticle film deposition using a simple and fast centrifuge sedimentation method," *Appl. Nanosci.* **5**, 457–468 (2015).
16. G. Recio-Sánchez et al., "Nanostructured copper/porous silicon hybrid systems as efficient sound-emitting devices," *Nanoscale Res. Lett.* **9**, 487 (2014).
17. S. S. de la Morena et al., "Hybrid gold/porous silicon thin films for plasmonic solar cells," *Scr. Mater.* **74**, 33–37 (2014).
18. L.-C. Chen and C.-Y. Weng, "Optoelectronic properties of MAPbI<sub>3</sub> perovskite/titanium dioxide heterostructures on porous silicon substrates for cyan sensor applications," *Nanoscale Res. Lett.* **10**, 404 (2015).
19. L. M. Pappu et al., "Voltage controlled scattering from porous silicon Mie-particles in liquid crystals," *J. Mol. Liq.* **281**, 108–116 (2019).
20. M. Hernandez et al., "Surface enhanced fluorescence of anti-tumoral drug emodin adsorbed on silver nanoparticles and loaded on porous silicon," *Nanoscale Res. Lett.* **7**, 364 (2012).
21. G. Vincent, "Optical properties of porous silicon superlattices," *Appl. Phys. Lett.* **64**, 2367–2369 (1994).
22. R. Ramadan and R. J. Martín-Palma, "Electrical characterization of MIS Schottky barrier diodes based on nanostructured porous silicon and silver nanoparticles with applications in solar cells," *Energies* **13**, 2165 (2020).
23. R. J. Martín-Palma et al., "Hybrid nanostructured porous silicon-silver layers for wideband optical absorption," *Sci. Rep.* **9**, 7291 (2019).

24. M. Ahmad and M. Rusop, "Influence of glacial acetic acid and nitric acid as a chelating agent in Sol-gel process to the nanostructured titanium dioxide thin films," in *AIP Conf. Proc.*, American Institute of Physics, pp. 339–344 (2009).
25. H. Park et al., "Electrodeposition of maghemite ( $\gamma$ -Fe<sub>2</sub>O<sub>3</sub>) nanoparticles," *Chem. Eng. J.* **139**, 208–212 (2008).
26. F. Nasirpour, *Electrodeposition of Nanostructured Materials*, Springer, Switzerland (2017).
27. R. Martín-Palma et al., "Direct determination of grain sizes, lattice parameters, and mismatch of porous silicon," *Appl. Phys. Lett.* **81**, 25–27 (2002).
28. R. Martín-Palma et al., "Monte Carlo determination of crystallite size of porous silicon from x-ray line broadening," *Appl. Phys. Lett.* **87**, 211906 (2005).
29. V. Torres-Costa, R. Martín-Palma, and J. Martínez-Duart, "Optical constants of porous silicon films and multilayers determined by genetic algorithms," *J. Appl. Phys.* **96**, 4197–4203 (2004).
30. J. Mock et al., "Shape effects in plasmon resonance of individual colloidal silver nanoparticles," *J. Chem. Phys.* **116**, 6755–6759 (2002).
31. T. G. Mackay and A. Lakhtakia, "Percolation thresholds in the homogenization of spheroidal particles oriented in two directions," *Opt. Commun.* **259**, 727–737 (2006).

## Abbreviations in chapter 2

PS	porous Silicon
AgNPs	Silver nanoparticles
NPs	Nanoparticles
FESEM	Field emission scanning electron microscope
EDX	Energy dispersive spectroscopy X-ray
J	current density
$\gamma$ -Fe <sub>2</sub> O <sub>3</sub>	Maghemite


## **Chapter 3:**

### **Hybrid Nanostructured Porous Silicon-Silver Layers for Wideband Optical Absorption**

R. J. Martín-Palma, P. D. McAtee, R. Ramadan, A. Lakhtakia, *Scientific reports*, 9(1), (2019), 1-8.

---

# SCIENTIFIC REPORTS



OPEN

## Hybrid Nanostructured Porous Silicon-Silver Layers for Wideband Optical Absorption

Raúl J. Martín-Palma<sup>1,2</sup>, Patrick D. McAtee<sup>3</sup>, Rehab Ramadan<sup>2,4</sup> & Akhlesh Lakhtakia<sup>3</sup>

As subwavelength nanostructures are receiving increasing attention for photonic and plasmonic applications, we grew nanostructured porous silicon (n-PS) and hybrid n-PS/Ag layers onto silicon substrates and measured their reflection and absorption characteristics as functions of the wavelength, angle of incidence, and polarization state of incident light. The experimental results show that the absorption characteristics of the hybrid n-PS/Ag layer can be controlled by selecting the appropriate combination of its thickness and porosity, together with the density of infiltrant silver nanoparticles. The observed wideband optical absorption characteristics of the hybrid n-PS/Ag layers might be useful in light-harvesting devices and photodetectors, since the overall efficiency will be increased as a result of increased field-of-view for both *s*- and *p*-polarization states of incident light.

Although nanostructured porous silicon (n-PS) was discovered by Uhlir in 1956 while studying electropolishing of silicon and germanium in HF-based solutions<sup>1</sup>, it was not until the observation visible photoluminescence from room-temperature n-PS by Canham in 1990<sup>2</sup> that this material was envisaged as a good candidate for applications in the field of photonics. Since then, its many additional properties beyond photo- and electro-luminescence have resulted in several successful applications in different fields ranging from microelectronics to biomedicine<sup>3</sup>.

Nanostructured porous silicon can be described quite simply as an amorphous matrix in which silicon nanocrystals are embedded<sup>4–7</sup>. The morphology of a n-PS sample depends on strongly on the specific fabrication parameters, including electrolyte composition and fabrication current density<sup>8</sup>. The complex-valued effective refractive index of n-PS is therefore dependent on the electrochemical fabrication parameters<sup>9</sup>. Control over the refractive index allows the use of n-PS for tunable photonic structures made entirely of silicon<sup>10</sup>. It is worth pointing out that the electrochemical technique used for the fabrication of n-PS is compatible with current CMOS fabrication processes, thus enabling the potential integration of n-PS into circuits using microelectronics-compatible procedures.

Within this context and given the increasing attention being received by subwavelength nanostructures for photonic and plasmonic applications<sup>11,12</sup>, we decided to explore the use of n-PS and hybrid n-PS/Ag layers grown onto silicon as wideband optical absorbers. Therefore, we experimentally investigated the dependence of optical absorption characteristics of n-PS and hybrid n-PS/Ag layers on the thickness and porosity of n-PS layers and the amount of silver infiltrating the pores of n-PS. More specifically, we measured the reflection and absorption characteristics of the n-PS and hybrid n-PS/Ag layers as functions of the wavelength, angle of incidence, and polarization state of incident light.

### Experimental

**Fabrication of n-PS and hybrid n-PS/Ag layers.** Nanostructured porous silicon layers were formed by the electrochemical etching of boron-doped (*p*-type) silicon wafers of <100> orientation, resistivity in the 0.01–0.02 Ω-cm range, and surface roughness on the order of 0.1 nm. The wafers were cut into 1.5 × 1.5 cm<sup>2</sup> pieces. Each piece was mounted in a sample holder with about 1.23 cm<sup>2</sup> area exposed to the etching solution, which was formulated as a 1:2 HF (48 wt %):ethanol (98 wt %) mixture. The anodization times, ranging from 18–46 s, were adjusted to obtain layers of three different thickness. Two different current densities — namely, 20 and 60 mA/cm<sup>2</sup> — were used, leading to two different porosities arising from the creation of nanocolumnar pores

<sup>1</sup>Department of Materials Science and Engineering, The Pennsylvania State University, University Park, Pennsylvania, PA, 16802, USA. <sup>2</sup>Departamento de Física Aplicada, Universidad Autónoma de Madrid, 28049 Cantoblanco, Madrid, Spain. <sup>3</sup>Department of Engineering Science and Mechanics, The Pennsylvania State University, University Park, Pennsylvania, PA, 16802, USA. <sup>4</sup>Department of Physics, Faculty of Science, Minia University, 61519, Minia, Egypt. Correspondence and requests for materials should be addressed to R.J.M.-P. (email: [raul@psu.edu](mailto:raul@psu.edu))



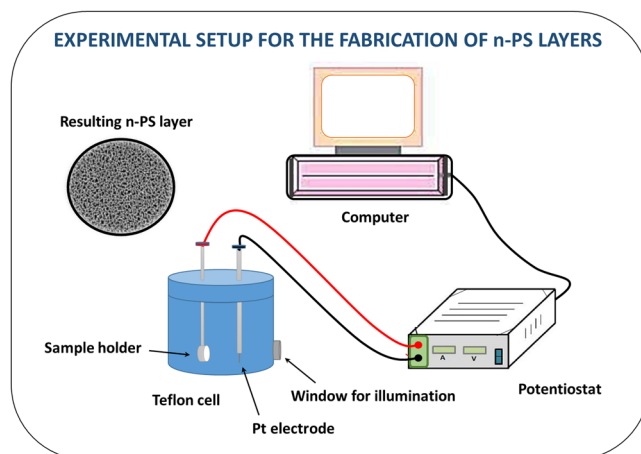


**Figure 1.** Experimental setup used for the fabrication of n-PS layers by the electrochemical etch of silicon wafers.

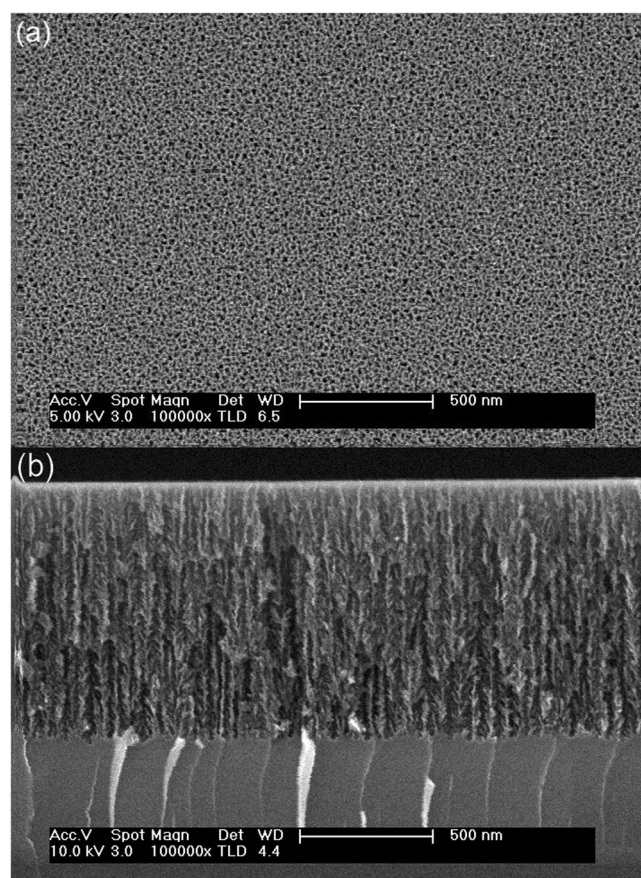


**Figure 2.** (a) Top-view and (b) cross-sectional FESEM images of a typical high-porosity n-PS layer (fabrication current density of  $60 \text{ mA/cm}^2$ ).

of two different average diameters. After fabrication, each sample was rinsed in ethanol and blown dry with a mild stream of dry nitrogen. The experimental setup used for the fabrication of n-PS layers by the electrochemical etch of silicon wafers is schematically depicted in Fig. 1.

The n-PS layer was used as a template for the subsequent growth of silver nanoparticles inside the porous structure. For this task, a modified electrochemical deposition process<sup>13</sup> was implemented. This process was carried out using a Bio-Logic SP-150 potentiostat at a fixed current density of  $1 \mu\text{A/cm}^2$  for different electrodeposition durations (2, 4, 6 or 15 min) in an aqueous solution of silver nitrate (0.1 mM), sodium citrate (0.25 mM), and nitric acid (0.01 M), with  $\text{pH} = 3$ . Afterwards, the sample was rinsed in ethanol for 5 min and subsequently

Current density (mA/cm <sup>2</sup> )	Duration of anodization (s)	Thickness (μm)	Duration of electrodeposition (min)
<b>n-PS and hybrid n-PS/Ag layers</b>			
20 (low porosity)	22	0.33	0
	33	0.60	0
	46	0.77	0
60 (high porosity)	18	0.70	0
	28	1.00	0
	40	1.40	0
60 (high porosity)	18	0.70	2, 4, 6, or 15
	28	1.00	2, 4, 6, or 15
	40	1.40	2, 4, 6, or 15

**Table 1.** Summary of the fabrication conditions of the n-PS layers and hybrid n-PS/Ag layers.

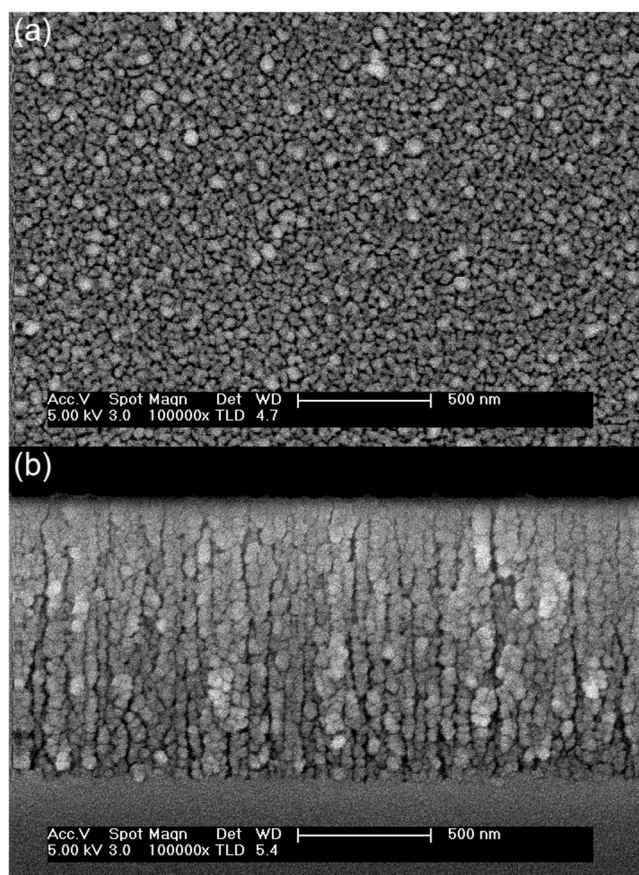


**Figure 3.** Top-view and cross-sectional FESEM images of a typical hybrid n-PS/Ag layer. The n-PS layer was grown using a current density of 60 mA/cm<sup>2</sup> and the silver nanoparticles were electrodeposited for 4 min. The Ag nanoparticles (bright areas) are rounded with diameters in the 30–65 nm range.

distilled in water for another 5 min and finally dried with a mild stream of dry nitrogen. This process leads to the formation of a hybrid n-PS/Ag thin film.

In all, four different sets of n-PS and hybrid n-PS/Ag layers were prepared as detailed in Table 1, to study the effects of porosity, thickness, and the volumetric proportion of silver on the optical response characteristics.

**Morphological characterization.** Top-view and cross-sectional images of every sample were acquired using a Philips XL 30S-FEG field emission scanning electron microscope (FESEM). The sizes of the pores of n-PS and the Ag nanoparticles were determined from these FESEM images using the ImageJ software.

**Optical characterization.** *Specular reflection.* White light from a halogen source (HL-2000, Ocean Optics, Dunedin, Florida, USA) was passed through a fiber-optic cable and then through a linear polarizer

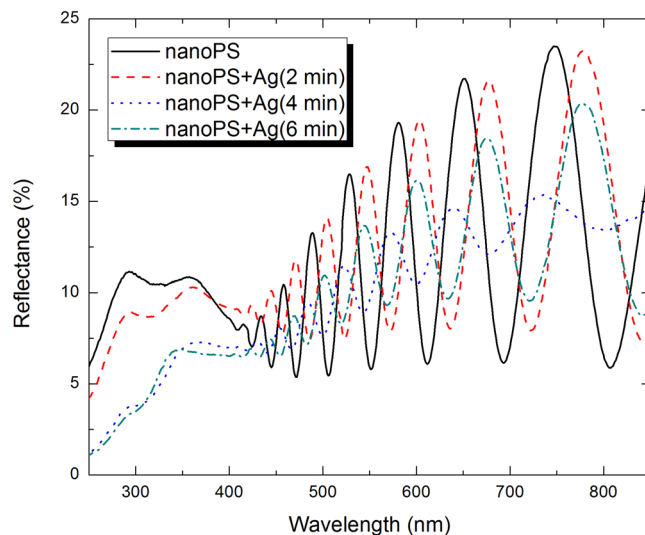


**Figure 4.** Overall reflectance spectra of 1.4- $\mu\text{m}$ -thick high-porosity n-PS and hybrid n-PS/Ag layers for different durations of infiltration of silver nanoparticles by electrodeposition (2, 4, and 6 min).

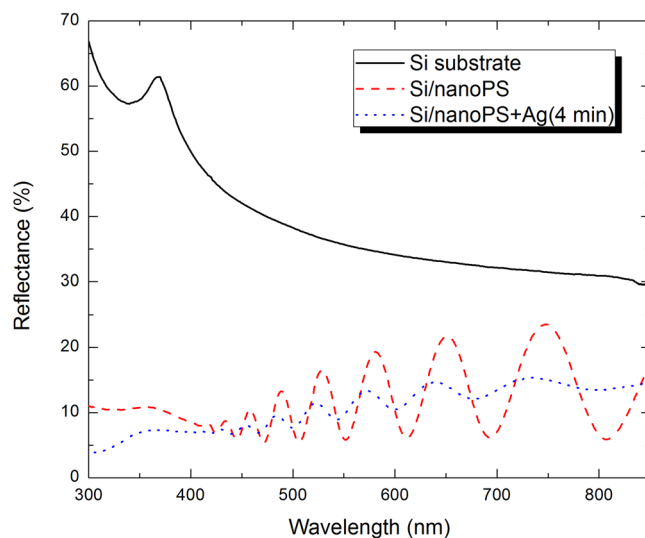


**Figure 5.** Overall reflectance spectra of bulk silicon substrate, a 1.4- $\mu\text{m}$ -thick high-porosity n-PS layer on a silicon substrate, and a 1.4- $\mu\text{m}$ -thick high-porosity n-PS layer (on a silicon substrate) infiltrated by silver nanoparticles during 4-min electrodeposition.

(GT10, ThorLabs, Newton, NJ, USA) to be incident upon the sample to be characterized. The reflected light was passed through a second linear polarizer (GT10, ThorLabs) and then through a fiber-optic cable to a CCD spectrometer (HRS-BD1-025, Mightex Systems, Pleasanton, CA, USA). All measurements were taken in a dark room and background noise was removed from the measured data. Co-polarized specular reflectances ( $R_{ss}$  and  $R_{pp}$ ) and cross-polarized specular reflectances ( $R_{ps}$  and  $R_{sp}$ ) were measured for the angle of incidence  $\theta_{inc}$  in the  $10^\circ$ – $70^\circ$  range as functions of the free-space wavelength  $\lambda_o$  in the 400–900 nm visible and near-infrared spectral regimes. The angle of incidence is measured with respect to the perpendicular to the illuminated face of the sample, with  $\theta_{inc} = 0^\circ$  for normal incidence. The first subscript on a specular reflectance denotes the linear polarization state of light collected by the detector, while the second subscript denotes the linear polarization state of light impinging on the sample. Care was taken to remove the effects of ambient light, as described elsewhere<sup>14</sup>.

**Overall reflection.** The overall reflectance spectrum for  $\lambda_o$  in the 250–900 nm wavelength regime was acquired using a double-beam spectrophotometer (V-560, JASCO International, Tokyo, Japan) equipped with an integrating sphere in order to collect both diffuse and specular reflections, with unpolarized light being incident at angle  $\theta_{inc} = 10^\circ$  (i.e., almost normally) on the sample. The photometric accuracy is specified by the manufacturer to be better than 0.3%.

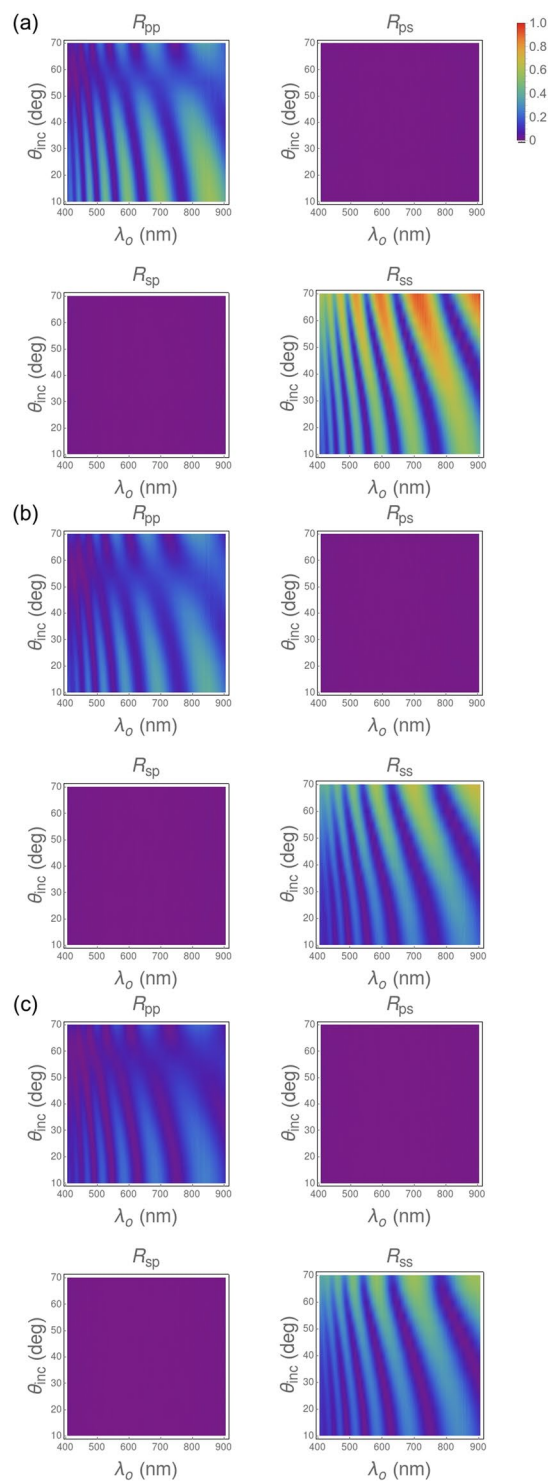


**Figure 6.** Dependences on  $\lambda_o$  and  $\theta_{inc}$  of the measured specular reflectances of (a) a 1- $\mu\text{m}$ -thick high-porosity n-PS layer, (b) a 1- $\mu\text{m}$ -thick high-porosity hybrid n-PS/Ag layer after silver infiltration for 15 min, and (c) a 1- $\mu\text{m}$ -thick high-porosity hybrid n-PS/Ag layer after silver infiltration for 4 min.

## Experimental Results

Figure 2 shows top-view and cross-sectional FESEM images of a typical n-PS layer grown by the electrochemical etch of a monocrystalline silicon wafer. Clearly, the electrochemical fabrication process delivers a porous columnar structure. For low-porosity n-PS layers (fabrication current density of 20 mA/cm<sup>2</sup>), the pore diameter is in the 5–15 nm range, as determined from FESEM image analysis, but that range changes to 15–35 nm in the case of high-porosity n-PS layers (60 mA/cm<sup>2</sup>).

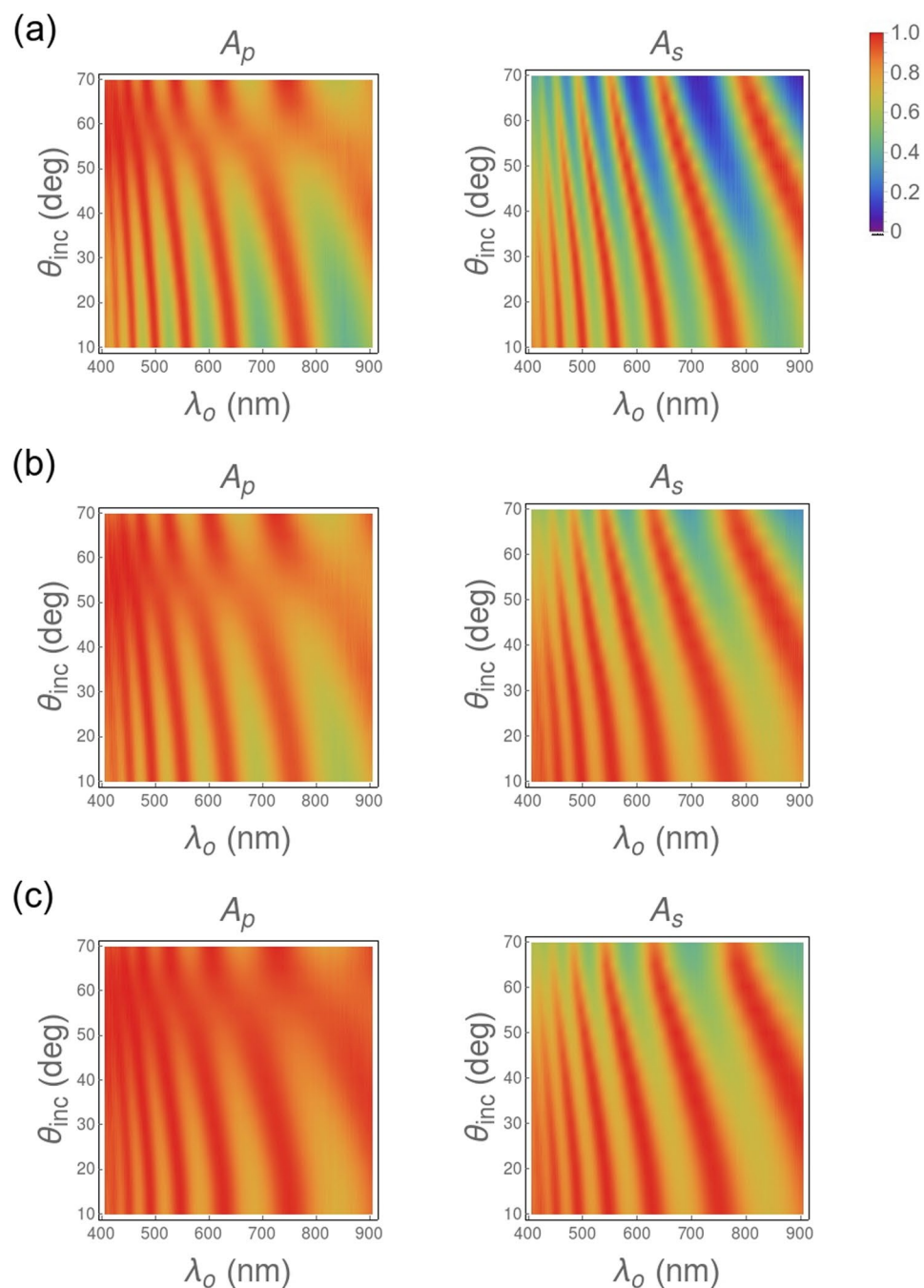


**Figure 7.** Dependences on  $\lambda_o$  and  $\theta_{inc}$  of the absorptances of (a) a 1- $\mu\text{m}$ -thick high-porosity n-PS layer, (b) a 1- $\mu\text{m}$ -thick high-porosity hybrid n-PS/Ag layer after silver infiltration for 15 min, and (c) a 1- $\mu\text{m}$ -thick high-porosity hybrid n-PS/Ag layer after silver infiltration for 4 min.

In Fig. 3, top-view and cross-sectional FESEM images of a typical hybrid n-PS/Ag layer grown onto silicon are presented. The sample comprises a high-porosity n-PS layer (current density 60 mA/cm<sup>2</sup>) in which silver nanoparticles were infiltrated for 4 min. The FESEM images show that the fabrication process leads to a quite homogeneous distribution of silver nanoparticles on the surface and inside the n-PS layer, the nanoparticle diameter ranging from 30–65 nm as determined by image analysis. Accordingly, given their characteristic small feature sizes, both the n-PS and the hybrid n-PS/Ag layers can be treated as homogeneous media from an optical standpoint at any wavelength  $\lambda_o$  exceeding about 200 nm.

Aiming at increasing optical absorption in the hybrid n-PS/Ag layers, we controlled the volumetric fraction of silver nanoparticles by using three different electrodeposition durations: namely, 2, 4, and 6 min. From the overall reflectance spectra shown in Fig. 4, we concluded that the differences between neighboring maxima and minima are the least when the electrodeposition duration was 4 min.

Reflection reduction after electrodeposition for 2 min can be attributed to increased absorption due to a strong interaction between free electrons in the silver nanoparticles and the incident electromagnetic radiation<sup>15</sup>. Reflection reduction is enhanced after electrodeposition for 4 min, as a consequence of increased absorption due to a larger number density of silver nanoparticles. However, increasing the electrodeposition duration to 6 min results in increased reflection, because the even larger number density of silver nanoparticles leads to the percolation effect<sup>16,17</sup>, the hybrid n-PS/Ag layer acquiring a strongly metallic character that inhibits refraction into the layer.

The overall reflectance spectra of the high-porosity n-PS layers and the best hybrid n-PS/Ag layers are shown in Fig. 5 in addition to the overall reflectance spectrum of a silicon wafer. It is evident that the fabrication of n-PS onto silicon substrates results in a remarkable reduction of the average overall reflectance and that further reflection reduction occurs on infiltration by silver nanoparticles. This effect is attributable to increased optical absorption provided by the silver nanoparticles in consequence of the high values of the imaginary part of the refractive index of silver in the chosen spectral regime<sup>18–20</sup>. Additionally, the observed shifts in the reflectance maxima and minima can be attributed to the changes in the spectrum of the complex-valued effective refractive index as a consequence of: first, due to the creation of pores due to electrochemical etching and, second, to the electrodeposition of silver nanoparticles.

Figure 6 shows characteristic two-dimensional density plots of co-polarized and cross-polarized specular reflectances as functions of  $\lambda_o$  and  $\theta_{inc}$  for a n-PS layer and two hybrid n-PS/Ag layers grown onto monocrystalline substrates. First, it is worth noticing that the two cross-polarized reflectances ( $R_{ps}$  and  $R_{sp}$ ) are negligible for all n-PS layers and hybrid n-PS/Ag layers, independently of their porosity and thickness. Therefore, materials of both types can be considered to be isotropic in the plane normal to the thickness direction. Second, we found that the reflectance spectra did not change when the sample was translated transversely to the path of the incident light beam. Therefore, materials of both types can be considered to be effectively homogeneous, as also indicated by the FESEM images.

The reflectance spectra in Fig. 6 contain several bands having their origin in classical interference effects. The bright bands (or fringes) correspond to interference maxima while the dark bands correspond to interference minima. We ascertained from the reflectance spectra of all 18 samples mentioned in Table 1 that the number of bright bands increases with the sample thickness. Also, there is an evident dependence of the width of the bright bands on the angle of incidence, which is a consequence of increased optical path for larger angles of incidence.

In the plots of  $R_{pp}$  in Fig. 6, we see a dark horizontal region corresponding to low reflection in the vicinity of  $\theta_{inc} = 60^\circ$ , but a similar dark region is absent in the plots of  $R_{ss}$ . This is indicative of the pseudo-Brewster effect<sup>21</sup>. As  $\theta_{inc}$  increases further, both  $R_{pp}$  and  $R_{ss}$  increase rapidly towards unity.

We ascertained experimentally that no light was transmitted through any of the samples. Therefore, we defined the absorptances  $A_p = 1 - (R_{pp} + R_{sp})$  and  $A_s = 1 - (R_{ss} + R_{ps})$  and plotted them as functions of  $\lambda_o$  and  $\theta_{inc}$  in Fig. 7 for a n-PS layer and two hybrid n-PS/Ag layers grown onto silicon substrates. Clearly in this figure,  $A_p$  is larger than  $A_s$  for all three samples. Besides, the comparison of Fig. 7a,b allows the conclusion that infiltration of n-PS layers by silver nanoparticles results in increased absorption, given that broader and more intense absorption bands are displayed. This enhancement is observed for both  $A_p$  and  $A_s$ , although it is more pronounced for  $A_s$ . Absorption is further increased once the density of silver particles in the nanoporous structure is optimized, as shown in Fig. 7c. Accordingly, it can be concluded that the infiltration of n-PS by silver nanoparticles results in increased absorption and, additionally, optical absorption can be controlled by controlling the density of the infiltrant silver nanoparticles.

## Concluding Remarks

The use of nanostructured porous silicon (n-PS) and hybrid n-PS/Ag layers grown onto silicon as wideband optical absorbers with potential applications in the fields of light sensing and light harvesting was experimentally explored by investigating the dependences of the optical reflectances and absorptances on the thickness and porosity of n-PS and hybrid n-PS/Ag layers and the number density of the infiltrant silver nanoparticles.

Our data show that the absorption characteristics of the hybrid n-PS/Ag layers can be controlled by selecting the appropriate combination of thickness and porosity of the n-PS layers, together with the density of infiltrant silver nanoparticles. The wideband optical absorption characteristics of the hybrid n-PS/Ag layers are expected to contribute to increased efficiency of light-harvesting devices and photodetectors given by increased field-of-view for both *s*- and *p*-polarization states of incident light over a broad spectral regime.

## References

- Uhlir, A. Electrolytic Shaping of Germanium and Silicon. *Bell Syst. Tech. J.* **35**, 333–347 (1956).
- Canham, L. T. Silicon quantum wire array fabrication by electrochemical and chemical dissolution of wafers. *Appl. Phys. Lett.* **57**, 1046–1048 (1990).
- Canham, L. T. (ed.) *Handbook of Porous Silicon*, 2nd ed. (Springer 2018).
- Martín-Palma, R. J., Pascual, L., Herrero, P. & Martínez-Duart, J. M. Direct determination of grain sizes, lattice parameters, and mismatch of porous silicon. *Appl. Phys. Lett.* **81**, 25–27 (2002).
- Martín-Palma, R. J., Pascual, L., Landa, A., Herrero, P. & Martínez-Duart, J. M. High-resolution transmission electron microscopic analysis of porous silicon/silicon interface. *Appl. Phys. Lett.* **85**, 2517–2519 (2004).
- Martín-Palma, R. J., Pascual, L., Herrero, P. & Martínez-Duart, J. M. Monte Carlo determination of crystallite size of porous silicon from x-ray line broadening. *Appl. Phys. Lett.* **87**, 211906–1–3 (2005).
- Pascual, L., Martín-Palma, R. J., Landa-Cánovas, A. R., Herrero, P. & Martínez-Duart, J. M. Lattice distortion in nanostructured porous silicon. *Appl. Phys. Lett.* **87**, 251921–1–3 (2005).
- Sailor, M. J. *Porous Silicon in Practice: Preparation, Characterization and Applications* (Wiley, 2012).
- Torres-Costa, V., Martín-Palma, R. J. & Martínez-Duart, J. M. Optical constants of porous silicon films and multilayers determined by genetic algorithms. *J. Appl. Phys.* **96**, 4197–4203 (2004).

10. Torres-Costa, V. & Martín-Palma, R. J. Application of nanostructured porous silicon in the field of optics. A review. *J. Mater. Sci.* **45**, 2823–2838 (2010).
11. Atwater, H. A. & Polman, A. Plasmonics for improved photovoltaic devices. *Nat. Mater.* **9**, 205–213 (2010).
12. Oh, J., Yuan, H.-C. & Branz, H. M. An 18.2%-efficient black-silicon solar cell achieved through control of carrier recombination in nanostructures. *Nat. Nanotechnol.* **7**, 743–748 (2012).
13. Ko, E. *et al.* Electrochemical Fabrication of Nanostructures on Porous Silicon for Biochemical Sensing Platforms. *Anal. Sci.* **32**, 681–686 (2016).
14. Vepachedu, V., McAtee, P. D. & Lakhtakia, A. Nonexhibition of Bragg phenomenon by chevronic sculptured thin films: experiment and theory. *J. Nanophotonics* **11**, 036018–1–15 (2017).
15. Mackay, T. G. On the effective permittivity of silver-insulator nanocomposites. *J. Nanophotonics* **1**, 019501–1–5 (2007).
16. McLachlan, D. S., Priou, A., Chenierie, I., Issac, E. & Henry, F. Modeling the Permittivity of Composite Materials with a General Effective Medium Equation. *J. Electromag. Waves Appl.* **6**, 1099–1131 (1992).
17. Mackay, T. G. & Lakhtakia, A. Percolation thresholds in the homogenization of spheroidal particles oriented in two directions. *Opt. Commun.* **259**, 727–737 (2006).
18. Martín-Palma, R. J. & Martínez-Duart, J. M. Accurate determination of the optical constants of sputter-deposited Ag and SnO<sub>2</sub> for low emissivity coatings. *J. Vac. Sci. Technol. A* **16**, 409–412 (1998).
19. Martín-Palma, R. J., Vázquez, L., Martínez-Duart, J. M. & Malats-Riera, A. Silver-based low-emissivity coatings for architectural windows: Optical and structural properties. *Sol. Energy Mater. Sol. Cells* **53**, 55–66 (1998).
20. Martín-Palma, R. J., Gago, R., Vinnichenko, M. & Martínez-Duart, J. M. In-depth optical and structural study of silver-based low-emissivity multilayer coatings for energy-saving applications. *J. Phys. D: Appl. Phys.* **37**, 1554–1557 (2004).
21. Kim, S. Y. & Vedam, K. Analytic solution of the pseudo-Brewster angle. *J. Opt. Soc. Am. A* **3**, 1772–1773 (1986).

## Acknowledgements

R.J.M.-P. thanks *Ministerio de Educación, Cultura y Deporte* (Spain) for funding under grant reference number PRX17/00095. P.D.M. and A.L. thank the Charles Godfrey Binder Endowment at Penn State for continued support of their research activities. R.R. thanks the Egyptian Ministry of Higher Education, Missions section, for funding under Joint Supervision grant, call 2015–2016.

## Author Contributions

R.J.M.-P. and A.L. conceived and supervised the study and designed the experiments. P.D.M. carried out the specular reflectance measurements. R.R. fabricated the n-PS and hybrid n-PS/Ag layers, acquired the FESEM images, and was in charge of the overall reflectance optical characterization. R.J.M.-P. drafted the initial version of the manuscript. All the authors commented on the results, provided ideas for the study, and reviewed the manuscript.

## Additional Information

**Competing Interests:** The authors declare no competing interests.

**Publisher's note:** Springer Nature remains neutral with regard to jurisdictional claims in published maps and institutional affiliations.



**Open Access** This article is licensed under a Creative Commons Attribution 4.0 International License, which permits use, sharing, adaptation, distribution and reproduction in any medium or format, as long as you give appropriate credit to the original author(s) and the source, provide a link to the Creative Commons license, and indicate if changes were made. The images or other third party material in this article are included in the article's Creative Commons license, unless indicated otherwise in a credit line to the material. If material is not included in the article's Creative Commons license and your intended use is not permitted by statutory regulation or exceeds the permitted use, you will need to obtain permission directly from the copyright holder. To view a copy of this license, visit <http://creativecommons.org/licenses/by/4.0/>.

© The Author(s) 2019

### Abbreviations in chapter 3

n-PS	Nanostructured porous Silicon
FESEM	Field emission scanning electron microscope
J	current density
(R <sub>ss</sub> and R <sub>pp</sub> )	Co-polarized specular reflectances
(R <sub>ps</sub> and R <sub>sp</sub> )	cross-polarized specular reflectances
$\theta_{inc}$	Angle of incidence
$\lambda_0$	the free-space wavelength



## **Chapter 4:**

### **Electrical Characterization of MIS Schottky Barrier Diodes Based on Nanostructured Porous Silicon and Silver Nanoparticles with Applications in Solar Cells**

R. Ramadan, R. J. Martín-Palma, *Energies*, 13(9), (2020), 2165.

---

Article

# Electrical Characterization of MIS Schottky Barrier Diodes Based on Nanostructured Porous Silicon and Silver Nanoparticles with Applications in Solar Cells

Rehab Ramadan <sup>1,2,\*</sup>  and Raúl J. Martín-Palma <sup>1,3</sup> 

<sup>1</sup> Departamento de Física Aplicada, Universidad Autónoma de Madrid, 28049 Madrid, Spain; rauljose.martin@uam.es

<sup>2</sup> Department of Physics, Faculty of Science, Minia University, Minia 61519, Egypt

<sup>3</sup> Instituto Universitario de Ciencia de Materiales “Nicolás Cabrera”, Universidad Autónoma de Madrid, 28049 Madrid, Spain

\* Correspondence: rehab.ramadan@uam.es

Received: 25 March 2020; Accepted: 23 April 2020; Published: 1 May 2020



**Abstract:** The accurate determination of the electrical properties of photovoltaic devices is of utmost importance to predict and optimize their overall optoelectronic performance. For example, the minority carrier lifetime and the carrier diffusion length have a strong relationship with the carrier recombination rate. Additionally, parasitic resistances have an important effect on the fill factor of a solar cell. Within this context, the alternating current (AC) and direct current (DC) electrical characteristics of Si-based metal–insulator–semiconductor (MIS) Schottky barrier diodes with the basic structure Al/Si/TiO<sub>2</sub>/NiCr were studied, aiming at using them as photovoltaic devices. The basic diode structure was modified by adding nanostructured porous silicon (nanoPS) layers and by infiltrating silver nanoparticles (AgNPs) into the nanoPS layers, leading to Al/Si+nanoPS/TiO<sub>2</sub>/NiCr and Al/Si+nanoPS+AgNPs/TiO<sub>2</sub>/NiCr structures, respectively. The AC electrical properties were studied using a combination of electrochemical impedance spectroscopy and Mott–Schottky analysis, while the DC electrical properties were determined from current–voltage measurements. From the experimental results, an AC equivalent circuit model was proposed for the three different MIS Schottky barrier diodes under study. Additionally, the most significant electrical parameters were calculated. The results show a remarkable improvement in the performance of the MIS Schottky barrier diodes upon the addition of hybrid nanoPS layers with embedded Ag nanoparticles, opening the way to their use as photovoltaic devices.

**Keywords:** MIS Schottky barrier diodes; nanoporous silicon; silver nanoparticles; electrochemical impedance spectroscopy; Mott–Schottky theory

## 1. Introduction

During the past few years, there has been a great interest towards the integration of nanostructured porous silicon (nanoPS) with silicon micro- and optoelectronic devices [1,2]. For applications in these fields, including as photodiodes and solar cells, the efficiency and performance of the electrical contacts to nanoPS is a key factor. In particular, it is of great importance to determine the specific mechanisms of carrier transport, since these will play a crucial role in the performance of nanoPS-based devices. Previous low-temperature DC studies of metal/nanoPS/Si structures showed rectifying behavior, and the subsequent analysis of their current-voltage (*I*-*V*) characteristics allowed identification of them as metal–insulator–semiconductor (MIS) Schottky junctions [3,4].

MIS Schottky junctions have found important applications in the broad fields of micro- and optoelectronics, including diodes [5], near-infrared (NIR) photodetectors [6], photoelectrochemical

water oxidation devices [7], and photovoltaic solar cells [8]. In the particular case of Schottky barrier solar cells, the presence of an insulator thin film avoids the principal shortcoming of metal–semiconductor (MS) Schottky barriers, which is their typically low open-circuit voltage,  $V_{oc}$  [9]. In fact, it has been found by several authors that the use of MIS junctions results in increased  $V_{oc}$ , compared to that of MS Schottky barrier solar cells [10–13]. This increase in  $V_{oc}$  leads to (1) decreased reverse saturation current density associated with thermionic emission in the Schottky barrier, (2) increased value of the diode ideality factor, and/or (3) increased effective Schottky barrier height [14]. In fact, the key transport mechanisms of MIS Schottky barrier diodes are tunneling through the insulator or the interfacial layer by the majority carriers or diffusion current due to the minority carriers [15,16]. This effect is drastically manifested in nanoPS, given its high specific surface area.

A thorough study of the AC and DC electrical properties of MIS Schottky barrier diodes is essential to understand their fundamental electrical conduction properties. In this line, electrochemical impedance spectroscopy (EIS) enables determination of the electrical parameters which characterize the electrical conduction properties of the interfaces of a device in a given frequency range [17]. EIS has been previously used to investigate the internal electrical properties of the interfaces of multilayer structures, such as light-emitting diodes [18], electrochromic smart windows [19,20],  $\text{Li}^+$ -ion batteries, [21] and photovoltaic devices [17], by establishing an equivalent circuit model. Capacitance-voltage ( $C$ - $V$ ) characterization at a fixed frequency allows evaluation of other essential electrical parameters. Within this context, the Mott–Schottky model [22] allows determination of the built-in potential, semiconductor type, and doping density. Since not all the electrical conduction parameters for a given device can be obtained from EIS and  $C$ - $V$  measurements, DC current–voltage ( $I$ - $V$ ) analysis provides some additional semiconductor device electrical parameters, including diffusion and recombination currents in dark and bulk resistances [23].

The main aim of the present work is to study the AC and DC electrical conduction properties of three different Si-based MIS Schottky barrier diodes to assess their potential use in the field of photovoltaics. The optoelectronic properties of similar structures were recently studied [24]. The basic structure of the MIS Schottky barrier devices is  $\text{Al/Si/TiO}_2/\text{NiCr}$ , with the  $\text{Al/Si}$  interface behaving as an ohmic contact. A variation of the basic device includes a nanoPS layer grown on the Si substrate, leading to diodes with the structure  $\text{Al/Si+nanoPS/TiO}_2/\text{NiCr}$ . The last modification includes a layer consisting of silver nanoparticles (AgNPs) embedded into nanoPS, resulting in the structure  $\text{Al/Si+nanoPS+AgNPs/TiO}_2/\text{NiCr}$ . The AC electrical properties were determined using a combination of EIS and  $C$ - $V$  measurements, while the DC electrical properties were obtained from  $I$ - $V$  measurements. From the experimental EIS results, an AC equivalent circuit model was proposed for the three different MIS Schottky devices, and the internal resistance and capacitance associated to each interface were calculated. Additionally, both the minority carrier lifetimes and minority carrier diffusion coefficients were calculated. From the  $C$ - $V$  results at fixed frequencies, the built-in potential, doping concentration, and the type of the semiconductor were determined. Finally, the reverse saturation current, ideality factor, parasitic resistances, and built-in potential were obtained from the experimental  $I$ - $V$  data.

## 2. Experimental

### 2.1. Fabrication of the Si-Based MIS Schottky Barrier Diodes

#### 2.1.1. Fabrication of the NanoPS Layers

Low-resistivity ohmic back contacts to boron-doped (p-type) silicon wafers (100) orientation and resistivity of 25–30  $\Omega$ -cm) were fabricated by electron beam evaporation of 150 nm-thick Al layers and subsequent thermal annealing in a nitrogen atmosphere for 5 min. The Si wafers were cut into  $1.5 \times 1.5 \text{ cm}^2$  pieces, each of which were mounted in a sample holder and exposed to the etching solution, consisting of a 1:6 HF (48 wt%):dimethyl formamide (99 wt%) mixture. The native oxide layer was removed before starting the etching process by immersing, for 60 s, the Si pieces in a HF:H<sub>2</sub>O (1:20) solution. The anodization process was carried out under an applied current density of 10 mA/cm<sup>2</sup>

*Energies* 2020, 11, x FOR PEER REVIEW, 3 of 16  
 and a fixed anodization time of 120 s, leading to nanoPS layers with thickness of around 120 nm. Once the etching process was completed, the nanoPS layers grown onto Si were cleaned with ethanol to remove any residuals from the HF solution and finally, blow-dried with a mild stream of dry nitrogen. The experimental setup of the anodization process has previously been described and is schematically presented in [25].

### 2.1.2. Infiltration of Silver Nanoparticles (AgNPs)

Silver nanoparticles (AgNPs) were grown inside the nanoPS layers using an electrochemical deposition process described in previous work [25]. An aqueous solution of silver nitrate, sodium citrate and nitric acid (pH = 3) was used. The current density was, in all cases,  $1 \mu\text{A}/\text{cm}^2$  and the infiltration time was 4 min. The electrochemical deposition process led to the formation of hybrid layers composed of nanoPS and silver nanoparticles (nanoPS+AgNPs).

### 2.1.3. Spin Coating of $\text{TiO}_2$ Thin Films

A solution of titanium isopropoxide ( $\text{Ti}[\text{OCH}(\text{C}_2\text{H}_5)_2]_4$ ) in ethanol was prepared with 0.40 M concentration. Afterwards, 115  $\mu\text{L}$  of HCl acid was added to the solution to induce an acid catalysis to prevent nanoPS from damage. The solution was stirred at 3000 rpm at room temperature for 30 min to obtain a clear solution. A total of 60  $\mu\text{L}$  of the solution was cast on either the Si substrate, the nanoPS layers, or the nanoPS+AgNPs hybrid layers at a spinning speed of 3000 rpm for 30 s. Finally, the resulting  $\text{TiO}_2$  thin films were annealed on a hot plate at  $150^\circ\text{C}$  for 5 min to evaporate the remaining solvents.

### 2.1.4. Ni/Cr Top Contact

Electron beam evaporation was used to deposit 100 nm-thick Ni/Cr (80%/20%) top contacts on the  $\text{TiO}_2$  thin films. The base pressure was  $2.5 \times 10^{-5}$  mbar, and the evaporation time was 5 minutes. A metallic mask was used to define the geometry at the microscale of the Ni/Cr front contacts. The mask was used to define the geometry at the microscale of the Ni/Cr front contacts. The area was  $0.15 \text{ cm}^2$ .

Figure 1 shows the final structure of the Al/Si+nanoPS+AgNPs/ $\text{TiO}_2$ /Ni/Cr Schottky barrier diodes. In addition to this basic device, two other Schottky barrier diodes were fabricated to compare their performance, namely Al/Si/ $\text{TiO}_2$ /NiCr and Al/Si+nanoPS/ $\text{TiO}_2$ /NiCr.

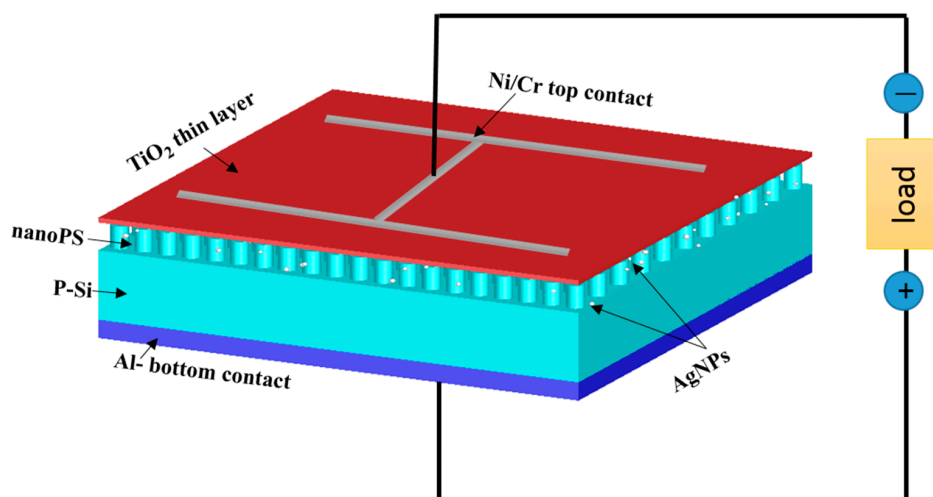


**Figure 1.** Schematic illustration of the structure of the Al/Si+nanoPS+AgNPs/ $\text{TiO}_2$ /Ni/Cr Schottky barrier diodes connected to a load. In this case, the active layer is Si+nanoPS+AgNPs.

In summary, the structure of the three different Si-based MIS Schottky barrier diodes analyzed in this work is Al/active layer/ $\text{TiO}_2$ /NiCr, the active layer being respectively Si, Si+PS+PS, Si+nanoPS+AgNPs. Therefore, the electrical conduction properties of the different active layers are expected to have a pivotal role in the overall performance of the diodes.

or Si+nanoPS+AgNPs. Therefore, the electrical conduction properties of the different active layers are expected to have a pivotal role in the overall performance of the diodes.

Energies 2020, 11, x FOR PEER REVIEW  
2.2. Characterization

4 of 16

**2.2. Characterization**  
The morphologies of the different layers and interfaces were analyzed by field emission scanning electron microscopy (FESEM). The morphologies of the different layers and interfaces were analyzed by field emission scanning electron microscopy (FESEM) (XL-40 FEG, Philips, Eindhoven, The Netherlands) operated at 5 kV. Alternating current (AC) and direct current (DC) electrical measurements were carried out using a potentiostat instruments (SP-150, BioLogic, Seyssinet-Pariset, France). For electrochemical impedance spectroscopy (EIS) measurements, a voltage amplitude of 500 mV and a frequency range between 1 Hz and 1 MHz were used. Capacitance-voltage (C-V) characterization was performed at three specific frequencies, 1 KHz, 5 KHz, and 10 KHz, under reverse bias from 0 V to -1 V with a scan rate of 20 mV/s. For current-voltage (I-V) measurements, the applied potential was varied between -1.5 and +1.5 V and the scan rate was set at 5 mV/s. All the measurements were carried out at room temperature in a Faraday cage to shield the electrical measurements from any external signals.

### 3. Experimental Results

#### 3.1. Morphology

Typical field emission scanning electron microscopy (FESEM) images of the nanoPS layers after the electrochemical deposition of Ag nanoparticles (AgNPs) are presented in Figure 2a, b. These images confirm the infiltration of these nanoparticles inside the pores. It was determined that the diameter of the AgNPs typically ranges between 5 and 15 nm. Figure 2c, d portray cross-sectional and top views of characteristic nanoPS+AgNPs layers coated with a very thin layer of TiO<sub>2</sub>. The images confirm the extremely small thickness of the TiO<sub>2</sub> layer (~10 nm), given the notable conformity observed.

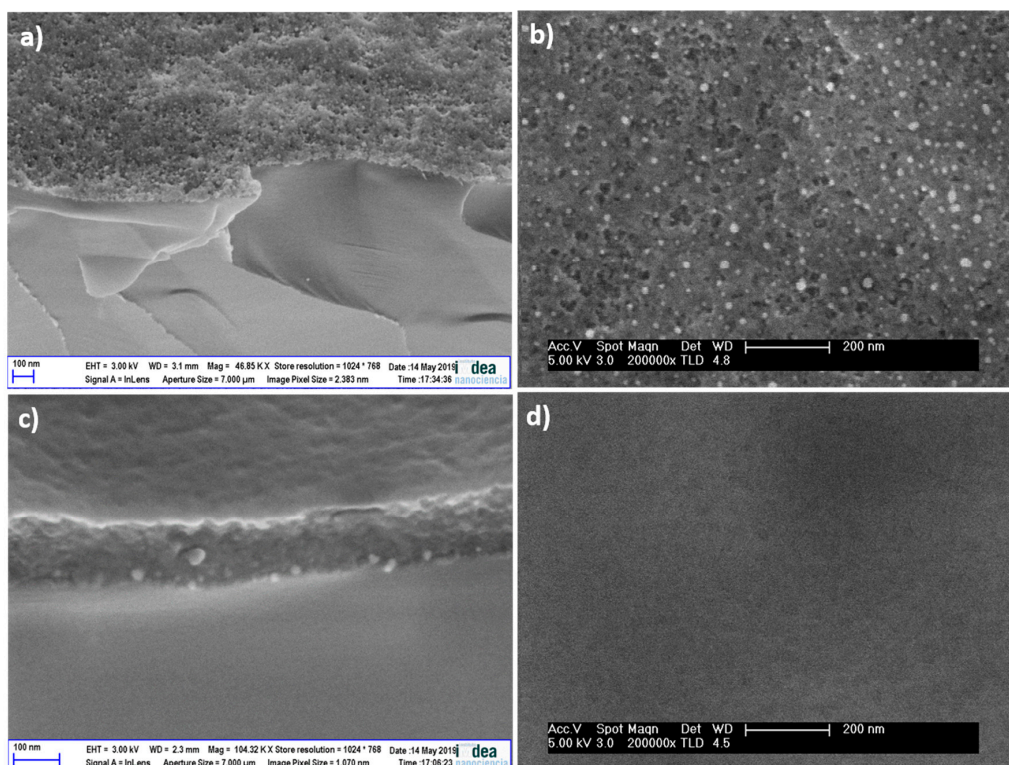


**Figure 2.** (a) Cross-sectional and (b) top views FESEM image of a typical nanoPS+AgNP layer (c) and (d) the same views upon deposition of a conformal TiO<sub>2</sub> thin film.

### 3.2. Electrical Characterization

#### 3.2.1. AC Electrical Measurements

EIS analysis, given its power and versatility, was used to determine the electrical transport properties through the interfaces of the three different Si-based MIS Schottky diodes. From the fitting of the Nyquist plots (Figure 3), a full equivalent circuit model for these devices was proposed. The equivalent circuit, which includes an intricate combination of resistances (R), capacitors (C), and a constant phase element (Q), is depicted in Figure 4. For the interpretation of the results, it must be kept in mind that resistance is a parameter which is strongly related to the carrier transport properties, while a capacitance is linked to the carrier accumulation and distribution and to the presence of defect traps in the interface [26]. Furthermore, the constant phase element (CPE) is a circuit element that models an imperfect capacitor. Its non-linear capacitance behavior is generally attributed to inhomogeneities in the interface [26]. The differences in the impedance of the interfaces of the three MIS Schottky barrier diodes analyzed in this work will be analyzed in the following paragraphs.

$$C \equiv Q^{\frac{1}{a}} \cdot R^{\frac{1-a}{a}} \tag{1}$$

where Q is the CPE and the factor a is an index which indicates the degree of "perfection" of this element. This index can vary between 0 and 1, with 0 describing a perfect resistor and 1 a perfect capacitor [26]. The differences in the impedance of the interfaces of the three MIS Schottky barrier diodes analyzed in this work will be analyzed in the following paragraphs.

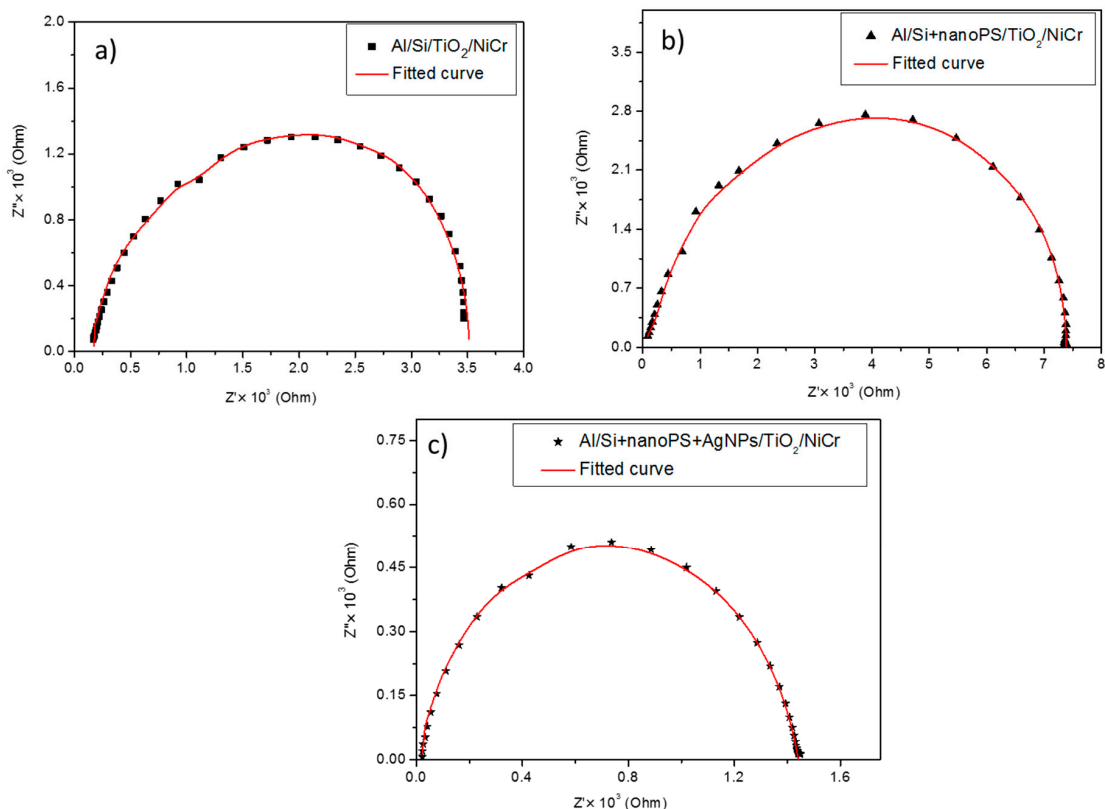


Figure 3. Nyquist diagrams and impedance fittings corresponding to (a) Al/Si/TiO<sub>2</sub>/NiCr diodes, (b) Al/Si+nanoPS/TiO<sub>2</sub>/NiCr diodes, and (c) Al/Si+nanoPS+AgNPs/TiO<sub>2</sub>/NiCr diodes.

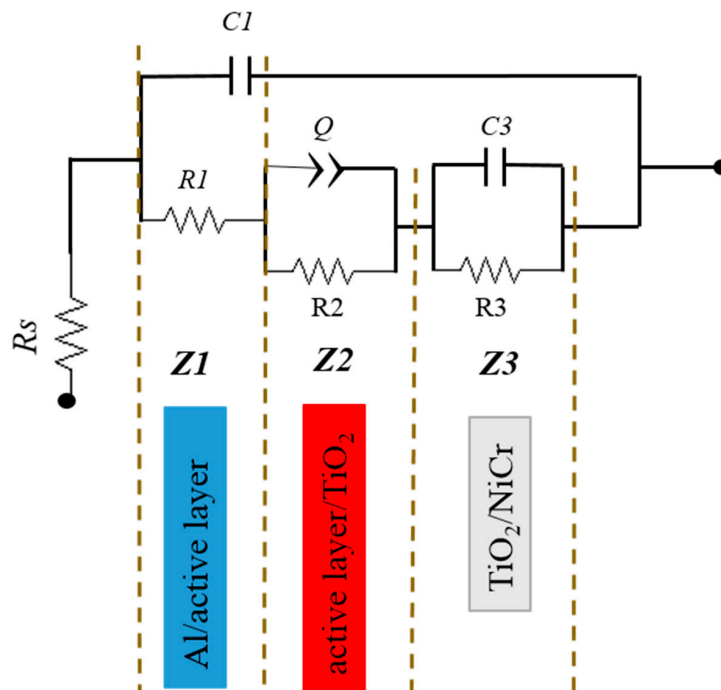
Figure 3 shows the Nyquist plots for the three MIS Schottky barrier diodes, i.e., Al/Si/TiO<sub>2</sub>/NiCr, Al/Si+nanoPS/TiO<sub>2</sub>/NiCr, and Al/Si+nanoPS+AgNPs/TiO<sub>2</sub>/NiCr. As each MIS structure has three different interfaces, every interface has been attributed to a semicircle in the corresponding Nyquist plot

Figure 3 shows the Nyquist plots for the three MIS Schottky barrier diodes, i.e., Al/Si/TiO<sub>2</sub>/NiCr, Al/Si+nanopPS/TiO<sub>2</sub>/NiCr, and Al/Si+nanopPS+AgNPs/TiO<sub>2</sub>/NiCr. As each MIS structure has three so that each semicircle is associated to an individual electrical transport process. Table 1 summarizes the interfaces under study for the three Si-based Schottky diodes. Table 1 summarizes the interfaces under study for the three Si-based Schottky diodes.

**Table 1.** Summary of the interfaces for the three Schottky junction diodes under analysis.

Schottky Diode Structure	1st Interface	2nd Interface	3rd Interface
Al/Si/TiO <sub>2</sub> /NiCr	Al/Si	Si/TiO <sub>2</sub>	TiO <sub>2</sub> /NiCr
Al/Si+nanopPS/TiO <sub>2</sub> /NiCr	Al/Si+nanopPS	Si+nanopPS/TiO <sub>2</sub>	TiO <sub>2</sub> /NiCr
Al/Si+nanopPS+AgNPs/TiO <sub>2</sub> /NiCr	Al/Si+nanopPS+AgNPs	Si+nanopPS+AgNPs/TiO <sub>2</sub>	TiO <sub>2</sub> /NiCr

The best fitting of the equivalent circuit for the three Si-based devices was obtained using a series resistance and three parallel resistor-capacitor (RC) circuits, as shown in Figure 4, where each RC circuit shown in series in the Nyquist plots corresponds to a frequency. The low-frequency semicircle is attributed to the Al/active layer (1st interface), while the semicircle at mid-frequency is associated to the active layer/TiO<sub>2</sub> interface (2nd interface). The last semicircle at high frequency is attributed to the TiO<sub>2</sub>/NiCr interface (3rd interface). It must be pointed out that for the Al/Si+nanopPS/TiO<sub>2</sub>/NiCr Schottky barrier diodes, the Schottky barrier is deposited by layers in junction, given that we assume that there are no contacts between Si and nanopPS. In this regard, we consider that this is a heterostructure formed between two different semiconductors with different bandgaps, the bandgap of nanopPS being larger than that of Si [28,29]. It is also important to notice that electrical conduction through nanopPS is much lower than through Si, which is attributed to their very different conductivities [30,31]. What is more, since the silver nanoparticles do not form a continuous layer (as shown in Figure 2), we assume that the Si+nanopPS+AgNPs structure also represents just one active layer.



**Figure 4.** AC equivalent circuit model proposed to study the electrical behavior of the three Si-based MIS Schottky barrier diodes analyzed in this work. Depending on the particular diode, the active layer will be Si, Si+nanopPS, or Si+nanopPS+AgNPs.

Table 2 portrays a comparison between the RC elements for the interfaces of each device. Due to the very different active layer for each device, the electrical RC parameters are rather

dissimilar. It is observed that for the three active layer/TiO<sub>2</sub> interfaces, the electrical conduction of the Al/Si+nanoPS/TiO<sub>2</sub>/NiCr devices is lower than that of the Al/Si/TiO<sub>2</sub>/NiCr devices, most likely due to the formation of the nanopores in the heavily-doped regions of the Si substrate, leading to an effective reduction of the doping concentration [29]. The experimental results also show that the electrical conduction is notably increased in the devices based on nanoPS combined with metallic Ag nanoparticles. This behavior is attributed to increased electrical conduction due to the presence of the AgNPs embedded into the nanoPS layers. A comparable enhancement in the electrical conduction of silica nanofiber structures was recently observed upon incorporation of gold nanoparticles [32].

**Table 2.** Comparison between the electrical RC elements for the three Si-based MIS Schottky barrier diodes studied in this work.

Calculated Parameter	Device Structure		
	Al/Si/TiO <sub>2</sub> /NiCr	Al/Si+nanoPS/TiO <sub>2</sub> /NiCr	Al/Si+nanoPS+AgNPs/TiO <sub>2</sub> /NiCr
$R_s$ ( $\Omega$ )	173	51	23.2
$C_1$ (nf)	5.7	2.3	15.5
$R_1$ (k $\Omega$ )	0.6	0.7	0.05
$\tau_1$ ( $\mu$ s)	3.42	1.61	0.77
$Q$ (nS)	54	16.8	21
$a$	0.9	0.89	0.8
$C_2$ (nf)	4.01	0.91	0.04
$R_2$ (k $\Omega$ )	1.3	3.4	0.7
$\tau_2$ ( $\mu$ s)	5.21	3.09	0.03
$C_3$ (nf)	19.7	31.5	13.2
$R_3$ (k $\Omega$ )	1.5	3.4	0.518
$\tau_3$ ( $\mu$ s)	29.55	97.65	5.52

Additionally, the changes in the structure of the active layer could have an important effect on the electrical conduction properties of all the interfaces of the devices. The electrical conduction for the interface's Al/active layer and TiO<sub>2</sub>/NiCr decreases for the Al/Si/TiO<sub>2</sub>/NiCr devices, due to the large thickness of the TiO<sub>2</sub> thin films. Also, the reduction for the Al/Si+nanoPS/TiO<sub>2</sub>/NiCr devices is attributed to the lower conduction of nanoPS, compared to Si. However, the improved conduction for the Al/Si+nanoPS+AgNPs/TiO<sub>2</sub>/NiCr devices is attributed to the combination of the nanoPS and metallic nanoparticles.

The minority carrier lifetime ( $\tau$ ) for every interface can be obtained from the well-known relationship [33]:

$$\tau = RC \quad (2)$$

where  $R$  is the electrical resistance and  $C$  is the electrical capacitance at each interface. The results are compiled in Table 2. It can be observed that the Al/Si+nanoPS+AgNPs/TiO<sub>2</sub>/NiCr device shows the lowest values for  $\tau_1$ ,  $\tau_2$ , and  $\tau_3$ , which are associated with increased conduction. The observed increase in  $\tau_1$ ,  $\tau_2$ , and  $\tau_3$  for the Al/Si/TiO<sub>2</sub>/NiCr devices is related to the large thickness of the TiO<sub>2</sub> thin films and the large carrier recombination rates of Si [34], as previously indicated in the analysis of the Nyquist plots. The values obtained for  $\tau_1$ ,  $\tau_2$ , and  $\tau_3$  for the Al/Si+nanoPS/TiO<sub>2</sub>/NiCr devices are attributed to conduction losses associated with the porous structure of the nanoPS layers, as well as with the formation of defects on their surface [35]. The combination of the nanoPS layers with metallic nanoparticles has a notable effect on the electrical conduction at the active layer/TiO<sub>2</sub> interfaces, which leads to a small value of  $\tau_2$ . More specifically,  $\tau_2$  decreases from 3.09  $\mu$ s for the Al/Si+nanoPS/TiO<sub>2</sub>/NiCr devices to 0.03  $\mu$ s for the Al/Si+nanoPS+AgNPs/TiO<sub>2</sub>/NiCr devices.

Table 2 shows that  $C_1$  and  $C_2$  are lower for the Al/Si+nanoPS/TiO<sub>2</sub>/NiCr devices than for the Al/Si/TiO<sub>2</sub>/NiCr devices. The observed decrease in the capacitance at the two nanoPS interfaces could be due to the particular structure of the nanoPS layers, which would induce quite large leakage currents.



be due to the particular structure of the nanoPS layers, which would induce quite large leakage currents. However, at the TiO<sub>2</sub>/NiCr interface, the capacitance increased from 19.7 nF for the Al/Si/TiO<sub>2</sub>/NiCr devices to 31.5 nF for the Al/Si+nanoPS/TiO<sub>2</sub>/NiCr devices. This variation could be due to a more homogeneous TiO<sub>2</sub> thin film when grown on the nanoPS layers, as discussed above.

The minority carrier diffusion coefficient can be calculated using the thickness of the interfaces ( $L$ ) and  $\tau$ , by means of the following relationship [36]:

$$D = \frac{L^2}{\tau} \quad (3)$$

However, at the TiO<sub>2</sub>/NiCr interface, the capacitance increased from 19.7 nF for the Al/Si/TiO<sub>2</sub>/NiCr devices to 31.5 nF for the Al/Si+nanoPS/TiO<sub>2</sub>/NiCr devices. This variation could be due to a more homogeneous TiO<sub>2</sub> thin film when grown on the nanoPS layers, as discussed above.

The minority carrier diffusion coefficient can be calculated using the thickness of the interfaces ( $L$ ) and  $\tau$ , by means of the following relationship [36]:

$$D = \frac{L^2}{\tau} \quad (3)$$

Since the smallest values for  $\tau$  are obtained for the Al/Si+nanoPS+AgNPs/TiO<sub>2</sub>/NiCr Schottky devices,  $D$  will show the largest values. A higher diffusion coefficient indicates a larger average length for a carrier between generation and recombination [33]. These results are further confirmed by the improvement of the optoelectronic performance of the Al/Si+nanoPS+AgNPs/TiO<sub>2</sub>/NiCr devices, as demonstrated in a previous work [24].

Since the smallest values for  $\tau$  are obtained for the Al/Si+nanoPS+AgNPs/TiO<sub>2</sub>/NiCr Schottky devices,  $D$  will show the largest values. A higher diffusion coefficient indicates a larger average length for a carrier between generation and recombination [33]. These results are further confirmed by the improvement of the optoelectronic performance of the Al/Si+nanoPS+AgNPs/TiO<sub>2</sub>/NiCr devices, as demonstrated in a previous work [24].

The impedance of a parallel RC Schottky barrier is given by the following equation [37]:

$$Z = \frac{R \cdot X_c}{R + X_c} \quad (4)$$

where  $X_c$  is the capacitive reactance in Ohms,  $f$  is the frequency in Hertz, and  $C$  is the AC capacitance in Farads. From that, the capacitive reactance itself is inversely proportional to the applied frequency

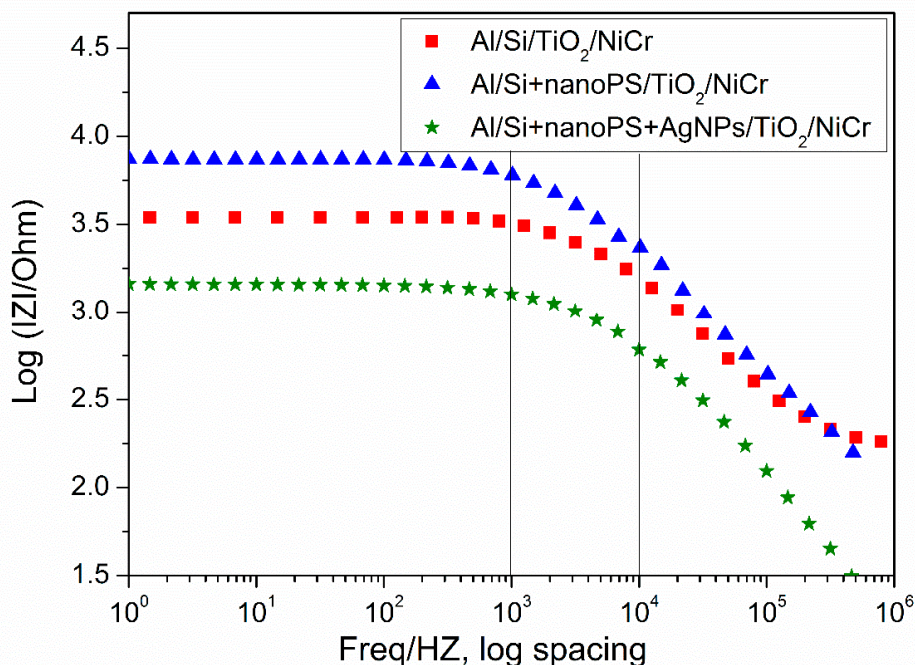


**Figure 5.** Bode diagram to study the effect of frequency on the total impedance for the three MIS Schottky barrier devices analyzed.

Mott–Schottky analysis allows determination of several parameters of semiconductors, such as the flat-band potential, carrier doping density, and the type of the semiconductor. Aiming at determining these parameters,  $C$ - $V$  measurements were recorded at the three specific frequencies where

**Figure 5.** Bode diagram to study the effect of frequency on the total impedance for the three MIS Schottky barrier devices analyzed. Energies 2020, 13, 2165

Mott-Schottky analysis allows determination of several parameters of semiconductors, such as the flat-band potential, carrier doping density, and the type of the semiconductor. Aiming at determining these parameters, C-V measurements were recorded at the three specific frequencies of 1, 5, and 10 kHz. From the experimental values, the Mott-Schottky plots shown in Figures 6–8 were generated for the three MIS Schottky barrier devices. The AC electrical parameters were calculated using the Mott-Schottky equation [38]:

$$\frac{1}{C^2} - \frac{1}{C_0^2} = \frac{2q}{\epsilon \epsilon_0 A N_D} \left( V - V_{fb} - \frac{K_B T}{q} \right) \quad (5)$$

where C (F) is the space charge capacitance, A (cm<sup>2</sup>) the active geometric area, N<sub>D</sub> (cm<sup>-3</sup>) the semiconductor doping density, ε the vacuum permittivity (8.854 × 10<sup>-12</sup> F·m<sup>-1</sup>), ε<sub>0</sub> the relative permittivity (19.8 for p-type silicon), V the applied potential, V<sub>fb</sub> the flat-band potential, at which there is no band bending or field inside the semiconductor [22], K<sub>B</sub> is the Boltzmann constant (1.381 × 10<sup>-23</sup> J·K<sup>-1</sup>), and T the absolute room temperature.

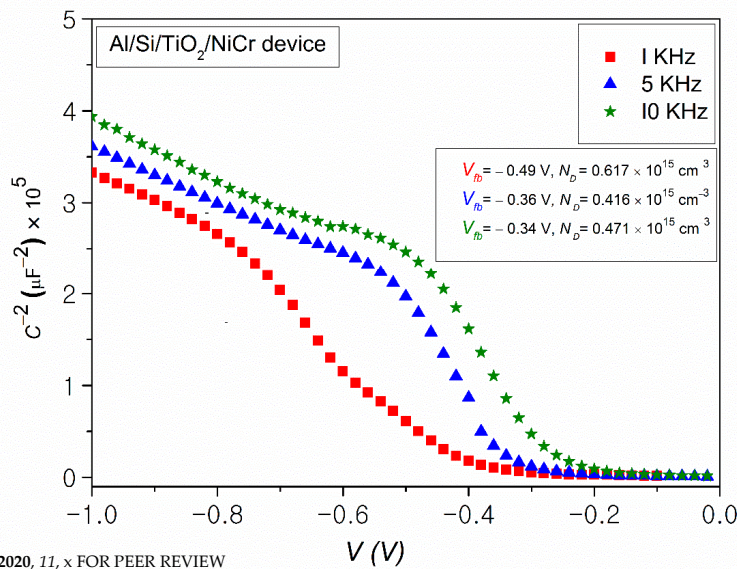


**Figure 6.** Mott-Schottky diagram for the Al/Si/TiO<sub>2</sub>/NiCr Schottky junction device at 1, 5, and 10 kHz. The values calculated for V<sub>fb</sub> and N<sub>D</sub> are presented in the inset.

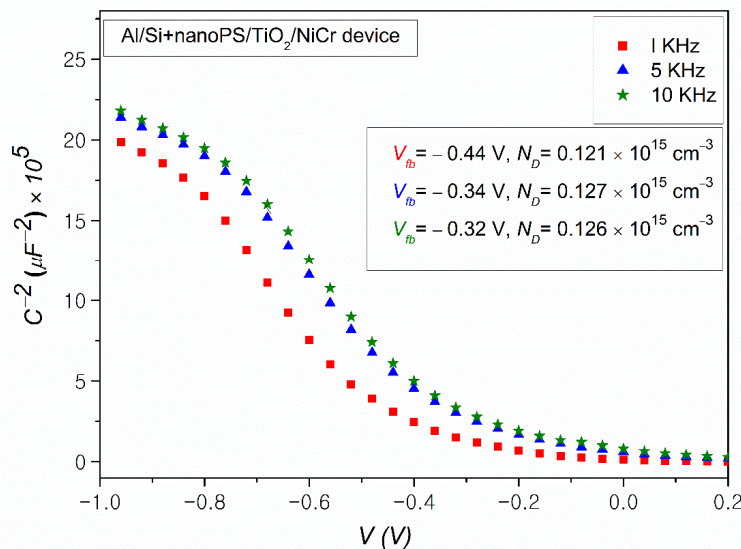
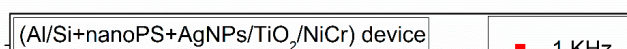


**Figure 7.** Mott-Schottky diagram for the Al/Si+nanoPS/TiO<sub>2</sub>/NiCr Schottky junction device, at 1, 5, and 10 kHz. The values calculated for V<sub>fb</sub> and N<sub>D</sub> are presented in the inset.



Energy

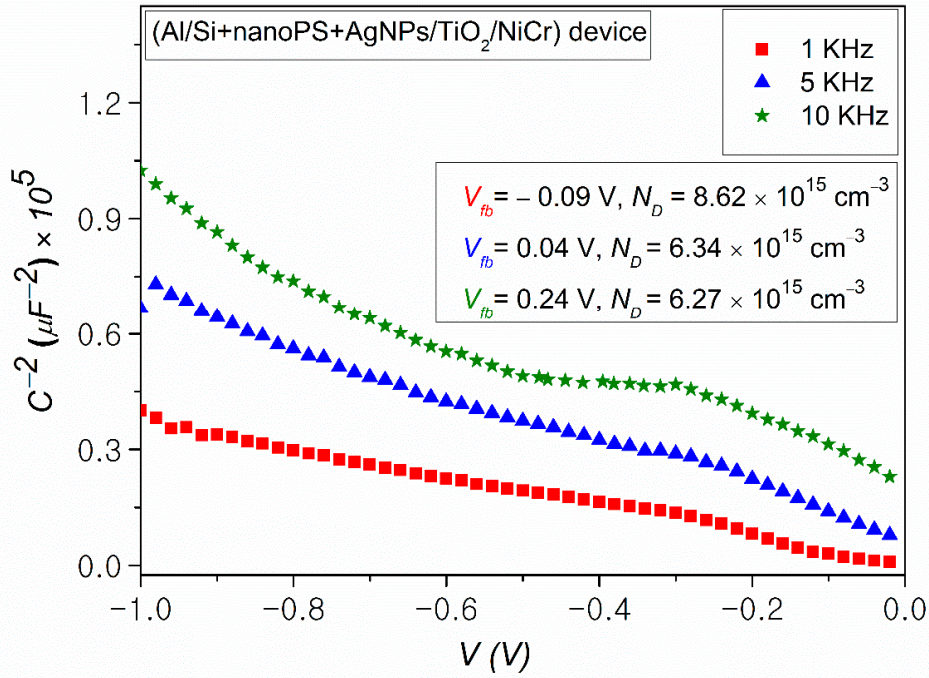


Figure 8. Mott-Schottky diagram for the Al/Si+nanoPS+AgNPs/TiO<sub>2</sub>/NiCr Schottky junction device, at 1, 5, and 10 kHz. The inset shows the values of  $V_{fb}$  and  $N_D$ .

The negative slope of the straight line from the three  $C^{-2}$ - $V$  plots confirms the p-type character of the electrical conductivity in all cases. According to Equation (5), the intercept of this straight line to the voltage axis gives the value of the flat-band potential, while the carrier concentration can be calculated from the value of the slope. The built-in potential ( $V_{bi}$ ) can be determined from the flat-band potential, according to the following equation [39]:

$$V_{bi} = V_{fb} - \frac{K_B T}{q} \quad (6)$$

All the Mott-Schottky diagrams confirm the decrease of capacitance with increasing frequency in the 1 KHz to 10 KHz range. Likewise, in all cases, the flat-band potential decreases with increasing frequency. Since all the MIS Schottky barrier devices have the same behavior with frequency, the results at 1 KHz are compared in Table 3. The values for  $V_{bi}$ , which opposes the flow of the carriers across the junction, slightly decreased in the case of the Al/Si+nanoPS/TiO<sub>2</sub>/NiCr devices, in comparison with the Al/Si/TiO<sub>2</sub>/NiCr devices. This reduction is attributed to the wider band gap of the nanoPS structures, compared to Si [28]. It is also observed that  $N_D$  decreased from  $0.617 \times 10^{15} \text{ cm}^{-3}$  for the Al/Si/TiO<sub>2</sub>/NiCr devices to  $0.121 \times 10^{15} \text{ cm}^{-3}$  for the Al/Si+nanoPS/TiO<sub>2</sub>/NiCr devices, probably due to the formation of a porous Si layer in the heavily-doped regions of the Si substrate [28]. For the Al/Si+nanoPS+AgNPs/TiO<sub>2</sub>/NiCr devices, a remarkable decrease in  $V_{bi}$  from 0.515 V for the Al/Si/TiO<sub>x</sub>/NiCr devices to 0.115 V for the Al/Si+nanoPS+AgNPs/TiO<sub>2</sub>/NiCr devices is observed. The notable decrease in  $V_{bi}$  for the Al/Si+nanoPS+AgNPs/TiO<sub>2</sub>/NiCr devices is probably due to the improvement of the electrical RC parameters, which is indicative of low  $\tau$  and large  $D$ , as determined from EIS measurements. An improvement in the electrical conduction has also been demonstrated through the values calculated for the carrier doping concentration, which were  $0.61 \times 10^{15} \text{ cm}^{-3}$  for the Al/Si/TiO<sub>2</sub>/NiCr devices, and notably increased to  $8.6 \times 10^{15} \text{ cm}^{-3}$  for the Al/Si+nanoPS+AgNPs/TiO<sub>2</sub>/NiCr devices.

**Table 3.** AC electrical parameters for the three structures determined from the Mott–Schottky plots at 1 KHz.

Device Structure	$V_{fb}$ (V)	$V_{bi}$ (V)	$N_D \times 10^{15}$ (cm <sup>-3</sup> )
Al/Si/TiO <sub>2</sub> /NiCr	-0.9	-0.515	0.617
Al/Si+ nanoPS/TiO <sub>2</sub> /NiCr	-0.44	-0.465	0.121
Al/Si+nanoPS+AgNPs/TiO <sub>2</sub> /NiCr	-0.09	-0.115	8.620

3.2.2. DC Electrical Measurements

Current-voltage ( $I$ - $V$ ) measurements of Schottky barrier devices can be used to determine some of their essential parameters, which allows for describing and optimizing their overall performance. This study is aimed at determining the reverse saturation current ( $I_0$ ), diode ideality factor ( $n$ ), parasitic series ( $R_s$ ) and shunt resistances ( $R_{sh}$ ), and barrier height ( $\phi_B$ ). Figure 9 portrays the experimental  $I$ - $V$  curves in the  $-1.5$  V to  $+1.5$  V range for the three Schottky barrier devices. The experimental results confirm the rectifying behavior for all the devices, which is consistent with a thermionic emission carrier transport mechanism, with a variation in the particular values of the re

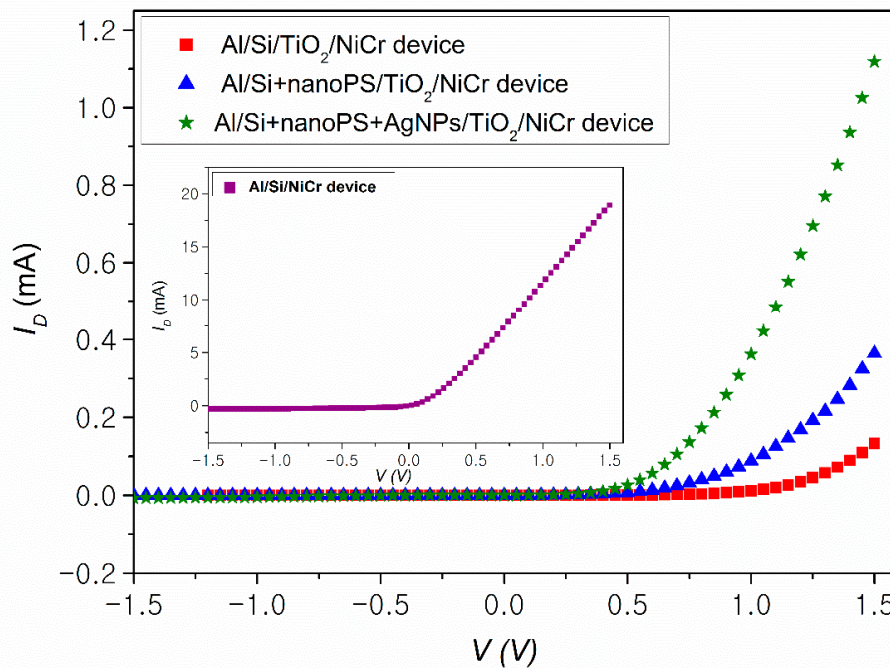


**Figure 9.** Current-voltage ( $I$ - $V$ ) curve for the three MIS Schottky junction devices under forward and reverse bias, showing in all cases a rectifying behavior. The inset portrays a typical  $I$ - $V$  curve for Al/Si/NiCr devices (metal–semiconductor diodes), showing a notable increment in the values of current.

An ideal diode has low resistance (ideally zero) under forward bias, and high resistance (ideally infinite) under reverse bias. The Schottky ideal diode equation is given by [40]:

$$I_D = I_0 \left[ \frac{e^{\frac{qV}{nK_B T}} - 1}{e^{\frac{qV_1}{nK_B T}} - 1} \right] \tag{7}$$

where  $I_D$  is the current in the dark,  $I_0$  is the reverse saturation current,  $n$  is the diode ideality factor (equal to one for a Si ideal diode and 2 for Ge),  $K_B$  is the Boltzmann constant, and  $T$  is the absolute junction temperature. The ideal diode equation assumes that all recombination processes occur via band-to-band transitions or through traps in the bulk of the device. However, recombination could occur in other areas of the device, leading to losses in the overall performance of the diode. As such, a modified equation widely used for non-ideal diodes is given by the expression [40]:

$$I_D = I_0 \left[ e^{\frac{q(V-IR_s)}{nK_B T}} - 1 \right] + \frac{V - IR_s}{R_{sh}} \tag{8}$$

Large values of  $R_s$  cause power to be dissipated in solar cells, while low  $R_{sh}$  leads to power losses

occur in other areas of the device, leading to losses in the overall performance of the diode. As such, a modified equation widely used for non-ideal diodes is given by the expression [40]:

$$I_D = I_0 \left[ e^{\frac{q(V-IR_s)}{nK_B T}} - 1 \right] + \frac{V - IR_s}{R_{sh}} \tag{8}$$

Large values of  $R_s$  cause power to be dissipated in solar cells, while low  $R_{sh}$  leads to power losses by providing an alternate current path for the light-generated current.

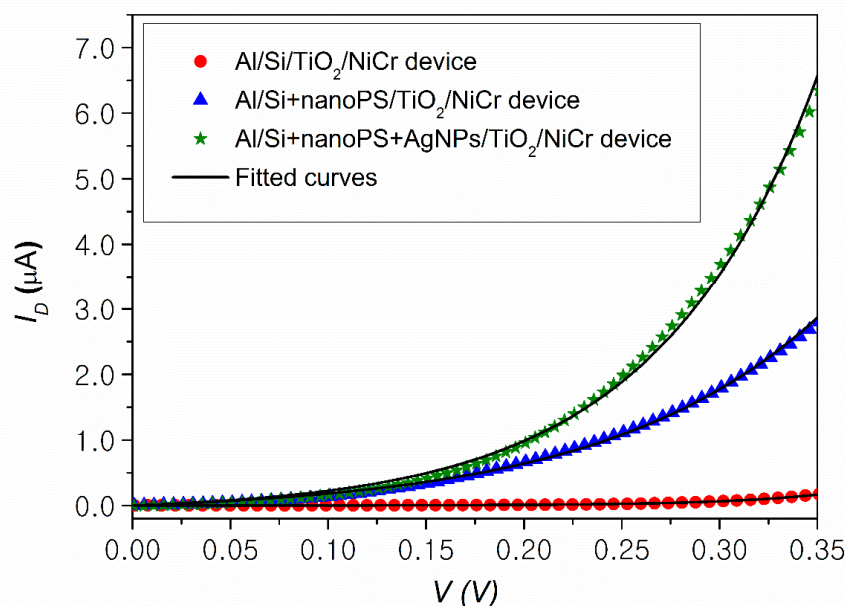
The Al/Si/TiO<sub>2</sub>/NiCr devices show the lowest values of  $I_D$ , probably as a consequence of coating the Si substrates with a compact and continuous interfacial thin film of TiO<sub>2</sub>, which acts as a very effective insulating thin film. To analyze the effect of the TiO<sub>2</sub> thin film on the reduction in the current through the device, the inset of Figure 9 shows the  $I$ - $V$  curve corresponding to the Al/Si/TiO<sub>2</sub>/NiCr devices without TiO<sub>2</sub> layer. The Al/Si+nanoPS/TiO<sub>2</sub>/NiCr devices show larger  $I_D$  values than those of the Al/Si/TiO<sub>2</sub>/NiCr devices. This effect, similar to the case of the series resistance determined from the Nyquist plots, is attributed to a much thinner TiO<sub>2</sub> layer covering the nanoPS layer than when TiO<sub>2</sub> is grown over flat Si, or even to the presence of small pits or pores. As pointed out before, this is probably a consequence of the filling of the pores of nanoPS with TiO<sub>2</sub> during the spin coating process. The combination of nanoPS with AgNPs remarkably improves the electrical conduction properties of the active layer, as previously confirmed by EIS and  $I$ - $V$  measurements.

Figure 10 shows the experimental  $I$ - $V$  results under forward bias (up to 0.35 V) and the corresponding fittings to Equation (8) (modified ideal diode). The very low values of  $I_D$  under reverse bias (of the order of 10<sup>-9</sup> A) indicate that  $R_{sh}$  is very high for the three MIS Schottky barrier diodes. Accordingly, the last part of Equation (8), which is related to  $R_{sh}$ , can be safely neglected for the fittings. Table 3 provides the DC electrical parameters obtained from the fittings, in addition to the barrier height ( $\phi_B$ ), which was calculated using the following equation [41]:

$$\phi_B = \frac{K_B T}{q} \ln \left( \frac{A A^* T^2}{I_0} \right) \tag{9}$$

where  $A$  (cm<sup>2</sup>) is the active area of the device and  $A^*$  is the effective Richardson constant, which takes the value 32 A/cm<sup>2</sup>K<sup>2</sup> for p-type Si.

where  $A$  (cm<sup>2</sup>) is the active area of the device, and  $A^*$  is the effective Richardson constant, which takes the value



**Figure 10.** Experimental  $I$ - $V$  data under forward bias and fittings to the modified ideal diode model used to extract the electrical parameters of the MIS Schottky barrier devices.

Table 4 presents a comparison between the DC electrical parameters, namely  $I_0$ ,  $n$ ,  $R_s$ , and  $\phi_B$  for the three MIS Schottky barrier devices. Since the values of  $I_D$  are rather small for the Al/Si/TiO<sub>2</sub>/NiCr devices compared with the other two Schottky barrier devices,  $I_0$  is very small. Likewise,  $n$  shows the lowest value in this case. The increase in  $n$  observed for the Al/Si+nanoPS/TiO<sub>2</sub>/NiCr devices is attributed to the higher porosity of the surface of Si after the etching process, which causes an increase in the defects on the surface of the nanoPS layers [25]. The reduction of the value of the ideality factor

Table 4 presents a comparison between the DC electrical parameters, namely  $I_0$ ,  $n$ ,  $R_s$ , and  $\varphi_B$  for the three MIS Schottky barrier devices. Since the values of  $I_D$  are rather small for the Al/Si/TiO<sub>2</sub>/NiCr devices compared with the other two Schottky barrier devices,  $I_0$  is very small. Likewise,  $n$  shows the lowest value in this case. The increase in  $n$  observed for the Al/Si+nanoPS/TiO<sub>2</sub>/NiCr devices is attributed to the higher porosity of the surface of Si after the etching process, which causes an increase in the defects on the surface of the nanoPS layers [35]. The reduction of the value of the ideality factor for the Al/Si+nanoPS+AgNPs/TiO<sub>2</sub>/NiCr devices ( $n = 3.29$ ) is considered a consequence of a change of the type of charge carrier recombination that is taking place in the active layer associated to the Ag nanoparticles embedded into nanoPS.

**Table 4.** DC electrical parameters obtained from the fitting of the experimental  $I$ - $V$  curves.

Device Structure	$I_0$ (mA)	$n$	$R_s$ (k $\Omega$ )	$\varphi_B$ (V)
Al/Si/TiO <sub>2</sub> /NiCr	$2.32 \times 10^{-7}$	2.12	3.21	0.87
Al/Si+nanoPS/TiO <sub>2</sub> /NiCr	$1.23 \times 10^{-4}$	4.39	0.363	0.72
Al/Si+nanoPS+AgNPs/TiO <sub>2</sub> /NiCr	$9.55 \times 10^{-5}$	3.29	0.139	0.73

The values of  $I_D$  are smaller for the Al/Si/TiO<sub>2</sub>/NiCr devices than those of the nanoPS-based devices. This reduction is attributed to the large thickness of the TiO<sub>2</sub> layer, so that  $I_0$  is very small ( $2.32 \times 10^{-7}$  mA). The presence of a porous layer on the Si substrate causes a decrease in the doping concentration, due to the formation of the pores in the heavily doped regions, as mentioned in the section devoted to EIS characterization. As a result, both  $I_0$  and  $n$  increase. The performance improves upon infiltration of AgNPs into nanoPS, with  $I_0$  decreasing from  $1.23 \times 10^{-4}$  mA for the Al/Si+nanoPS/TiO<sub>2</sub>/NiCr devices to  $9.55 \times 10^{-5}$  mA for the Al/Si+nanoPS+AgNPs/TiO<sub>2</sub>/NiCr devices. Additionally,  $\varphi_B$  for the Al/Si+nanoPS+AgNPs/TiO<sub>2</sub>/NiCr devices slightly increases due to the improvement in both  $I_0$  and  $n$ . Furthermore, the reduction in the value of  $R_s$  for the Al/Si+nanoPS+AgNPs/TiO<sub>2</sub>/NiCr devices is most likely due to an improved internal electrical conduction upon infiltration of metallic nanoparticles into the nanoPS layer. The large  $R_s$  value for the Al/Si/TiO<sub>2</sub>/NiCr devices is presumed to be due to the large thickness of the TiO<sub>2</sub> interfacial layers grown on the Si surface, which decrease the internal conductivity of the device.

#### 4. Conclusions

The main aim of this study was to study the electrical conduction properties of three different MIS Schottky barrier diodes, aiming at assessing their potential use as photovoltaic solar cells. With this objective in mind, the AC and DC electrical conduction properties of the MIS Schottky barrier diodes were studied and analyzed in detail.

The AC electrical properties were determined using a combination of electrochemical impedance spectroscopy and capacitance–voltage measurements. From the AC electrical characterization, an equivalent electric model was proposed. Additionally, Mott–Schottky analysis allowed determination of such parameters as the flat-band potential, carrier doping density, and the type of the conduction (p or n). The DC electrical properties were obtained from current–voltage measurements, which allowed us to determine several key diode parameters, namely reverse saturation current, ideality factor, parasitic series and shunt resistances, and barrier height.

In all, the electrical conduction properties of MIS Schottky barrier diodes with the structure Al/Si/TiO<sub>2</sub>/NiCr were improved by including two modifications to the initial design. Firstly, by etching the Si surface leading to nanoPS layers, which resulted in improving the electrical behavior of the TiO<sub>2</sub>/NiCr interface. However, the presence of nanoPS layers leads to conduction losses at the Si+nanoPS/TiO<sub>2</sub> interface. To overcome this drawback, silver nanoparticles were infiltrated into the nanoPS layers, which led to a notable enhancement in the overall electrical conduction properties of the resulting Al/Si+nanoPS+AgNPs/TiO<sub>2</sub>/NiCr MIS Schottky barrier diodes. The enhancement

observed in the electrical conduction and carrier separation for these devices was recently reported to also improve their optoelectronic performance, thus enabling their use in the field of photovoltaics.

**Author Contributions:** Conceptualization, R.R. and R.J.M.-P.; Methodology, R.R.; Validation, R.R. and R.J.M.-P.; Formal Analysis, R.R. and R.J.M.-P. Investigation, R.R. and R.J.M.-P.; Resources R.R. and R.J.M.-P.; Data Curation, R.R. and R.J.M.-P.; Writing-Original Draft Preparation, R.R.; Writing-Review & Editing, R.R. and R.J.M.-P.; Visualization, R.R. and R.J.M.-P.; Supervision, R.J.M.-P.; Project Administration, R.J.M.-P.; Funding Acquisition, R.J.M.-P. All authors have read and agreed to the published version of the manuscript.

**Funding:** This work was partially supported by the Egyptian Ministry of Higher Education, Missions Section under an Egyptian joint supervision grant at UAM Spain for PhD degree.

**Acknowledgments:** We would like to thank the Egyptian Institute, Cultural Office of the Egyptian Embassy in Madrid, Spain. The authors are thankful to Luis García Pelayo and Valentin Constantin Nistor for technical support.

**Conflicts of Interest:** The authors declare no conflict of interest.

## References

- Gautier, G.; Defforge, T.; Desplombain, S.; Billoué, J.; Capelle, M.; Povéda, P.; Vanga, K.; Lu, B.; Bardet, B.; Lascaud, J. Porous silicon in microelectronics: From academic studies to industry. *ECS Trans.* **2015**, *69*, 123–134. [[CrossRef](#)]
- Canham, L. *Handbook of Porous Silicon*; Springer: Berlin/Heidelberg, Germany, 2014.
- Martin-Palma, R.; Pérez-Rigueiro, J.; Martínez-Duart, J. Study of carrier transport in metal/porous silicon/Si structures. *J. Appl. Phys.* **1999**, *86*, 6911–6914. [[CrossRef](#)]
- Martín-Palma, R.; Pérez-Rigueiro, J.; Guerrero-Lemus, R.; Moreno, J.; Martínez-Duart, J. Ageing of aluminum electrical contacts to porous silicon. *J. Appl. Phys.* **1999**, *85*, 583–586. [[CrossRef](#)]
- Shetty, A.; Roul, B.; Mukundan, S.; Mohan, L.; Chandan, G.; Vinoy, K.; Krupanidhi, S. Temperature dependent electrical characterisation of Pt/HfO<sub>2</sub>/n-GaN metal-insulator-semiconductor (MIS) Schottky diodes. *AIP Adv.* **2015**, *5*, 097103. [[CrossRef](#)]
- Kim, H.; Kumar, M.D.; Kim, J. Highly-performing Ni/SiO<sub>2</sub>/Si MIS photodetector for NIR detecting applications. *Sens. Actuators A Phys.* **2015**, *233*, 290–294. [[CrossRef](#)]
- Digdaya, I.A.; Adhyaksa, G.W.; Trześniewski, B.J.; Garnett, E.C.; Smith, W.A. Interfacial engineering of metal-insulator-semiconductor junctions for efficient and stable photoelectrochemical water oxidation. *Nat. Commun.* **2017**, *8*, 15968. [[CrossRef](#)]
- Chang, T.-Y.; Chang, C.-L.; Lee, H.-Y.; Lee, P.-T. A metal-insulator-semiconductor solar cell with high open-circuit voltage using a stacking structure. *IEEE Electron Device Lett.* **2010**, *31*, 1419–1421. [[CrossRef](#)]
- Pulfrey, D.L. MIS solar cells: A review. *IEEE Trans. Electron Devices* **1978**, *25*, 1308–1317. [[CrossRef](#)]
- Fahrenbruch, A.; Bube, R. *Fundamentals of Solar Cells: Photovoltaic Solar Energy Conversion*; Elsevier: Amsterdam, The Netherlands, 2012.
- Fonash, S. *Solar Cell Device Physics*; Elsevier: Amsterdam, The Netherlands, 2012.
- Singh, R.; Green, M.; Rajkanan, K. Review of conductor-insulator-semiconductor (CIS) solar cells. *Sol. Cells* **1981**, *3*, 95–148. [[CrossRef](#)]
- Srivastava, A.; Arora, B.; Guha, S. Current-voltage characteristics of GaAs metal-insulator-semiconductor solar cells under illumination. *Sol. Cells* **1984**, *12*, 277–283. [[CrossRef](#)]
- Wang, F.; Fahrenbruch, A.; Bube, R. Properties of metal-semiconductor and metal-insulator-semiconductor junctions on CdTe single crystals. *J. Appl. Phys.* **1989**, *65*, 3552–3559. [[CrossRef](#)]
- Shewchun, J.; Burk, D.; Spitzer, M.B. MIS and SIS solar cells. *IEEE Trans. Electron Devices* **1980**, *27*, 705–716. [[CrossRef](#)]
- Sharma, B. *Metal-Semiconductor Schottky Barrier Junctions and Their Applications*; Springer Science & Business Media: Berlin/Heidelberg, Germany, 2013.
- Mora-Sero, I.; Garcia-Belmonte, G.; Boix, P.P.; Vazquez, M.A.; Bisquert, J. Impedance spectroscopy characterisation of highly efficient silicon solar cells under different light illumination intensities. *Energy Environ. Sci.* **2009**, *2*, 678–686. [[CrossRef](#)]
- Lee, G.W.; Kim, H.; Park, J.; Shim, J.-I.; Shin, D.-S. Investigation of luminance degradation in organic light-emitting diodes by impedance spectroscopy. *IEEE Photonics Technol. Lett.* **2018**, *30*, 1183–1185. [[CrossRef](#)]

19. Ramadan, R.; Kamal, H.; Hashem, H.; Abdel-Hady, K. Gelatin-based solid electrolyte releasing Li<sup>+</sup> for smart window applications. *Sol. Energy Mater. Sol. Cells* **2014**, *127*, 147–156. [[CrossRef](#)]
20. Ramadan, R.; Elshorbagy, M.; Kamal, H.; Hashem, H.; Abdelhady, K. Preparation and characterization of protonic solid electrolyte applied to a smart window device with high optical modulation. *Optik* **2017**, *135*, 85–97. [[CrossRef](#)]
21. Schönleber, M.; Uhlmann, C.; Braun, P.; Weber, A.; Ivers-Tiffée, E. A consistent derivation of the impedance of a lithium-ion battery electrode and its dependency on the state-of-charge. *Electrochim. Acta* **2017**, *243*, 250–259. [[CrossRef](#)]
22. Gelderman, K.; Lee, L.; Donne, S. Flat-band potential of a semiconductor: Using the Mott–Schottky equation. *J. Chem. Educ.* **2007**, *84*, 685. [[CrossRef](#)]
23. Kim, W.; Choi, W. A novel parameter extraction method for the one-diode solar cell model. *Sol. Energy* **2010**, *84*, 1008–1019. [[CrossRef](#)]
24. Ramadan, R.; Manso-Silvan, M.; Martın-Palma, R.J. Hybrid porous silicon/silver nanostructures for the development of enhanced photovoltaic devices. *J. Mater. Sci.* **2020**, *55*, 5458–5470. [[CrossRef](#)]
25. Martın-Palma, R.J.; McAtee, P.D.; Ramadan, R.; Lakhtakia, A. Hybrid Nanostructured porous silicon-silver Layers for Wideband optical Absorption. *Sci. Rep.* **2019**, *9*, 7291. [[CrossRef](#)] [[PubMed](#)]
26. Orazem, M.E.; Tribollet, B. *Electrochemical Impedance Spectroscopy*; John Wiley & Sons: Hoboken, NJ, USA, 2017.
27. Ribeiro, D.; Souza, C.; Abrantes, J. Use of Electrochemical Impedance Spectroscopy (EIS) to monitoring the corrosion of reinforced concrete. *Rev. Ibracon De Estrut. E Mater.* **2015**, *8*, 529–546. [[CrossRef](#)]
28. Kim, J.H.; Shin, D.H.; Lee, H.S.; Jang, C.W.; Kim, J.M.; Seo, S.W.; Kim, S.; Choi, S.-H. Enhancement of efficiency in graphene/porous silicon solar cells by co-doping graphene with gold nanoparticles and bis (trifluoromethanesulfonyl)-amide. *J. Mater. Chem. C* **2017**, *5*, 9005–9011. [[CrossRef](#)]
29. Chavarria, M.; Fonthal, F. Electrical Investigation of Porous Silicon/p-Si Heterojunction Prepared by Electrochemical Etching. *ECS J. Solid State Sci. Technol.* **2016**, *5*, P3172–P3175. [[CrossRef](#)]
30. Kulathuraan, K.; Mohanraj, K.; Natarajan, B. Structural, optical and electrical characterization of nanostructured porous silicon: Effect of current density. *Spectrochim. Acta Part A Mol. Biomol. Spectrosc.* **2016**, *152*, 51–57. [[CrossRef](#)]
31. Sultan, F.I.; Slman, A.A.; Nayef, U.M. IV and CV Characteristics of Porous Silicon Nanostructures by Electrochemical Etching. *Eng. Technol. J.* **2013**, *31*, 332–338.
32. Hamza, S.; Ignaszak, A.; Kiani, A. Synthesis of electrical conductive silica nanofiber/gold nanoparticle composite by laser pulses and sputtering technique. *Nanoscale Res. Lett.* **2017**, *12*, 432. [[CrossRef](#)]
33. Wang, D.; Zhu, J.; Ding, L.; Gao, P.; Pan, X.; Sheng, J.; Ye, J. Interface electric properties of Si/organic hybrid solar cells using impedance spectroscopy analysis. *Jpn. J. Appl. Phys.* **2016**, *55*, 056601. [[CrossRef](#)]
34. Youssef, G.; El-Nahass, M.; El-Zaiat, S.; Farag, M. Effect of porosity on the electrical and photoelectrical properties of textured n+ p silicon solar cells. *Mater. Sci. Semicond. Process.* **2015**, *39*, 457–466. [[CrossRef](#)]
35. Harizi, A.; Laatar, F.; Ezzaouia, H. Physical properties enhancement of porous silicon treated with In<sub>2</sub>O<sub>3</sub> as a antireflective coating. *Results Phys.* **2019**, *12*, 1716–1724. [[CrossRef](#)]
36. Fabregat-Santiago, F.; Garcia-Belmonte, G.; Mora-Sero, I.; Bisquert, J. Characterization of nanostructured hybrid and organic solar cells by impedance spectroscopy. *Phys. Chem. Chem. Phys.* **2011**, *13*, 9083–9118. [[CrossRef](#)] [[PubMed](#)]
37. Shibayama, N.; Zhang, Y.; Satake, T.; Sugiyama, M. Modelling of an equivalent circuit for Cu<sub>2</sub>ZnSnS<sub>4</sub>- and Cu<sub>2</sub>ZnSnSe<sub>4</sub>-based thin film solar cells. *RSC Adv.* **2017**, *7*, 25347–25352. [[CrossRef](#)]
38. Ma, Y.; Pendlebury, S.R.; Reynal, A.; Le Formal, F.; Durrant, J.R. Dynamics of photogenerated holes in undoped BiVO<sub>4</sub> photoanodes for solar water oxidation. *Chem. Sci.* **2014**, *5*, 2964–2973. [[CrossRef](#)]
39. Gupta, G.K.; Garg, A.; Dixit, A. Electrical and impedance spectroscopy analysis of sol-gel derived spin coated Cu<sub>2</sub>ZnSnS<sub>4</sub> solar cell. *J. Appl. Phys.* **2018**, *123*, 013101. [[CrossRef](#)]
40. Darwish, A.; El-Shazly, E.; Attia, A.; El-Rahman, K.A. Dark electrical properties and photovoltaic performance of organic/inorganic (SnPcCl<sub>2</sub>/p-Si) solar cells. *J. Mater. Sci. Mater. Electron.* **2016**, *27*, 8786–8792. [[CrossRef](#)]
41. Sze, S.M.; Ng, K.K. *Physics of Semiconductor Devices*; John Wiley & Sons: Hoboken, NJ, USA, 2006.





## Abbreviations in chapter 4

AC	Alternating current
DC	Direct current
MIS	metal-insulator-semiconductor
NanoPS	Nanostructured porous Silicon
AgNPs	Silver nanoparticles
MS	Metal–semiconductor
$V_{oc}$	Open-circuit voltage
EIS	Electrochemical impedance spectroscopy
$Ti[OCH(CH_3)_2]_4$	Titanium isopropoxide
R	Resistance
C	capacitor
CPE	Constant phase element
$R_s$	Series resistance
$\tau$	Minority carrier lifetime
D	Minority carrier diffusion coefficient
L	Thickness of the interfaces
$X_C$	Capacitive reactance
$f$	Frequency
A	The active geometric area
$N_D$	Semiconductor doping density
q	Electron charge ( $1.602 \times 10^{-19}$ C)
$\epsilon$	Relative permittivity
$\epsilon_0$	vacuum permittivity
$V_{fb}$	Flat-band potential
$K_B$	Boltzmann constant ( $1.381 \times 10^{-23}$ J·K <sup>-1</sup> )
$V_{bi}$	Built-in potential
$I_0$	Reverse saturation current
$R_{sh}$	Shunt resistance
$\phi_B$	Barrier height
$I_D$	The current in the dark
$A^*$	The effective Richardson constant

## **Chapter 5:**



### **Hybrid porous silicon/silver nanostructures for the development of enhanced photovoltaic devices**

Ramadan, M. Manso-Silván, R. J. Martín-Palma, *Journal of Materials Science*, 55(13), (2020), 5458-5470.

---



# Hybrid porous silicon/silver nanostructures for the development of enhanced photovoltaic devices

Rehab Ramadan<sup>1,2,\*</sup> , Miguel Manso-Silvan<sup>1,3</sup> , and Raul J. Martın-Palma<sup>1,3</sup> 

<sup>1</sup>Departamento de Fısica Aplicada, Universidad Autonoma de Madrid, Campus de Cantoblanco, 28049 Madrid, Spain

<sup>2</sup>Department of Physics, Faculty of Science, Minia University, Minia 61519, Egypt

<sup>3</sup>Instituto Universitario de Ciencia de Materiales "Nicolas Cabrera" (INC), Universidad Autonoma de Madrid, Campus de Cantoblanco, 28049 Madrid, Spain

Received: 22 October 2019

Accepted: 22 January 2020

Published online:

2 February 2020

© Springer Science+Business Media, LLC, part of Springer Nature 2020

## ABSTRACT

Si-based metal–insulator–semiconductor (MIS) Schottky junction solar cells with the basic structure Al/Si/TiO<sub>2</sub>/Au were fabricated. This structure was modified by the addition of nanostructured porous silicon (nanoPS) layers and silver nanoparticles (AgNPs), resulting in devices with the following structures: Al/Si/nanoPS/TiO<sub>2</sub>/Au and Al/Si/nanoPS+AgNPs/TiO<sub>2</sub>/Au. The key performance parameters of the three MIS Schottky junction solar cells were determined, including spectral photocurrent response, short-circuit current density, open-circuit voltage, fill factor, and efficiency. The experimental results show a remarkable enhancement in the overall performance of the solar cells upon the addition of nanoPS and AgNPs layers to the basic structure. An energy band model is proposed for the Si-based MIS Schottky junction solar cells to understand the different photogeneration and conduction mechanisms.

## Introduction

The unlimited availability of solar energy makes photovoltaic (PV) technology an inexpensive, renewable, clean, and reliable source of electricity generation for both space and terrestrial applications [1]. However, in spite of all the available alternatives and the intense research in this area, silicon is likely to remain the dominant PV material for the foreseeable future, given its abundance in the earth's crust, long-term stability, well-established technology (having its origins in the semiconductor industry),

and relatively low cost [2]. However, crystalline silicon (c-Si) still has several drawbacks which limit its performance. These include optical losses and high recombination rates, as well as thermal and quantum losses [3]. Many efforts have been made by researchers to reduce optical losses and carrier recombination rates. In particular, various nanostructures were grown on Si substrates, including Si nanowires [4–6], quantum dots [7], and porous silicon [8], as well as periodic, random, and pyramidal surface texturing [9, 10].

Address correspondence to E-mail: rehab.ramadan@predoc.uam.es

A different approach to achieve an efficient photovoltaic conversion of solar energy goes through the development of metal–semiconductor (MS) Schottky junction solar cells based on c-Si, basically because of their structural simplicity and therefore convenient realization [11]. Moreover, these solar cells are inexpensive compared to solar cells based on diffused p–n junctions and they also overcome the issues related to high-temperature diffusion. However, MS solar cells usually have lower conversion efficiencies compared to p–n junction solar cells of the same materials due to their typically low open-circuit voltage [12]. However, metal–insulator–semiconductor (MIS) junctions show increased open-circuit voltage due to tunneling through the insulating layer of the majority carriers or diffusion current due to the minority carriers [13, 14], thus improving the overall conversion efficiency of Schottky barrier solar cells.

In the present work, we present our findings related to the study of the optoelectronic performance of three different MIS Schottky junction solar cells. These include a device with the structure Al/Si/TiO<sub>2</sub>/Au and two modified devices. The first variation includes a nanoporous silicon (nanoPS) layer, leading to the structure Al/Si/nanoPS/TiO<sub>2</sub>/Au, while the second one includes silver nanoparticles (AgNPs) embedded into the nanoPS layer, leading to the structure Al/Si/nanoPS+AgNPs/TiO<sub>2</sub>/Au.

The modified devices constitute two strategies which are implemented to improve light absorption and minimize the carrier recombination rates of c-Si. In the first variation (Al/Si/nanoPS/TiO<sub>2</sub>/Au devices), nanoPS is used as a wideband optical absorber [15]. However, this choice has two main drawbacks: (a) The surface of nanoPS is rapidly oxidized upon exposition to the atmosphere, leading to changes in its optical properties [16], and (b) two main recombination mechanisms can take place on the surface of nanoPS, namely radiative recombination through surface states (surface recombination) and through oxygen vacancies [17]. In this line, thin layers of In<sub>2</sub>O<sub>3</sub> [16], SiO<sub>2</sub> or SiO<sub>2</sub>/SiN [18], TiO<sub>2</sub> [19], and Al<sub>2</sub>O<sub>3</sub> or Al<sub>2</sub>O<sub>3</sub>/SiN have been used to passivate the surface of nanoPS [20]. Thin layers with high resistivity or even insulating nature in contact with the active layer of solar cells limit the amount of current that can flow into a small localized area, thus lowering the carrier mobility which improves cell efficiency as a result of an increase in the open-circuit voltage [21]. In particular, the use of TiO<sub>2</sub> thin films has the great

advantage of serving at the same time as passivation layers to prevent nanoPS from oxidation and to increase the open-circuit voltage. At the same time, the TiO<sub>2</sub> thin films can be used as antireflective coatings [22].

In the second variation (Al/Si/nanoPS+AgNPs/TiO<sub>2</sub>/Au devices), plasmonic effects are used to increase light absorption and short-circuit current [23]. Furthermore, the immersion in noble metal ion solutions during the growth of metal nanoparticles is used to modify the surface properties of nanoPS [24–26]. Anyhow, although the use of plasmonic nanoparticles seems in principle attractive, it presents significant challenges. For instance, an excessive surface density of embedded nanoparticles in the active layer would increase carrier recombination rates and, as a result, decrease the overall solar cell efficiency [27].

The experimental results show a remarkable improvement in the photovoltaic performance of the Al/Si/nanoPS/TiO<sub>2</sub>/Au devices. Furthermore, a notable enhancement in the photocurrent response of the devices based on nanoPS layers combined with metallic AgNPs has been measured.

## Experimental

### Fabrication of the active nanoPS layers

NanoPS layers were fabricated by the electrochemical anodization of boron-doped (*p*-type) silicon wafers of <100> orientation, resistivity in the 25–30 Ω cm range, and surface roughness of the order of 0.1 nm. Al bottom contacts were deposited by electron beam evaporation. For the evaporation, the base pressure was  $1.25 \times 10^{-5}$  mbar and the evaporation time was 4 min, resulting in 150-nm-thick Al thin films. The Al thin films were subsequently annealed by rapid thermal processing (RTP) in nitrogen atmosphere for 5 min to turn the initial rectifying behavior into an ohmic one. Afterward, the wafers were cut into  $1.5 \times 1.5$  cm<sup>2</sup> pieces. Each piece was mounted in a sample holder with an area of about 1.23 cm<sup>2</sup> exposed to the etching solution (the active area of the solar cell device). The etching solution consists of a 1:6 HF (48 wt%)/dimethyl formamide (99 wt%) mixture. Before the etching process, the native oxide layer was removed by immersing the Si substrates into HF/H<sub>2</sub>O solutions (1:20 ratio) for 30 s. Next, the

substrates were cleaned by immersion in acetone and ethanol and then by distilled water to remove any residuals from the HF solution. The applied current density ranged between 5 and 15 mA/cm<sup>2</sup>, leading to layers with different porosities and different dimensions of the nanopores. The anodization time was fixed at 120 s. After the fabrication process, each sample was rinsed in ethanol and blown dry with dry nitrogen. The experimental setup of the anodization process was schematically described in a previous work [15].

### Infiltration of Ag NPs

The nanoPS layers were used as templates for the subsequent growth of silver nanoparticles. For this task, we used an electrochemical deposition process previously implemented [15] at a fixed current density of 1 μA/cm<sup>2</sup> and a fixed duration of 4 min (without optimization of the density of the infiltrated nanoparticles). The aqueous solution was composed of silver nitrate, sodium citrate, and nitric acid, with pH = 3. This process led to the formation of hybrid nanoPS/Ag NPs layers.

### Spin coating of TiO<sub>2</sub> thin films

A solution of titanium isopropoxide (Ti[OCH(CH<sub>3</sub>)<sub>2</sub>]<sub>4</sub>) in ethanol was prepared with a 0.4 M concentration. Next, 0.35 M concentration of HCl acid was added to the solution to induce an acid catalysis to prevent nanoPS from damage [28]. The solution was stirred at 3000 rpm at room temperature for 30 min to obtain a clear solution. Sixty microliters of the sol was cast on either the Si substrate, nanoPS layer, or the nanoPS+AgNPs hybrid layer at a spinning speed of 3000 rpm for 30 s. Finally, the resulting TiO<sub>2</sub> thin films were annealed on a hot plate at 150 °C for 5 min to evaporate the remaining solvents.

Furthermore, aiming at determining the energy band gap of TiO<sub>2</sub> thin films from optical absorption measurements, 60 μl of TiO<sub>2</sub> sol was cast on clean glass substrates at the same previous spinning speed and for the same time.

### Fabrication of Au micropatterned top contact by UV lithography

A negative photoresist (Ariston 20 series) was used for the lithographic process on the Au thin films as

previously described [29]. The Au thin films were deposited using a DC sputtering system in argon atmosphere. The typical deposition pressure was  $2 \times 10^{-2}$  mbar, and the typical plasma current was 20 mA, leading to a thickness of around 90 nm. The photoresist spin time was 30 s, and the spin speed was 4000 rpm. Afterward, the samples were dried on a hot plate at 70 °C for 15 min. The photoresist/Au film stack was then exposed to UV radiation (Hamamatsu LC-L1 UV-led spot light source,  $1 \text{ W} \times \text{cm}^{-2}$ ) through a printed photomask for 3 min. The photoresist micropattern was subsequently developed by immersing the sample in a 0.25 M NaOH solution for 1 min. Next, any residuals from the Au thin film were removed by wet etching, i.e., by immersing the sample in HCl/HNO<sub>3</sub> (1:3) solution for 1 min. The photoresist was finally lift off in acetone, and afterward, the device was cleaned using ethanol and distilled water and dried in nitrogen.

An illustration of the final structure of the different devices is presented in Fig. 1, including FESEM images of the active layer/TiO<sub>2</sub> interfaces, where the active layers are Si, Si/nanoPS, and Si/nanoPS+AgNPs, leading to devices with the following structures: Al/Si/TiO<sub>2</sub>/Au, Al/Si/nanoPS/TiO<sub>2</sub>/Au, and Al/Si/nanoPS+AgNPs/TiO<sub>2</sub>/Au, respectively, in addition to a real top-view image of the fabricated devices.

### Characterization techniques

The morphology of the thin films and interfaces was studied by field emission scanning electron microscopy (FESEM) using a Philips XL-40FEG microscope operated at 5 kV.

Optical characterization in the UV–visible range (250–900 nm) was carried out using a Jasco V-560 double-beam spectrophotometer, equipped with an integrating sphere to avoid scattering losses.

The electrical characterization of the MIS Schottky junction solar cells was carried out in a Bio-Logic SP-150 potentiostat with a scan rate 5 mV/s and applied potential in the + 1.5 to – 1.5 V range. A homemade cell consisting of two movable copper probes with a diameter of 0.5 mm and a copper base ( $2 \times 2 \text{ cm}^2$ ) was used. The measurements were carried out in a Faraday box to shield them from any external signals.

A solar simulator (LCS-100 Solar Simulator-Model 94011A), with a calibrated illumination power

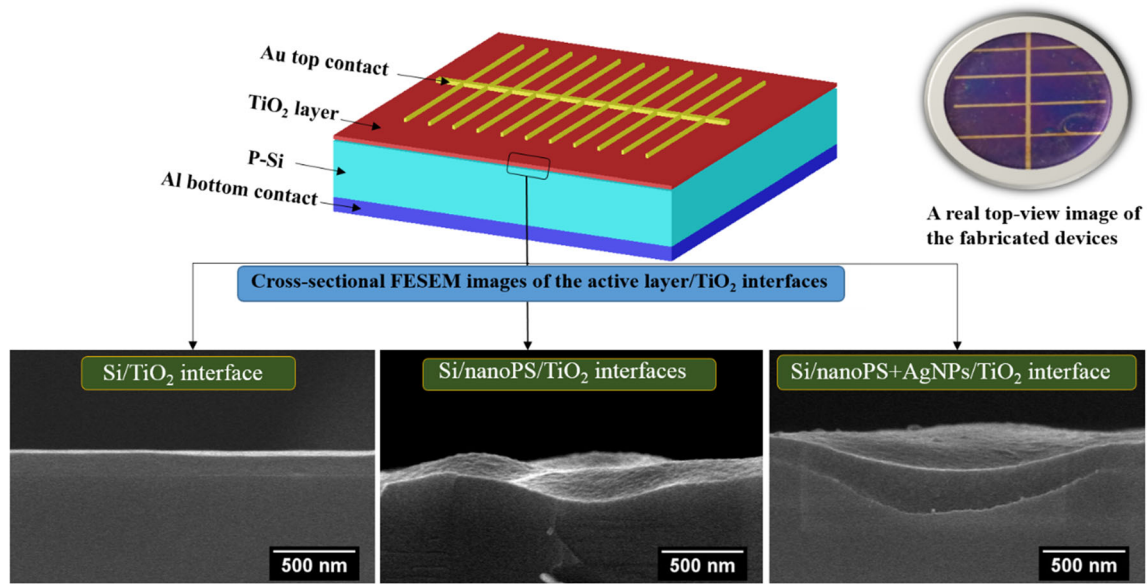


**Figure 1** Schematic illustration of the structure of the Schottky junction solar cell devices fabricated for this study, with FESEM cross-sectional images of the active layer/TiO<sub>2</sub> interfaces for the three devices. In addition to a real top-view image of the fabricated devices.

density of 100 mW/cm<sup>2</sup>, was used as the light source to measure the photovoltaic characteristics of the fabricated MIS Schottky solar cells.

Photocurrent measurements were carried out at 0 V bias using a dual digital lock-in amplifier (Signal Recovery 7225) at a chopper frequency of 300 Hz. Illumination was provided by an Acton Research Corporation Tungsten–Deuterium dual light source (model TDS-429), and a SpectraPro 150 monochromator equipped with three interchangeable diffraction gratings (1200 lines/mm) was used to select the wavelength.

## Experimental results

### Morphology

The FESEM images portrayed in Fig. 2 show the different layers which compose the final devices. More specifically, Fig. 2a, b shows the microstructure of the nanoPS layers and demonstrates the presence of AgNPs inside its pores and on the surface. Besides, it is observed that the nanoPS layers comprise macropores, with typical diameters in the 500–600 nm range, combined with meso-pores with diameters in the 5–30 nm range. Furthermore, the diameter of the AgNPs typically ranges between 5 and 15 nm. A cross-sectional view of the Si/nanoPS+AgNPs/TiO<sub>2</sub>

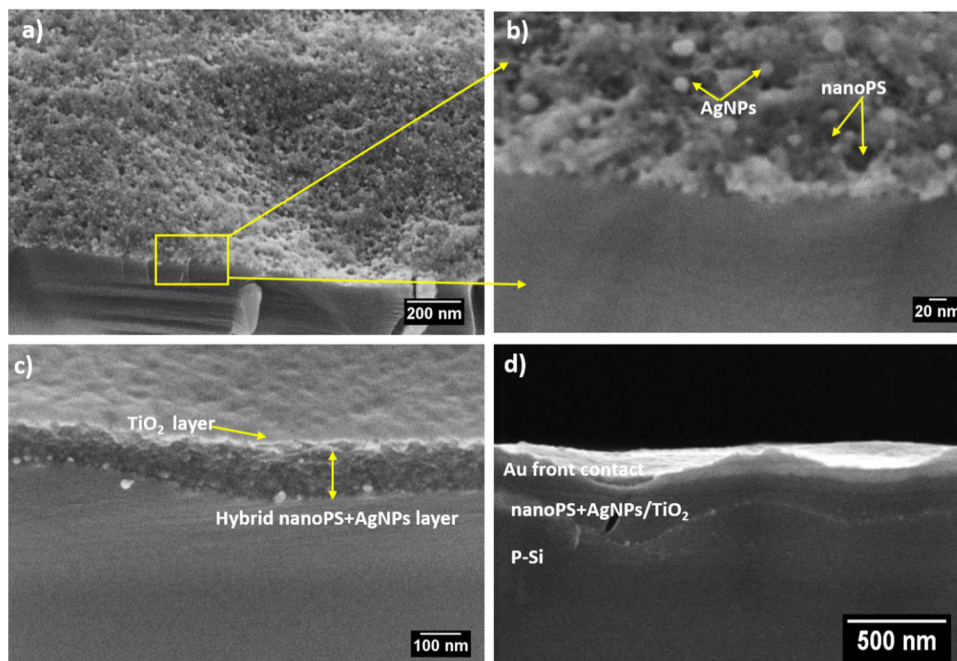
interface is depicted in Fig. 2c, from which the thickness of the nanoPS layer was determined to be around 120 nm. Spin coating of TiO<sub>2</sub> sol-gel leads to the filling of the nanopores with the sol and the formation of very thin films (~ 10 nm) over the nanoPS layers, as shown in Fig. 2c. The wavy shape of the top surface of the devices, portrayed in Fig. 2d, confirms the extremely low thickness of the TiO<sub>2</sub> interfacial thin film, which grows conformably following the underlying structure of the nanoPS layer. Likewise, the top Au metallic contact, with a thickness around 90 nm, follows the wavy surface shape of the TiO<sub>2</sub> thin film, as presented in Fig. 2d.

### Optical properties

#### Reflectance spectra

NanoPS may be described as a homogeneous mixture of silicon nanocrystallites, amorphous silicon, and air (pores), with typical feature sizes well below the wavelength of infrared and visible light [30, 31]. Thus, in this wavelength range, the optical properties of nanoPS will mainly depend on the composition of this mixture [32]. In this section, we analyze the effect of porosity on the overall reflectance (*R*) spectra of the nanoPS layers grown onto Si. Figure 3 shows the reflectance spectra of Si and of three different nanoPS layers grown onto the Si substrate. From the

**Figure 2** **a** Top-view FESEM images of a typical hybrid nanoPS+AgNPs layer, **b** high magnification image of a hybrid nanoPS+AgNPs layer. **c** Cross-sectional view showing a TiO<sub>2</sub> thin film grown onto the nanoPS+AgNPs layer. **d** Cross-sectional image of the Si/nanoPS+AgNPs/TiO<sub>2</sub>/Au structure.



experimental results, it is evident that the growth of nanoPS layers onto Si results in a significant reduction in the average reflectance. It is particularly remarkable that the average reflectance in the 250–900 nm wavelength range decreases from 35 to 19% for anodization current densities increasing from 5 to 15 mA/cm<sup>2</sup>. (The average reflectance for the Si substrate is 41%.) In particular, a drastic reduction of *R* for wavelengths shorter than 400 nm is clearly observed. As pointed out before, this effect has its

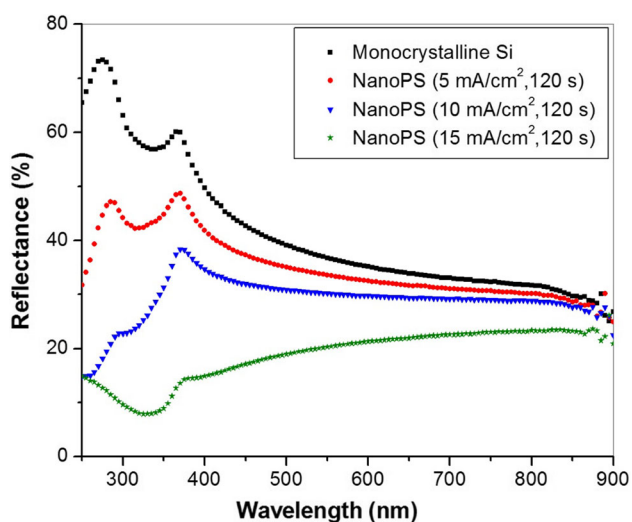


**Figure 3** Overall reflectance spectra of bulk Si and nanoPS layers grown onto Si substrates under different etching current densities (5, 10, and 15 mA/cm<sup>2</sup>) and at a fixed anodization time (120 s).

origin in a reduction in the effective index of refraction of the nanoPS layers with increasing porosity, i.e., increasing anodization current density. At the same time, increased porosity and reduced crystallite size result in increased transparency.

The experimental results allowed us to select an anodization current density of 10 mA/cm<sup>2</sup> as the best compromise between reflectance reduction and electrical conductivity (studied in a previous work) [33] for the subsequent fabrication of the photovoltaic devices. This particular current density leads to nanoPS layers with a porosity of 60.3% and quite low values of average reflectance (29% in the 250–900 nm wavelength range). Furthermore, a relatively small decrease in the electrical conductivity was determined from AC and DC electrical characterization [33].

Figure 4 shows the reflectance spectra of the Si substrate and the following layers grown onto Si: nanoPS, nanoPS+AgNPs, TiO<sub>2</sub>/nanoPS, and TiO<sub>2</sub>/nanoPS+AgNPs. It is clearly observed that the infiltration of silver nanoparticles into the nanoPS layers resulted in increased reflectance, especially in the UV–visible region. It is well known that the presence of noble metal nanoparticles leads to the generation of surface plasmon resonances (SPRs) which would reduce or shift the transmittance and/or reflectance spectra [34]. As such, metal NPs usually enhance the efficiency of photovoltaic devices by reducing

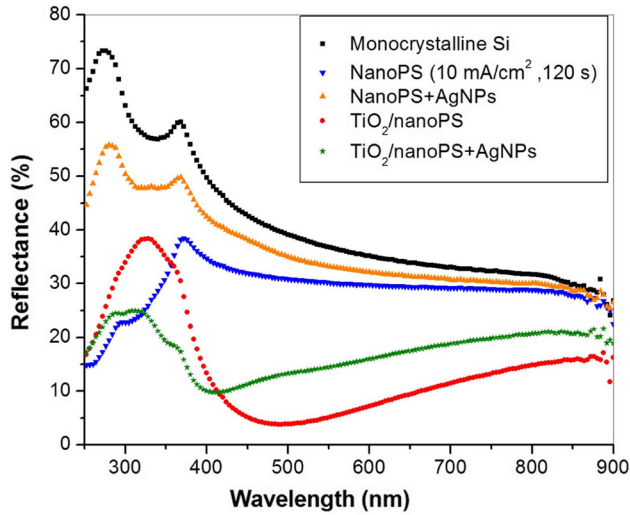


**Figure 4** Overall reflectance spectra of bulk Si, nanoPS layers grown at 10 mA/cm<sup>2</sup> for 120 s, nanoPS+AgNPs layers (infiltrated at 1 μA/cm<sup>2</sup> for 4 min), TiO<sub>2</sub>/nanoPS layers, and TiO<sub>2</sub>/nanoPS+AgNPs layers. All the structures were grown onto Si substrates.

reflection and increasing light trapping within the device. However, the specific optical behavior depends on the density of NPs, as well as their shape and size [35]. In some cases, the presence of metal NPs results in high reflectivity due to the backscattering of the NPs itself, or due to a large surface density of nanoparticles, which can reach their percolation threshold and even form a quasi-continuous thin film [36, 37]. Nevertheless, a large surface density of nanoparticles would result in improved electrical conduction. As such, aiming at reducing the reflectance produced by the metal NPs without decreasing their density, which has a favorable effect on the electrical conduction, very thin layers of TiO<sub>2</sub> (~ 10 nm) were deposited over the hybrid nanoPS AgNPs layers. TiO<sub>2</sub> was used given its low optical absorption in the visible [38].

The experimental results, portrayed in Fig. 4, confirm that depositing thin films of TiO<sub>2</sub> onto both nanoPS and nanoPS+AgNPs layers has a notable effect in reducing *R*. As such, the average reflectance in the 250–900 nm wavelength interval decreased from 29 to 14% upon deposition of TiO<sub>2</sub> thin films on the nanoPS layer and from 35 to 16% on the nanoPS+AgNPs hybrid layers.

Focusing on the average *R* of the devices with the structures Al/Si/nanoPS/TiO<sub>2</sub>/Au and Al/Si/nanoPS+AgNPs/TiO<sub>2</sub>/Au, a slight increment (from 14 to 16%) was observed upon the growth of silver NPs.

However, the addition of metallic AgNPs to the nanoPS layers results in a notable reduction in the average reflectance (from 23.8 to 17.5%) in the blue region of the optical spectrum ( $\lambda = 250\text{--}450\text{ nm}$ ). Thereby, we claim that SPR effects occur in this region which are attributed to the small size of the AgNPs (between 5 and 15 nm) [39].

*Determination of the band gap of the TiO<sub>2</sub> thin films*

In addition to reducing reflectance, the TiO<sub>2</sub> thin films in the MIS Schottky junction solar cells serve as interfacial layers. Accordingly, determining their energy band gap (*E<sub>g</sub>*) is a key step to create an energy band diagram for the devices. This would also allow us to analyze the electrical conduction mechanisms.

The optical band gap of the TiO<sub>2</sub> thin films can be determined from Tauc plots [40]. First, the spectral behavior of the absorption coefficient ( $\alpha$ ) was calculated from the optical measurement; afterward, the relationship between  $(\alpha \cdot d)^2$  and the photon energy was plotted (Fig. 5), where *d* is the thickness of the TiO<sub>2</sub> thin films. By assuming that the TiO<sub>2</sub> thin films show a direct band gap character [41], its band gap can be calculated by extrapolating the straight line of the relationship between  $(\alpha \cdot d)^2$  and the photon energy (*hν*), as shown in Fig. 5. The value of *E<sub>g</sub>* for the TiO<sub>2</sub> thin films was found to be 3.82 eV. This value is in good agreement with previous results obtained for TiO<sub>2</sub> thin films prepared by the sol gel method [41] and by sputtering [42].

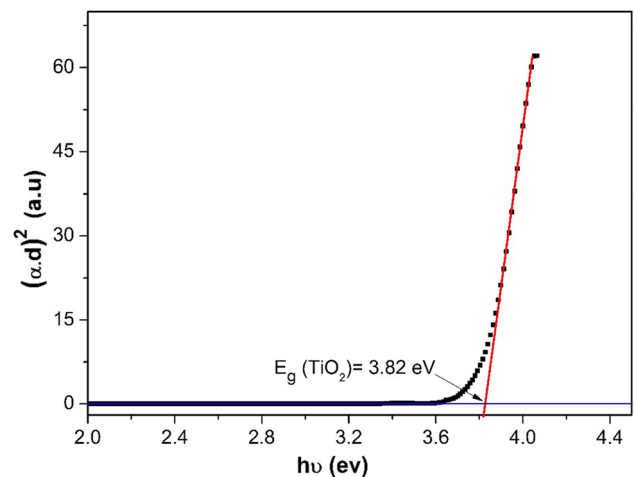


**Figure 5** Tauc plot for TiO<sub>2</sub> thin film deposited on a glass substrate to determine its *E<sub>g</sub>* value.



## Energy band diagrams

Energy band diagrams allow understanding the electronic and optoelectronic behavior of Schottky junctions. Figure 6 shows the energy band diagrams that we propose for the three different MIS Schottky junction devices under study. In all cases, the TiO<sub>2</sub> thin films, given their small thickness, behave as tunneling interfacial regions between the active layer and the front Au contact [43]. Although there are different forms of TiO<sub>2</sub>, all of them are semiconductors with empty and filled band edges at  $\sim 4.0$  eV and 7.9 eV below the vacuum level, as shown in

Fig. 6 [43]. The electron affinity at the surface of Si (100) is about 4.05 eV, and the valence band edge is located at around 5.17 eV below the vacuum level [43]. Anyhow, it is important to keep in mind that these values would slightly change due to the particular processes and techniques used for the fabrication of the different layers.

Accordingly, in the case of the Al/Si/TiO<sub>2</sub>/Au structures (Fig. 6a), the interface between Si and TiO<sub>2</sub> is expected to have a large valence band barrier ( $\Delta E_v \sim 2.5$  eV), which would block the transportation of holes from Si to TiO<sub>2</sub> and would only allow the transportation of minority carriers (electrons) to

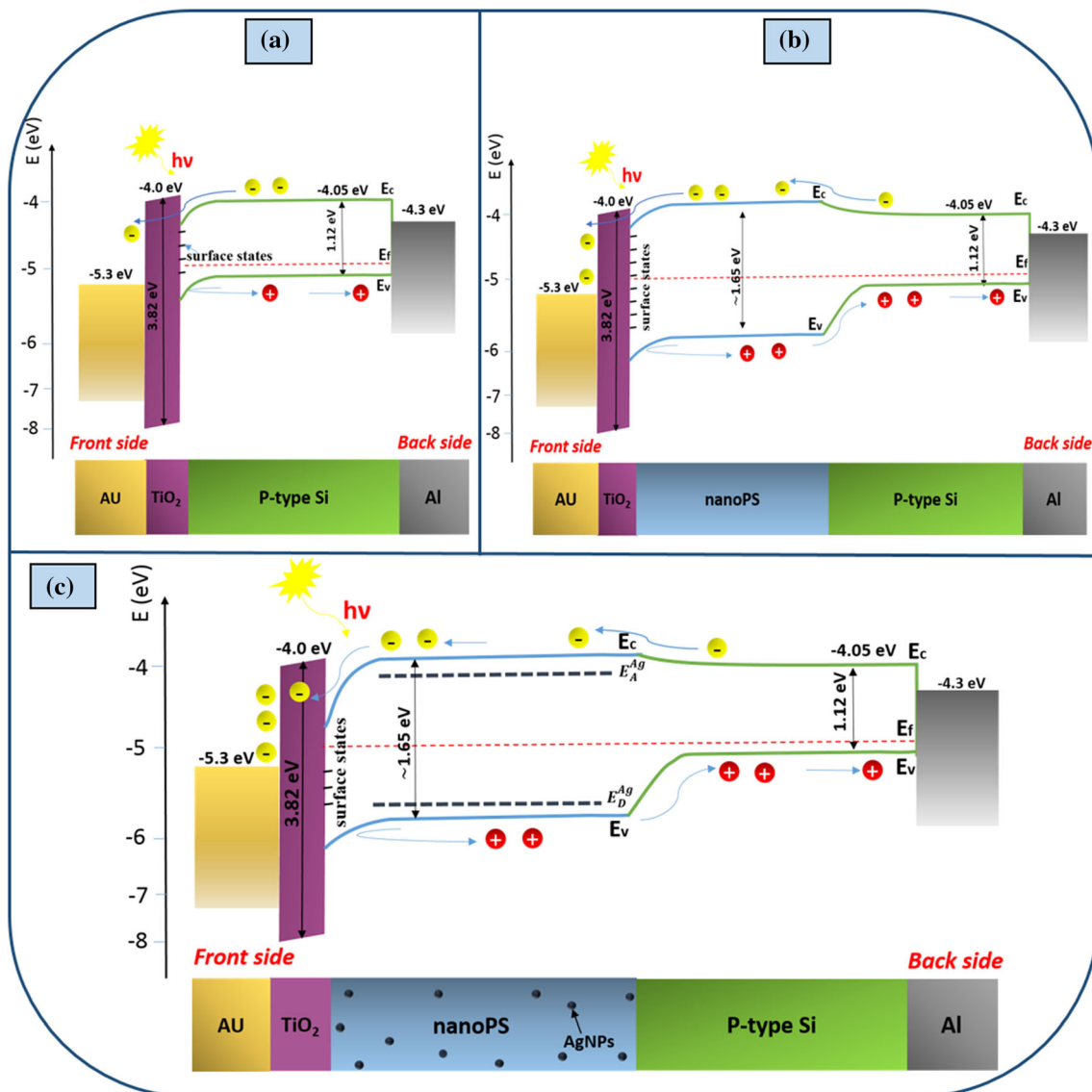


**Figure 6** Illustration of the proposed energy band diagrams for the different Si-based Schottky solar cells, namely **a** Al/Si/TiO<sub>2</sub>/Au devices, **b** Al/Si/nanoPS/TiO<sub>2</sub>/Au devices, and **c** Al/Si/nanoPS+AgNPs/TiO<sub>2</sub>/Au devices, with indication of surface states.

the Au contact, where the electron conductivity must be large and the hole conductivity must be low. Majority carriers (holes) move to the rear contact of the solar cell to increase the hole conductivity, where the hole conductivity is large and the electron conductivity is low (Al contact). In all, the valence band offset ( $\Delta E_v$ ) between Si and the TiO<sub>2</sub> thin film allows using the TiO<sub>2</sub> interlayer at the same time for electron harvesting and hole blocking to the Au contact. As a result, surface recombination is minimized, while the open-circuit voltage increases [43]. Regarding the interfacial layer in the MIS Schottky junctions, a very thin film is the best option to avoid increasing the series resistance of the device. That would lead to a decrease in the fill factor and the overall efficiency of the solar cells [12] in the case of the Al/Si/TiO<sub>2</sub>/Au structures (Fig. 1). The main reasons for photoreponse reduction for this device are discussed in detail in “Photocurrent response characterization” section.

Figure 6b shows the proposed energy band diagram corresponding to MIS Schottky devices with the structure Al/Si/nanoPS/TiO<sub>2</sub>/Au. The Fermi level for nanoPS is located close to the middle of the energy gap [44, 45] as a consequence of the formation of pores at defects and dopant sites of Si [16, 44, 46], thereby considerably reducing the doping concentration of Si and widening the energy gap of PS with respect to that Si (its energy band gap is 1.12 eV) [47]. We estimate the energy band gap value of nanoPS to be around 1.65 eV, corresponding to a porosity of 60.3% [47, 48]. Deposition of TiO<sub>2</sub> on the nanoPS layers has the important effect of reducing the rate of the different recombination mechanisms. Two primary competing recombination mechanisms are possible after the fabrication of nanoPS on Si, namely radiative recombination through the surface states (surface recombination) and radiative recombination through the oxygen vacancies [17]. This way, passivating the surface of nanoPS leads to an enhancement of the generation of electron/hole pairs by reducing the surface recombination rates. However, as previously shown (see “Morphology” section), nanoPS comprises pores of dimensions at two very different scales, i.e., macro- and meso-pores. Coating nanoPS with TiO<sub>2</sub> results in an effective coverage of the macro-pores with the sol. However, the meso-pores may still have oxygen vacancies, given their small dimensions with typical diameters in the 5–30 nm range (see FESEM images in Fig. 2). Accordingly,

radiative recombination processes through the oxygen vacancies in the meso-pores may still take place. For this reason, in addition to using TiO<sub>2</sub> thin films, chemical interaction with noble metal ions during the growth of the silver NPs has been used to further passivate the surface of nanoPS.

Figure 6c shows the proposed energy band diagram after growing AgNPs into the nanoPS layers. Given the small size and low surface density of the silver nanoparticles and based on previous experiments with Ag-doped Si [49], we hypothesize that the presence of the AgNPs leads to donor and acceptor levels in the forbidden region of nanoPS. According to this assumption, the addition of silver to the porous layers results in a singly ionized donor level in the lower half of the forbidden band of nanoPS ( $E_D^{Ag}$ ) and an acceptor level in the upper half of the forbidden band of nanoPS ( $E_A^{Ag}$ ). These ionized levels might lead to increased generation of electron–hole pairs by capture and emission of carriers in the nanoPS+AgNPs layer.

In the case of the Al/Si/nanoPS+AgNPs/TiO<sub>2</sub>/Au structures, we claim that the optoelectronic enhancement is due to four mechanisms. (1) Increased light absorption by the nanoPS layers in addition to TiO<sub>2</sub> thin films acting as antireflective coatings and passivating layers. (2) Improved surface passivation during the infiltration of the Ag NPs. (3) SPR effects at the interface between the metallic AgNPs and the TiO<sub>2</sub> and nanoPS layers manifested in the blue region of the electromagnetic spectrum (Fig. 4). Moreover, the generation of electron/hole pairs is greatly enhanced due to the electrical enhancement in the active layer by the AgNPs. (4) Improved electrical conduction given by the presence of silver nanoparticles.

## Photovoltaic properties

### Photocurrent response characterization

Figure 7 shows the photocurrent response in the 300–1200 nm wavelength range for the three MIS Schottky junction devices studied in this work. The experimental results show that the photocurrent presents a remarkable increase over all the wavelength range due to the incorporation of nanoPS layers, TiO<sub>2</sub> dielectric thin films, and the infiltration of silver nanoparticles into the porous structure. First, for the Al/Si/TiO<sub>2</sub>/Au MIS Schottky junction solar

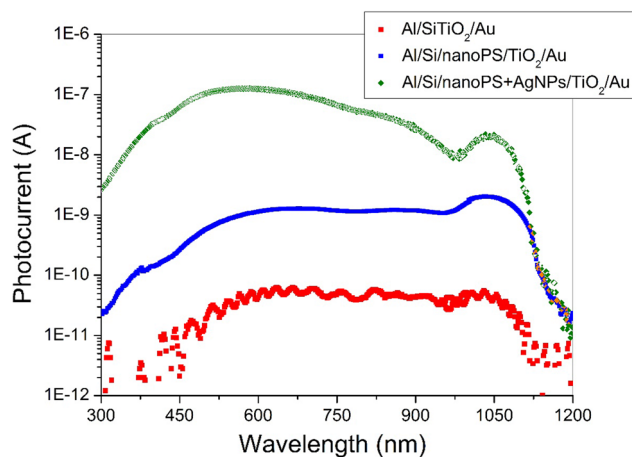


**Figure 7** Spectral photocurrent response in the 300–1200 nm wavelength range for the three MIS Schottky junction devices studied in this work.

cells, the photocurrent is very small, with values in the range of  $10^{-11}$  A. The small photocurrent levels for this device are attributed to three main reasons, namely (1) the indirect band gap character of Si, which causes an increase in the carrier recombination rates [3, 50], (2) a thicker  $\text{TiO}_2$  thin film than in the other devices, because flat Si accepts more  $\text{TiO}_2$  sol during spin casting due to surface tension and fluidics, as previously presented in Fig. 1, and (3) large reflectance losses at the Si surface, especially at lower wavelengths. The photovoltaic performance of the device was improved by growing nanoPS layers, which led to a radical decrease in the average reflectance from 41% (Si substrate) to 29% for the nanoPS/Si structure (see “Reflectance spectra” section). However, texturing the surface of Si causes an increase number of defects on the surface, leading to increased recombination rates in addition to conduction losses [51]. However, the infiltration of Ag nanoparticles inside the nanoPS layers results in a drastic enhancement in the photocurrent response by three orders of magnitude.

Three main reasons might be behind this remarkable improvement. (1) The resonant oscillation of conduction electrons (SPR) is in the blue region of the electromagnetic spectrum. The SPR effect is stimulated by the incident light at the interface between the metallic nanoparticles (AgNPs) and the dielectric films ( $\text{TiO}_2$  thin layers), which have negative and positive permittivity. The intensity of the resonances is determined by the dielectric properties of the metal and the surrounding medium and by the particle size

and shape [39]. The large enhancement in the near UV–blue region is attributed to the small size of the AgNPs (diameters in the 5–15 nm range), leading to higher absorption (Fig. 4) and generation of electron/hole pairs. (2) Surface passivation of nanoPS is improved during the growth of the AgNPs by reducing the radiative recombination induced by oxygen vacancies in the meso-pores. (3) The electrical conduction of nanoPS is highly improved by the presence of the metallic nanoparticles, as previously discussed for Au NPs [2]. From our recent study on the AC and DC electrical properties of these structures, a large enhancement in the diffusion length of the minority carriers was found, which led to improving carrier separation and generation of electron/hole pairs [33].

#### *Current–voltage characterization under illumination*

The current density–voltage ( $J$ – $V$ ) characteristics of the three MIS Schottky junction solar cells under illumination ( $100 \text{ mW/cm}^2$ ) were measured. The experimental results are shown in Fig. 8. The different electrical parameters which characterize the performance of solar cells, i.e., open-circuit voltage ( $V_{oc}$ ), short-circuit current density ( $J_{sc}$ ), fill factor (FF), and conversion efficiency ( $\eta$ ), were determined from the experimental  $J$ – $V$  curves and are presented in Table 1. A remarkable enhancement of both  $V_{oc}$  and  $J_{sc}$  for the Al/Si/nanoPS/ $\text{TiO}_2$ /Au Schottky barrier devices when compared to the Al/Si/ $\text{TiO}_2$ /Au devices is observed, most likely due to reduced reflectance losses provided by the porous structure. Also, filling the nanopores with the  $\text{TiO}_2$  sol led to decreasing its thickness, making these thin films more suitable as interfacial layers for the MIS solar cells. It is also noticeable that electron/hole pair generation is drastically improved by the infiltration of AgNPs into the nanoPS layers, probably due to the combined action of SPR effects, the reduction in  $R$ , and increased conduction, as discussed in “Photocurrent response characterization” section. As a result, the conversion efficiency ( $\eta$ ) increased from 0.9% for the Al/Si/nanoPS/ $\text{TiO}_2$ /Au devices to 1.9% for the Al/Si/nanoPS+AgNPs/ $\text{TiO}_2$ /Au structures (Table 1).

Figure 9 shows the maximum power density values for the three devices, which allows to calculate the fill factor (FF) and efficiency ( $\eta$ ) from the following well-known relations [12, 52]:

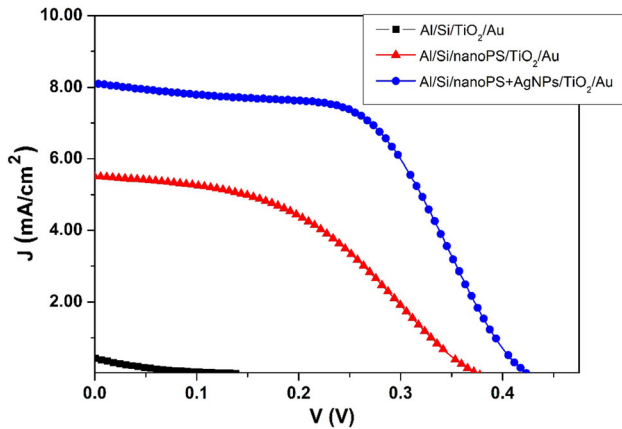


**Figure 8**  $J$ - $V$  characteristic of Al/Si/TiO<sub>2</sub>/Au, Al/Si/nanoPS/TiO<sub>2</sub>/Au and Al/Si/nanoPS+AgNPs/TiO<sub>2</sub>/Au photovoltaic devices.

$$FF = \frac{I_m V_m}{I_{sc} V_{oc}} \tag{1}$$

$$\eta = \frac{P_{out}}{S \cdot P_{in}} = \frac{I_m V_E}{S \cdot P_{in}} \tag{2}$$

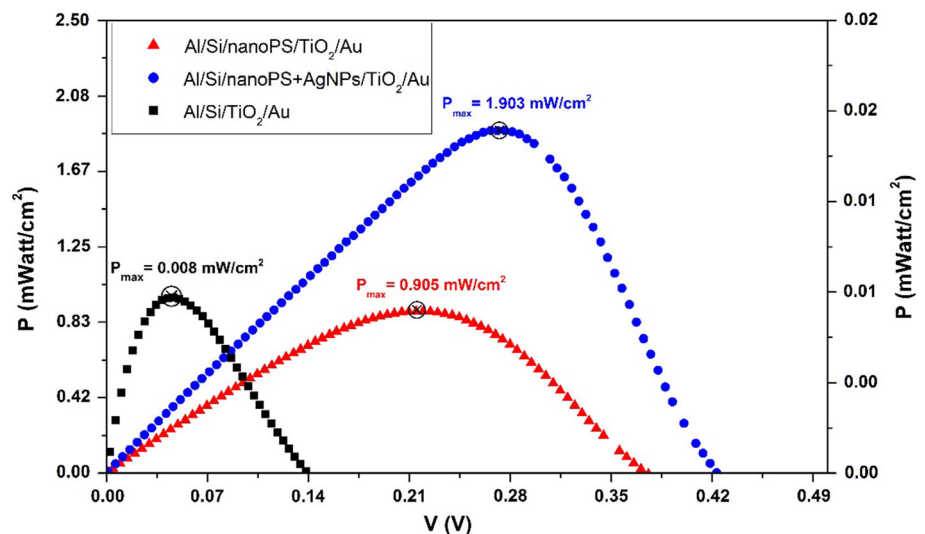
where  $I_m V_m$  is the maximum power point,  $S$  is the active area of the solar cell, and  $P_{in}$  is the power density of the incident light (100 mW/cm<sup>2</sup>).

It is important to mention that the addition of TiO<sub>2</sub> thin films to the Schottky junction devices has several advantages. First of all, they serve as interfacial layers to improve  $V_{oc}$  by hole blocking and electron transportation. As a result of the wide band gap of the TiO<sub>2</sub> thin films (3.82 eV, “[Reflectance spectra](#)” section), the TiO<sub>2</sub>/active layer interfaces are expected to have a large valence band barrier ( $\Delta E_v \sim 2.5$  eV), which would block the transport of holes from the active layer to the TiO<sub>2</sub> thin film. However, these interfaces are expected to possess a small conduction-band barrier ( $\Delta E_c \sim 0.1$  eV), which would allow transport of electrons from the active layer to the TiO<sub>2</sub> thin film [43] (see energy band diagrams, Fig. 6). Second, the TiO<sub>2</sub> thin films serve as antireflective coatings. Third, the TiO<sub>2</sub> thin films passivate the surface of the active layer and prevent it from oxidation, in addition to the notable reduction in surface recombination rates associated with nanoPS. This enhancement was observed from the photovoltaic parameters for the Al/Si/nanoPS/TiO<sub>2</sub>/Au and Al/Si/nanoPS+AgNPs/TiO<sub>2</sub>/Au devices. Finally, in the case of the latter devices, which have shown the highest efficiency, the interaction between TiO<sub>2</sub> (dielectric layer) with AgNPs led to an enhancement in the optoelectronic properties due to the manifestation

**Table 1** Photovoltaic characteristics of the three MIS Schottky solar cells under study

Device structure	$J_{sc}$ (mA/cm <sup>2</sup> )	$V_{oc}$ (V)	FF	$\eta$ (%)
Al/Si/TiO <sub>2</sub> /Au	0.43	0.14	13.5	0.008
Al/Si/nanoPS/TiO <sub>2</sub> /Au	5.52	0.38	42.7	0.9
Al/Si/nanoPS+AgNPs/TiO <sub>2</sub> /Au	8.07	0.42	55.9	1.9

**Figure 9** Maximum power density point determination for the Al/Si/TiO<sub>2</sub>/Au, Al/Si+nanoPS/TiO<sub>2</sub>/Au, and Al/Si/nanoPS+AgNPs/TiO<sub>2</sub>/Au photovoltaic devices.



of SPR effects in the blue region of the electromagnetic spectrum (Fig. 4).

In conclusion, the optoelectronic enhancement for the Al/Si/nanoPS+AgNPs/TiO<sub>2</sub>/Au devices shown in Figs. 7 and 8 is attributed to five main factors: (1) Reduction in the recombination rates by improving surface passivation, (2) improved light trapping by the use of TiO<sub>2</sub> thin film as antireflective coating, (3) increased light absorption by the nanoPS layer, (4) SPR effects associated with the presence of AgNPs, and (5) improved electrical conduction of the active layer by the presence of AgNPs.

Finally, it is worth pointing out that the results here presented are comparable to those obtained for several Schottky barrier junction solar cells based on crystalline Si and low-dimensional structures. For example,  $J_{sc} = 0.396 \text{ mA/cm}^2$  and  $V_{oc} = 0.429 \text{ V}$  have recently been obtained for Schottky junction solar cell based on Si nanowires and multi-layered graphene after optimizing the number of graphene layers [53],  $\eta = 1.25\%$  was obtained for Schottky junction solar cells based on patterned graphene and CdS nanobelts [54],  $\eta = 1.65\%$  for Au-graphene/CdS nanowires Schottky junction solar cells [55], and plasmonic enhancement in MIS Schottky junction solar cells by introducing Ag NPs and SiO<sub>x</sub> spacer layers on top of the junction, where  $J_{sc}$  improved from  $13.7 \text{ mA/cm}^2$  for the reference cell to  $19.7 \text{ mA/cm}^2$  after optimizing the size, shape, and distributions of Ag NPs [56].

## Conclusions

We have analyzed in detail the optoelectronic performance of three different MIS Schottky junction solar cells, namely Al/Si/TiO<sub>2</sub>/Au, Al/Si/nanoPS/TiO<sub>2</sub>/Au, and Al/Si/nanoPS+AgNPs/TiO<sub>2</sub>/Au structures. A remarkable improvement in the photovoltaic performance of the devices was found upon the addition of nanoPS and AgNPs. To understand the different photogeneration and conduction mechanisms, an energy band model was proposed for the different devices.

The large increase in the overall photovoltaic performance of the Al/Si/nanoPS+AgNPs/TiO<sub>2</sub>/Au devices is attributed to two main reasons, in addition to the reflectance reduction and the passivation provided by the nanoPS layers. First, the small size of the AgNPs (5–15 nm) leads to the manifestation of SPR effects in the blue region of the electromagnetic

spectrum. Second, the metallic AgNPs improved the electrical conduction of the nanoPS layers.

It is worth pointing out that the growth of TiO<sub>2</sub> thin films most likely does not completely passivate the surface of nanoPS due to the presence of small mesopores (5–30 nm). As such, radiative recombination mechanisms through oxygen vacancies in the small nanopores of the surface of nanoPS still may exist for the Al/Si/nanoPS/TiO<sub>2</sub>/Au devices. However, surface passivation of nanoPS was highly improved by the chemical process used for the infiltration of silver nanoparticles leading to the Al/Si/nanoPS+AgNPs/TiO<sub>2</sub>/Au structures.

## Acknowledgements

The authors are thankful to Mr. Luis García Pelayo and Dr. Valentin Constantin Nistor for technical support.

## Funding

Funding was provided by Egyptian Ministry of Higher Education, Missions Section under Egyptian Joint Supervision Grant, call 015/016.

## Compliance with ethical standards

**Conflict of interest** The authors declare that they have no conflict of interest.

## References

- [1] Nelson J (2003) The physics of solar cells. World Scientific Publishing Company, Singapore
- [2] de la Morena SS, Recio-Sánchez G, Torres-Costa V, Martín-Palma R (2014) Hybrid gold/porous silicon thin films for plasmonic solar cells. *Scr Mater* 74:33–37
- [3] Zhou L, Xiao L, Yang H, Liu J, Yu X (2018) Greatly enhanced photovoltaic performance of crystalline silicon solar cells via metal oxide. *Nanomaterials* 8:505
- [4] Wang X, Peng KQ, Pan XJ, Chen X, Yang Y, Li L, Meng XM, Zhang WJ, Lee ST (2011) High-performance silicon nanowire array photoelectrochemical solar cells through surface passivation and modification. *Angew Chem Int Ed* 50:9861–9865
- [5] Garnett E, Yang P (2010) Light trapping in silicon nanowire solar cells. *Nano Lett* 10:1082–1087

- [6] Peng KQ, Lee ST (2011) Silicon nanowires for photovoltaic solar energy conversion. *Adv Mater* 23:198–215
- [7] Jasim KE (2015) Quantum dots solar cells, chapter 11. In: Kosyachenko LA (ed) *Solar cells: new approaches and reviews*. InTech Open Publishing Company, Croatia
- [8] Kim JH, Shin DH, Lee HS, Jang CW, Kim JM, Seo SW, Kim S, Choi S-H (2017) Enhancement of efficiency in graphene/porous silicon solar cells by co-doping graphene with gold nanoparticles and bis (trifluoromethanesulfonyl)-amide. *J Mater Chem C* 5:9005–9011
- [9] Dewan R, Jovanov V, Hamraz S, Knipp D (2014) Analyzing periodic and random textured silicon thin film solar cells by rigorous coupled wave analysis. *Sci Rep* 4:6029
- [10] Schneider BW, Lal NN, Baker-Finch S, White TP (2014) Pyramidal surface textures for light trapping and antireflection in perovskite-on-silicon tandem solar cells. *Opt Express* 22:A1422–A1430
- [11] Farhat M, Kais S, Alharbi F (2017) Plasmonically enhanced Schottky photovoltaic devices. *Sci Rep* 7:14253
- [12] Pulfrey DL (1978) MIS solar cells: a review. *IEEE Trans Electron Dev* 25:1308–1317
- [13] Shewchun J, Burk D, Spitzer MB (1980) MIS and SIS solar cells. *IEEE Trans Electron Dev* 27:705–716
- [14] Sharma B (2013) *Metal-semiconductor Schottky barrier junctions and their applications*. Springer, Berlin
- [15] Martín-Palma RJ, McAtee PD, Ramadan R, Lakhtakia A (2019) Hybrid nanostructured porous silicon-silver layers for wideband optical absorption. *Sci Rep* 9:7291
- [16] Harizi A, Laatar F, Ezzaouia H (2019) Physical properties enhancement of porous silicon treated with  $\text{In}_2\text{O}_3$  as an antireflective coating. *Results Phys* 12:1716–1724
- [17] Iatsunskyi I, Pavlenko M, Viter R, Jancelewicz M, Nowaczyk G, Baleviciute I, Załęski K, Jurga S, Ramanavicius A, Smyntyna V (2015) Tailoring the structural, optical, and photoluminescence properties of porous silicon/ $\text{TiO}_2$  nanostructures. *J Phys Chem C* 119:7164–7171
- [18] Schmidt J, Kerr M, Cuevas A (2001) Surface passivation of silicon solar cells using plasma-enhanced chemical-vapour-deposited SiN films and thin thermal  $\text{SiO}_2$ /plasma SiN stacks. *Semicond Sci Technol* 16:164
- [19] Titova V, Veith-Wolf B, Startsev D, Schmidt J (2017) Effective passivation of crystalline silicon surfaces by ultrathin atomic-layer-deposited  $\text{TiO}_x$  layers. *Energy Procedia* 124:441–447
- [20] Schmidt J, Veith B, Brendel R (2009) Effective surface passivation of crystalline silicon using ultrathin  $\text{Al}_2\text{O}_3$  films and  $\text{Al}_2\text{O}_3/\text{SiN}_x$  stacks. *Physica Status Solidi (RRL) Rapid Res Lett* 3:287–289
- [21] von Roedern B (2001) How do buffer layers affect solar cell performance and solar cell stability? In: MRS online proceedings library archive, vol 668
- [22] Lee Y-T, Lin F-R, Lin T-C, Chen C-H, Pei Z (2016) Low-temperature, chemically grown titanium oxide thin films with a high hole tunneling rate for Si solar cells. *Energies* 9:402
- [23] Elshorbagy MH, Cuadrado A, Alda J (2017) High-sensitivity integrated devices based on surface plasmon resonance for sensing applications. *Photon Res* 5:654–661
- [24] Steiner P, Kozłowski F, Wielunski M, Lang W (1994) Enhanced blue-light emission from an indium-treated porous silicon device. *Jpn J Appl Phys* 33:6075
- [25] Andsager D, Hilliard J, Nayfeh MH (1994) Behavior of porous silicon emission spectra during quenching by immersion in metal ion solutions. *Appl Phys Lett* 64:1141–1143
- [26] Hosny M, Wissem D, Ikbel H, Hatem E (2014) Influence of gold nanoparticles deposition on porous silicon properties. *Sens Transducers* 27:202
- [27] Liu K, Bi Y, Qu S, Tan F, Chi D, Lu S, Li Y, Kou Y, Wang Z (2014) Efficient hybrid plasmonic polymer solar cells with Ag nanoparticle decorated  $\text{TiO}_2$  nanorods embedded in the active layer. *Nanoscale* 6:6180–6186
- [28] Langlet M, Jenouvrier P, Kim A, Manso M, Valdez MT (2003) Functionality of aerosol-gel deposited  $\text{TiO}_2$  thin films processed at low temperature. *J Sol-Gel Sci Technol* 26:759–763
- [29] Ramadan R, Romera D, Carrascón RD, Cantero M, Aguilera-Corrae J-J, García Ruiz JP, Esteban J, Silván MM (2019) Sol-Gel-deposited Ti-doped ZnO: toward cell fouling transparent conductive oxides. *ACS Omega* 4:11354–11363
- [30] Martín-Palma R, Pascual L, Herrero P, Martínez-Duart J (2002) Direct determination of grain sizes, lattice parameters, and mismatch of porous silicon. *Appl Phys Lett* 81:25–27
- [31] Martín-Palma R, Pascual L, Herrero P, Martínez-Duart J (2005) Monte Carlo determination of crystallite size of porous silicon from X-ray line broadening. *Appl Phys Lett* 87:211906
- [32] Torres-Costa V, Martín-Palma R (2010) Application of nanostructured porous silicon in the field of optics. A review. *J Mater Sci* 45:2823–2838. <https://doi.org/10.1007/s10853-010-4251-8>
- [33] Ramadan R, Martín-Palma RJ (2019) AC & DC electrical conduction of the interfaces of MIS Schottky barrier diodes based on silicon nanostructures and Ag nanoparticles
- [34] Chau Y-FC, Chao C-TC, Chiang H-P, Lim CM, Voo NY, Mahadi AH (2018) Plasmonic effects in composite metal

- nanoparticles for sensing applications. *J Nanoparticle Res* 20:190
- [35] Mock J, Barbic M, Smith D, Schultz D, Schultz S (2002) Shape effects in plasmon resonance of individual colloidal silver nanoparticles. *J Chem Phys* 116:6755–6759
- [36] McLachlan D, Priou A, Chenierie I, Issac E, Henry F (1992) Modeling the permittivity of composite materials with a general effective medium equation. *J Electromag Waves Appl* 6:1099–1131
- [37] Mackay TG, Lakhtakia A (2006) Percolation thresholds in the homogenization of spheroidal particles oriented in two directions. *Opt Commun* 259:727–737
- [38] Watanabe R, Eguchi Y, Yamada T, Saito Y (2015) Optical properties of spin-coated TiO<sub>2</sub> antireflection films on textured single-crystalline silicon substrates. *Int J Photoenergy* 2015:1–8
- [39] Kelly KL, Coronado E, Zhao LL, Schatz GC (2003) The optical properties of metal nanoparticles: the influence of size, shape, and dielectric environment. ACS Publications, Washington
- [40] Ramadan R, Abdelhady K, Manso-Silvan M, Torres-Costa V, Martın-Palma RJ (2019) Microwave plasma and rapid thermal processing of indium-tin oxide thin films for enhancing their performance as transparent electrodes. *J Photon Energy* 9:034001
- [41] Chrysicopoulou P, Davazoglou D, Trapalis C, Kordas G (1998) Optical properties of very thin (< 100 nm) sol-gel TiO<sub>2</sub> films. *Thin Solid Films* 323:188–193
- [42] Zhao B-X, Zhou J-C, Rong L-Y (2010) Microstructure and optical properties of TiO<sub>2</sub> thin films deposited at different oxygen flow rates. *Trans Nonferrous Met Soc China* 20:1429–1433
- [43] Avasthi S, McClain WE, Man G, Kahn A, Schwartz J, Sturm JC (2013) Hole-blocking titanium-oxide/silicon heterojunction and its application to photovoltaics. *Appl Phys Lett* 102:203901
- [44] Shin DH, Kim JH, Kim JH, Jang CW, Seo SW, Lee HS, Kim S, Choi S-H (2017) Graphene/porous silicon Schottky-junction solar cells. *J Alloys Compd* 715:291–296
- [45] Gallach-Perez D, Munoz-Noval A, Garcıa-Pelayo L, Manso-Silvan M, Torres-Costa V (2017) Tunnel conduction regimes, white-light emission and band diagram of porous silicon–zinc oxide nanocomposites. *J Lumin* 191:107–111
- [46] Hsu C-H, Lo H-C, Chen C-F, Wu CT, Hwang J-S, Das D, Tsai J, Chen L-C, Chen K-H (2004) Generally applicable self-masked dry etching technique for nanotip array fabrication. *Nano Lett* 4:471–475
- [47] Dzhafarov T (2013) Silicon solar cells with nanoporous silicon layer, chapter 2. In: Morales-Acevedo A (ed) *Solar cells: research and application perspectives*. InTech Open Publishing Company, Croatia
- [48] Al-Douri Y, Ahmed N, Bouarissa N, Bouhemadou A (2011) Investigated optical and elastic properties of Porous silicon: theoretical study. *Mater Des* 32:4088–4093
- [49] Thiel FL, Ghandhi SK (1970) Electronic properties of silicon doped with silver. *J Appl Phys* 41:254–263
- [50] Pascual Sanchez D (2015) Crystalline silicon heterojunction solar cells. Universitat Politecnica de Catalunya
- [51] Martın-Palma R, Perez-Rigueiro J, Martınez-Duart J (1999) Study of carrier transport in metal/porous silicon/Si structures. *J Appl Phys* 86:6911–6914
- [52] Sze SM, Ng KK (2006) *Physics of semiconductor devices*. Wiley, New York
- [53] Lin Y-K, Hong Y-T, Shyue J-J, Hsueh C-H (2019) Construction of Schottky junction solar cell using silicon nanowires and multi-layered graphene. *Superlattices Microstruct* 126:42–48
- [54] Ye Y, Gan L, Dai L, Dai Y, Guo X, Meng H, Yu B, Shi Z, Shang K, Qin G (2011) A simple and scalable graphene patterning method and its application in CdSe nanobelt/graphene Schottky junction solar cells. *Nanoscale* 3:1477–1481
- [55] Ye Y, Dai Y, Dai L, Shi Z, Liu N, Wang F, Fu L, Peng R, Wen X, Chen Z (2010) High-performance single CdS nanowire (nanobelt) Schottky junction solar cells with Au/graphene Schottky electrodes. *ACS Appl Mater Interfaces* 2:3406–3410
- [56] Tong C, Yun J, Song H, Gan Q, Anderson WA (2014) Plasmonic-enhanced Si Schottky barrier solar cells. *Solar Energy Mater Solar Cells* 120:591–595

**Publisher's Note** Springer Nature remains neutral with regard to jurisdictional claims in published maps and institutional affiliations.

## Abbreviations in chapter 5

MIS	metal-insulator-semiconductor
NanoPS	Nanostructured porous Silicon
AgNPs	Silver nanoparticles
PV	photovoltaic
C-Si	Crystalline silicon
MS	Metal–semiconductor
RTP	Rapid thermal processing
Ti[OCH(CH <sub>3</sub> ) <sub>2</sub> ] <sub>4</sub>	Titanium isopropoxide
SPR	surface plasmon resonance
hν	Photon energy
ΔE <sub>v</sub>	Valence band offset
$E_D^{Ag}$	Ionized donor level
$E_A^{Ag}$	Ionized acceptor level
J <sub>sc</sub>	Short circuit current density
FF	Fill factor
η	Conversion efficiency
P <sub>in</sub>	Power density of the incident light
ΔE <sub>c</sub>	Conduction-band barrier



## **Chapter 6:**

### **Self-powered broadband hybrid organic-inorganic photodetectors based on PEDOT:PSS and silicon micro-nanostructures**

R. Ramadan, V. Torres-Costa, & R. J. Martín-Palma, *Journal of Materials Chemistry C*, 9(13), (2021), 4682-4694.

---

Cite this: *J. Mater. Chem. C*, 2021, 9, 4682

# Self-powered broadband hybrid organic–inorganic photodetectors based on PEDOT:PSS and silicon micro-nanostructures

Rehab Ramadan, \*<sup>abc</sup> Vicente Torres-Costa<sup>ac</sup> and Raúl J. Martín-Palma <sup>ac</sup>

Hybrid organic–inorganic self-powered photodetectors with three different configurations were fabricated and their optoelectronic performance was determined. Si is the inorganic active layer and the transparent conductor poly(3,4-ethylenedioxythiophene) polystyrene sulfonate (PEDOT:PSS) is the organic layer. The basic photodetector structure under study is Au/PEDOT:PSS/Si/Al. This device shows high responsivity under low irradiation levels, as well as a wideband response in the visible and near-infrared wavelength ranges. To improve the performance of this basic device, its structure was modified by the addition of a nanostructured porous silicon (PSi) layer on top of the Si substrate. The resulting Au/PEDOT:PSS/PSi/Si/Al devices have been found to show improved photoresponse under high irradiation levels together with narrowband spectral responsivity in the infrared region. To further improve the optoelectronic performance of the photodetectors, Si + PSi micro-arrays were used instead of single PSi layers, leading to devices with the structure Au/PEDOT:PSS/(Si + PSi micro-arrays)/Si/Al. These devices possess a much improved performance, showing a responsivity of 1172.87 mA W<sup>-1</sup>, a specific detectivity of 5.81 × 10<sup>13</sup> Jones, and a fast response speed of 396/412 μs at 0 V bias under white-light illumination (100 μW). Furthermore, a broadband spectral responsivity was achieved, with a maximum value of 473 mA W<sup>-1</sup> at 853 nm. This improved behavior is associated with the combined effect of an effective reduction of the reflectance due to the presence of PSi and an improvement of the electrical conduction given by the presence of heavily-doped Si regions.

Received 24th January 2021,  
Accepted 8th March 2021

DOI: 10.1039/d1tc00329a

rsc.li/materials-c

## 1. Introduction

Self-powered photodetectors possess high potential for use in numerous applications in diverse fields such as optical communications, biomedicine, gas sensing, and video imaging.<sup>1</sup> Depending on their wavelength response, there are selective and broadband photodetectors. Broadband photodetectors with high detection efficiency, fast speed, high operation stability, small size, and low cost possess an enormous commercialization potential.

In addition to the many semiconducting materials used for photodetection, hybrid organic–inorganic structures are being increasingly used due to their attractive optical and electrical properties.<sup>2–6</sup> Organic polymers like poly(3-hexylthiophene) (P<sub>3</sub>HT), [6,6]-phenyl-C<sub>61</sub>-butyric acid methyl ester (PC<sub>61</sub>BM),<sup>7</sup> poly(2,7-carbazole-*alt*-4,7-dithienyl-2,1,3-benzothiadiazole),<sup>8</sup> and

poly(3,4-ethylenedioxythiophene) polystyrene sulfonate (PEDOT:PSS)<sup>9,10</sup> are extensively used, not only in photodetectors, but also in solar cells with a remarkable performance. In particular, PEDOT:PSS is one of the most successful conducting polymers. Thorough studies have been carried out on photodetectors based on hybrid PEDOT:PSS/n-type inorganic semiconductor structures which show a promising photoresponse. For instance, blue-sensitive photodetectors with the configuration PEDOT:PSS/SnO<sub>2</sub> microwires show a responsivity of 18.2 mA W<sup>-1</sup> at 450 nm,<sup>10</sup> while that of self-powered (PEDOT:PSS/Ga<sub>2</sub>O<sub>3</sub>) devices is 37.4 mA W<sup>-1</sup> at 254 nm,<sup>11</sup> and that of PEDOT:PSS/Si nanowire arrays based self-powered photodetectors is 37.8 mA W<sup>-1</sup> at 920 nm.<sup>12</sup>

Aiming at their integration into the current CMOS technology, it would be highly desirable to develop highly efficient silicon-based photodetectors in the visible region of the electromagnetic spectrum. However, Si has an indirect bandgap and high optical losses.<sup>13</sup> Structural modifications have been introduced to the surface of Si by many researchers aiming at improving its optical performance, including periodic nanostructures of Si (nanowires, quantum dots and pyramidal shapes) and randomly-textured structures such as porous silicon (PSi).<sup>14–17</sup> However, texturing the

<sup>a</sup> Departamento de Física Aplicada, Universidad Autónoma de Madrid, 28049 Madrid, Spain. E-mail: rehab.ramadan@uam.es; Tel: +34-914974919

<sup>b</sup> Department of Physics, Faculty of Science, Minia University, Minia 61519, Egypt

<sup>c</sup> Instituto de Ciencia de Materiales Nicolás Cabrera, Universidad Autónoma de Madrid, 28049 Madrid, Spain

surface of Si leads to some key disadvantages, *i.e.*, (1) an increased surface-to-volume ratio leading to increased electron-hole recombination rates, (2) fast surface oxidation rates, and (3) reduction of the electrical conductivity due to quantum confinement effects.<sup>18,19</sup>

The main aim of this work is to combine the good electrical properties of Si and the optical enhancement provided by PSi in one device. In this line, integrated micro-nanostructures consisting of ordered micro-arrays of PSi on the surface of Si, *i.e.*, Si + PSi micro-arrays, were fabricated for their subsequent use as self-powered photodetectors. Three configurations of hybrid organic-inorganic PEDOT:PSS-Si self-powered photodetectors were fabricated and studied: the basic Au/PEDOT:PSS/Si/Al structure, where Au and Al provide front and back contacts, and two variants aimed at improving the optical performance of the devices: Au/PEDOT:PSS/PSi/Si/Al and Au/PEDOT:PSS/(Si + PSi micro-arrays)/Si/Al. The PEDOT:PSS layer serves at the same time as a transparent conductor, anti-reflective coating and hole transport layer,<sup>20</sup> while Si, PSi/Si, and (Si + PSi micro-arrays)/Si are the photodetector active layers. The morphology, optical properties, and electrical transport properties of the three different photodetector configurations were analyzed. Furthermore, we compared their photoresponse in a wide range of incident light powers. Their stability and reproducibility to pulsed light were examined at 0 V. Finally, the spectral responsivity was analyzed in a broad wavelength range.

## 2. Experimental

Single-side polished phosphorous-doped (n-type) silicon wafers with (100) orientation were used for the fabrication of three different types of self-powered photodetectors. The properties of the Si wafers are (1–10  $\Omega$  cm) resistivity, (300  $\pm$  15 nm) thickness and surface roughness in the order of 0.1 nm. The wafers were cleaned by ultrasonication in ethanol, acetone and distilled water for 10 minutes each.

### 2.1 Electrochemical etching of the PSi layer

Before the electrochemical etching of the PSi layers, 100 nm thick Al back contacts were deposited by electron beam evaporation. The base pressure was  $1.25 \times 10^{-5}$  mbar and the evaporation time was 2 minutes. The Al thin films were subsequently annealed by rapid thermal processing (RTP) under a nitrogen atmosphere for 5 minutes to turn the initial rectifying junction into an ohmic one. Afterward, the wafers were cut into  $1.5 \times 1.5$  cm<sup>2</sup> pieces. Each sample was mounted in a sample holder with an exposed circular area of 0.785 cm<sup>2</sup>. The native oxide layer was removed by immersing the polished side of the Si substrate into HF/H<sub>2</sub>O solutions (1:20 ratio) for 30 s. Afterwards, the samples were immersed in the etching solution consisting of a 1:1 HF (48 wt%)/methanol (99 wt%) mixture. The anodization current density and time were set at 10 mA cm<sup>-2</sup> and 10 s, respectively. The etching process was carried out at room temperature under illumination with a halogen lamp (60 W). Schematic representation of the electrochemical etching process was portrayed in a previous study.<sup>21</sup>

### 2.2 Fabrication of (Si + PSi micro-arrays) structures

Fabrication of (Si + PSi micro-arrays) micro-nanostructures was executed in two steps. First, micropatterning of the photoresist was carried out on Si substrates using a UV-lithography process. Particularly, a negative photoresist thin film was deposited on a pre-cleaned Si substrate by spin coating at 3000 rpm for 30 s, followed by drying on a hot plate for 15 minutes at 70 °C. A photomask with the desired structure (rectangular patterns of  $55 \times 70$   $\mu\text{m}^2$ ) was fixed on the photoresist/Si stack and exposed to UV radiation for 3 minutes. Afterwards, the photoresist was developed in a NaOH (0.15 M) solution for 6 minutes and washed with distilled water. The developed micropattern of the photoresist/Si was then post-baked for 15 minutes at 70 °C to improve the adhesion of the micropattern to the Si surface. The second step consists of the electrochemical etching of the exposed Si areas. Using the same etching conditions as described in sec. 2.1, PSi was fabricated in the exposed areas of Si, resulting in photoresist + PSi micro-arrays which were thoroughly washed with distilled water. The photoresist was lifted-off by immersing the sample in acetone for 10 minutes, and finally the samples were rinsed several times in ethanol and isopropanol to remove any residues or contamination. Integrated micro-nanostructures of (Si + PSi micro-arrays) were obtained as a result of the two processes (photolithography and electrochemical etching). A schematic view of the fabrication processes of the Si + PSi micro-array structures is shown in Fig. 1.

### 2.3 Spin coating of PEDOT:PSS thin films

The poly(3,4-ethylenedioxythiophene):polystyrene sulfonate (PEDOT:PSS 1.3 wt%) polymer was purchased from Sigma Aldrich. Isopropyl alcohol (IPA) was used to increase the solubility of PEDOT:PSS solution. Dimethylsulfoxide (DMSO) (99.5%) assisted in improving the electrical conduction of the PEDOT:PSS films. Sulphuric acid (98%) was used to improve the surface wettability of the active layers. Distilled water, ethanol (99%) and methanol (99.5) were used for cleaning purposes.

Highly transparent conducting layers of PEDOT:PSS were grown on three types of substrates, *i.e.*, Si, PSi, and Si + PSi micro-arrays. The solution consisted of a 10 : 1 : 1 PEDOT:PSS/ IPA/DMSO mixture. Before the deposition of the PEDOT:PSS thin films, 200  $\mu\text{L}$  of sulphuric acid was dropped on the surface of the substrate for 10 minutes to increase surface wettability. Afterwards, the samples were cleaned by ultrasonication in a distilled water bath for 10 minutes to remove any sulphuric acid residues. 50  $\mu\text{L}$  of the PEDOT:PSS/IPA/DMSO solution was deposited on the pre-cleaned substrates by spin coating. For the deposition, the spin speed was 1000 rpm and the spin time was 60 s. Then, samples were heated at 100 °C for 15 minutes to evaporate any solvents in the PEDOT:PSS layer. The process was repeated twice under the same conditions to obtain thicker PEDOT:PSS films.

### 2.4 Device configurations

Self-powered photodetectors with three different configurations were fabricated. These are Au/PEDOT:PSS/Si/Al, Au/PEDOT:PSS/

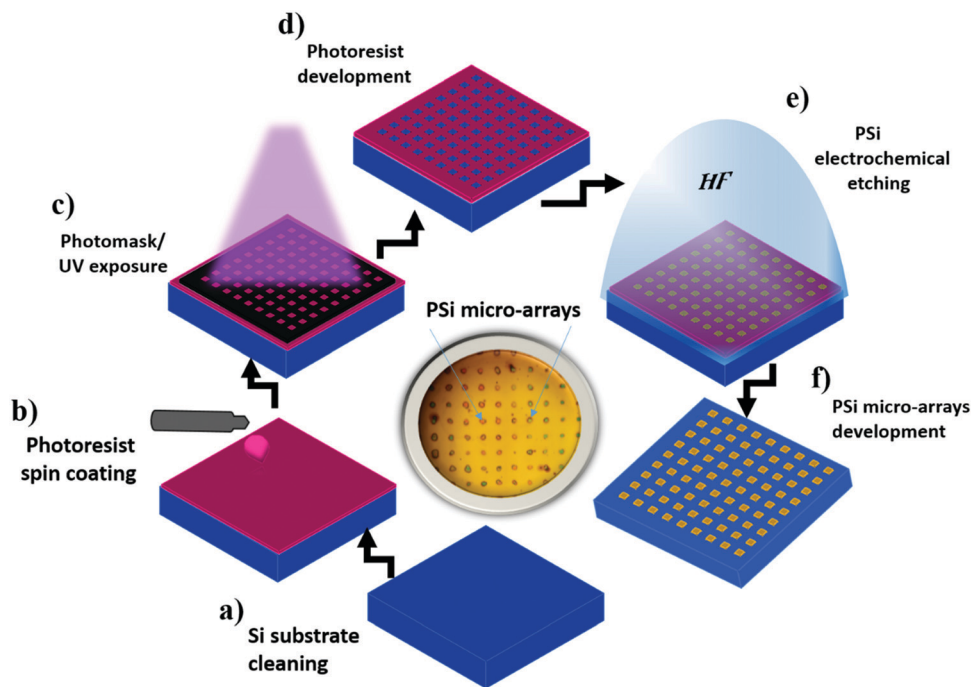


Fig. 1 Schematic view of the photolithography process of the Si substrate and the electrochemical etching of PSi micro-arrays on the Si surface.

PSi/Si/Al, and Au/PEDOT:PSS/(Si + PSi micro-arrays)/Si/Al. Au is the top contact, which is grown by DC-sputtering under an argon atmosphere using a patterned mask. The typical deposition pressure was  $2 \times 10^{-2}$  mbar and the typical plasma current was 20 mA, leading to a thickness of around 50 nm. The PEDOT:PSS thin films serve as transparent conductors. Si, PSi/Si, and (Si + PSi micro-arrays)/Si are the active layers in the self-powered photodetectors, while Al is the back contact (the evaporation

conditions described in Section 2.1). An illustration of the final structure of the three different photodetectors is presented in Fig. 2, including FESEM images of the active layer of each device.

## 2.5 Characterization techniques

The morphology of the PEDOT:PSS thin films and the active layers were studied by field emission scanning electron microscopy (FESEM) using a Philips XL-40FEG microscope operated at 5 kV.

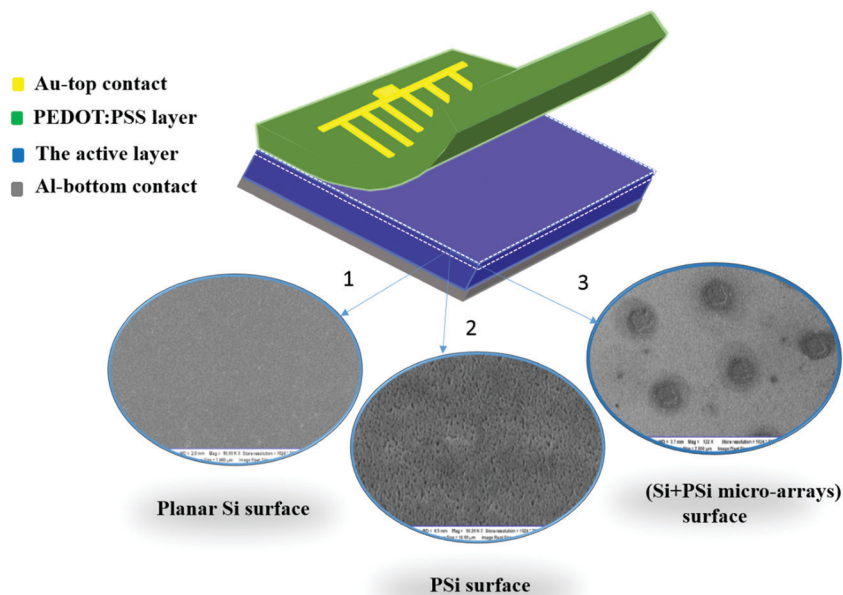


Fig. 2 Schematic view of the self-powered photodetectors including top and bottom contacts and FESEM top-view images of the active layer of the three devices.

Optical characterization in the UV-visible-near-infrared range (250–900 nm) was carried out using a Jasco V-560 double-beam spectrophotometer, equipped with an integrating sphere to avoid scattering losses.

The electrical and optoelectronic analysis of the photodetectors were carried out in a BioLogic SP-150 potentiostat. A homemade cell consisting of two movable copper probes with a diameter of 0.5 mm and a copper base ( $2 \times 2 \text{ cm}^2$ ) was used for all the electrical measurements. Current–voltage ( $I$ – $V$ ) curves in the dark were obtained at a scan rate  $10 \text{ mV s}^{-1}$  and applied potential in the  $-0.5$  to  $+0.5 \text{ V}$  range. Electrochemical impedance spectroscopy (EIS) measurements were executed without external voltage in the 200 mHz to 1 MHz frequency range.

A solar simulator (LCS-100 Solar Simulator-Model 94011A), with an adjustable illumination output power, was used for photoresponse measurements.  $I$ – $V$  curves under illumination were recorded in a wide range of incident light powers: 0.1, 1, 5, 15, 30, 50, 80, and  $100 \text{ mW cm}^{-2}$ . Time-dependent current ( $I$ – $t$ ) curves (ON/OFF response) were recorded under the same incident light powers (0.1, 1, 5, 15, 30, 50, 80, and  $100 \text{ mW cm}^{-2}$ ), every  $2 \mu\text{A}$  with time steps of  $dt = 0.15 \text{ s}$  at 0 V bias. The response speed of the photodetectors was examined every 20 ms using a light source with an intensity of  $400 \mu\text{W}$ .

The spectral responsivity in the 300 to 1200 nm wavelength range was determined at 0 V bias using a dual digital lock-in amplifier (Signal Recovery 7225) at a chopper frequency of 300 Hz. Illumination was provided by an Acton Research Corporation Tungsten-Deuterium dual light source (model TDS-429) and a SpectraPro 150 monochromator equipped with two interchangeable diffraction gratings (1200 lines per mm) was used to select the wavelength. The photoresponse of the devices to single-wavelength light was examined by analysing the  $I$ – $t$  curves (*i.e.*, ON/OFF response) at 0 V bias in different wavelength regions by adjusting the monochromatic light.

### 3. Results and discussion

Self-powered photodetectors with three different configurations were fabricated for the subsequent evaluation of their optoelectronic performance. The structure of these devices is described in the Experimental section.

#### 3.1 Morphological characterization

As a first step toward the analysis of the overall performance of the self-powered photodetectors, their morphology was analyzed by FESEM, as depicted in Fig. 3 and 4. Fig. 3a shows a typical cross-sectional image of the PEDOT:PSS layer grown on the flat Si surface, which confirms a uniform coverage of the underlying Si substrate with a 90 nm thick film. Fig. 3b shows a characteristic cross-sectional view of the PEDOT:PSS/PSi/Si interface, from which it can be noted that a 30 nm PSi layer shows a columnar structure with typical pore diameters in the 5 nm to 10 nm range. Furthermore, the PEDOT:PSS thin films grown on the PSi surface show a good homogeneity, with a thickness of around 80 nm. The inset of Fig. 3b shows that the pores of the PSi layer are

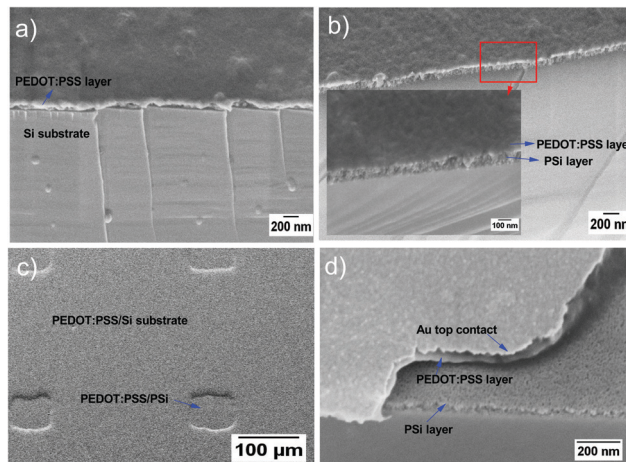


Fig. 3 Typical FESEM images of PEDOT:PSS/active layers of the Si-based photodetectors. (a) Cross-sectional view of the PEDOT:PSS/Si interface, (b) cross-sectional view of PEDOT:PSS/PSi/Si interfaces, (c) top-view of the PEDOT:PSS/(Si + PSi micro-arrays) surface, and (d) cross-sectional view of Au/PEDOT:PSS/PSi interfaces.

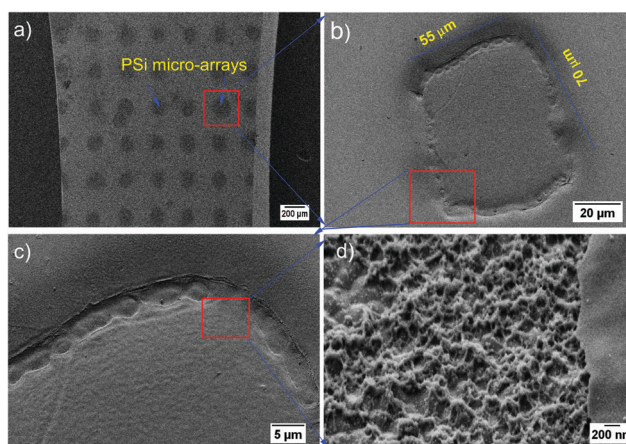


Fig. 4 Typical top-views of the (Si + PSi micro-arrays) structure at different magnifications. (a) An overview of PSi micro-arrays pattern grown on the Si substrate, (b) single rectangular PSi micro-array dimensions, (c) magnified image for the interface between Si and PSi, and (d) the morphology of PSi grown into the micropattern.

partially filled with PEDOT:PSS, which explains the fact that the PEDOT:PSS layer is thinner than that grown on flat Si.

Top view of the PEDOT:PSS/(Si + PSi micro-arrays) surface is shown in Fig. 3c, showing a homogeneous surface coverage. Again, the partial infiltration of PEDOT:PSS into the PSi pores is revealed by the changes in surface height at the PSi locations. Fig. 3d shows a characteristic cross-sectional view of the Au top contact, PEDOT:PSS layer and PSi layer. The thickness of these layers are 50, 80, and 30 nm, respectively.

Fig. 4 portrays typical FESEM images of the Si + PSi micro-arrays at different magnifications. Fig. 4a shows an overview of the PSi micro-arrays after photoresist development during the lithography process. The distance between the two micropatterns

is 225  $\mu\text{m}$  and the surface area of rectangular micro-arrays is  $55 \times 70 \mu\text{m}^2$ . Detailed views at different magnifications of a single micro-array are depicted in Fig. 4b–d.

### 3.2 Optical behavior

PSi can be regarded as a mixture of Si nanocrystallites, amorphous Si and air (pores).<sup>18,19</sup> Accordingly, its optical properties greatly depend on its porosity and thickness.<sup>22–25</sup> As a consequence, these parameters can be adjusted to produce high optical absorption in a broad wavelength range. However, the reduction in the overall reflectance is accompanied by a decrease of electrical conductivity associated with a higher porosity and a higher oxidation degree.<sup>26,27</sup> As such, the combination of silicon and PSi on the active layer can be an ideal strategy to combine the optical tunability of PSi and the high electrical conductivity of highly-doped Si in the same device. For this reason, rectangular micro-arrays of PSi were etched on the surface of photolithographic flat Si, termed Si + PSi micro-arrays.

Fig. 5a shows the comparison between the optical reflectance in the 250 to 900 nm wavelength range of flat Si, PSi (10 mA  $\text{cm}^{-2}$ , 10 s)/Si, and (Si + PSi micro-arrays)/Si. As expected, the growth of a PSi layer onto Si results in a remarkable reduction of the overall reflectance, while the presence of Si + PSi micro-arrays results only in a rather small decrease in reflectance. The subsequent growth of the PEDOT:PSS thin films on the surface of the different active layers leads to a further reduction of the optical reflectance in the three cases, as depicted in Fig. 5b. This effect is attributed to the anti-reflective properties of PEDOT:PSS.<sup>15,20,28</sup> The average reflectance ( $R_{\text{av}}$ ) in the 250–900 nm wavelength range was found to be 22.38%, 14.83 and 9.73% when PEDOT:PSS is grown on Si, PSi and Si + PSi micro-arrays, respectively. In particular, the average reflectance of the Si + PSi micro-arrays coated with PEDOT:PSS is 33% lower than that of the PEDOT:PSS/Si junction, and almost 50% lower in the central visible region.

### 3.3 Electrical conduction and carrier transport characteristics

AC and DC electrical measurements were carried out aiming at studying the electrical conduction properties through the interfaces of the Si-based photodetectors. Fig. 6a portrays the  $I$ – $V$  curves

for the three devices in the  $-0.5$  V to  $0.5$  V range from which a rectifying behavior is clearly observed in all cases. The rectifying behavior shown by the photodetectors under study confirms the contribution of PEDOT:PSS as a hole transport and an electron blocking layer as discussed below in the energy band diagrams section. Accordingly, Si (or PSi/Si or (Si + PSi micro-arrays)/Si) is assumed to be the active layer responsible for the generation of the carriers. This assumption agrees with previous studies of devices based on PEDOT:PSS/Si junctions.<sup>12</sup> The Au/PEDOT:PSS/Si/Al devices show dark-current values higher than those of the modified Au/PEDOT:PSS/PSi/Si/Al devices, which can be attributed to the intrinsic low conductivity of PSi. However, the Au/PEDOT:PSS/(Si + PSi micro-arrays)/Si/Al devices show dark-current values close to those of the Au/PEDOT:PSS/Si/Al devices. This behavior is probably due to the contribution of the heavily-doped Si areas present in the structure of the active layer (Si + PSi micro-arrays), as shown in Fig. 4a.

The electrical transport properties through the various interfaces of the photodetectors were studied by EIS. In this regard, Fig. 6b–d show the Nyquist plots for the Au/PEDOT:PSS/Si/Al, Au/PEDOT:PSS/PSi/Si/Al and Au/PEDOT:PSS/(Si + PSi micro-arrays)/Si/Al photodetectors, respectively. The measurements were carried out in the dark at 0 V bias. Fig. 7 presents the most suitable equivalent circuit models which result from fitting the experimental data. The proposed models comprise one series resistance ( $R_s$ ) and three additional circuits consisting of a resistor ( $R$ ) in parallel with a capacitor ( $C$ ). As indicated in Fig. 7, each of these circuits has been associated with a specific interface in the device. The circuit associated with the active layer/PEDOT:PSS interface consists of a resistor in parallel with a constant phase element ( $Q$ ). This element  $Q$  models an imperfect capacitor associated with inhomogeneity in the composition or/and thickness of the corresponding interface.<sup>29</sup> Thus, its characteristic capacitance,  $C$ , can be calculated by the following equation:<sup>30</sup>

$$C = Q^{\frac{1}{a}} \cdot R^{\frac{1-a}{a}} \quad (1)$$

where factor  $a$  is an index that represents the degree of “perfection” of this element. This index can vary between 0 and 1, with 0

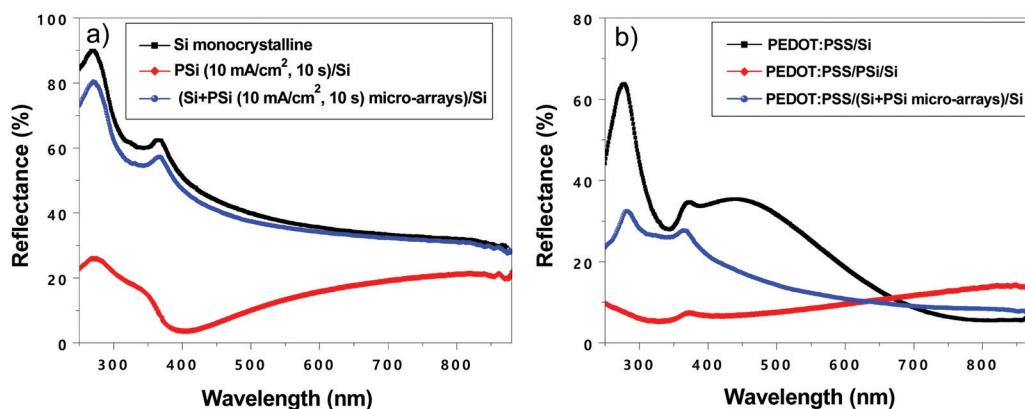


Fig. 5 Typical optical reflectance in the 250 to 900 nm wavelength range. (a) Reflectance of the active layers (Si, PSi/Si and (Si + PSi micro-arrays)/Si). (b) Reflectance of the PEDOT:PSS layer grown on Si, PSi/Si and (Si + PSi micro-arrays)/Si layers.

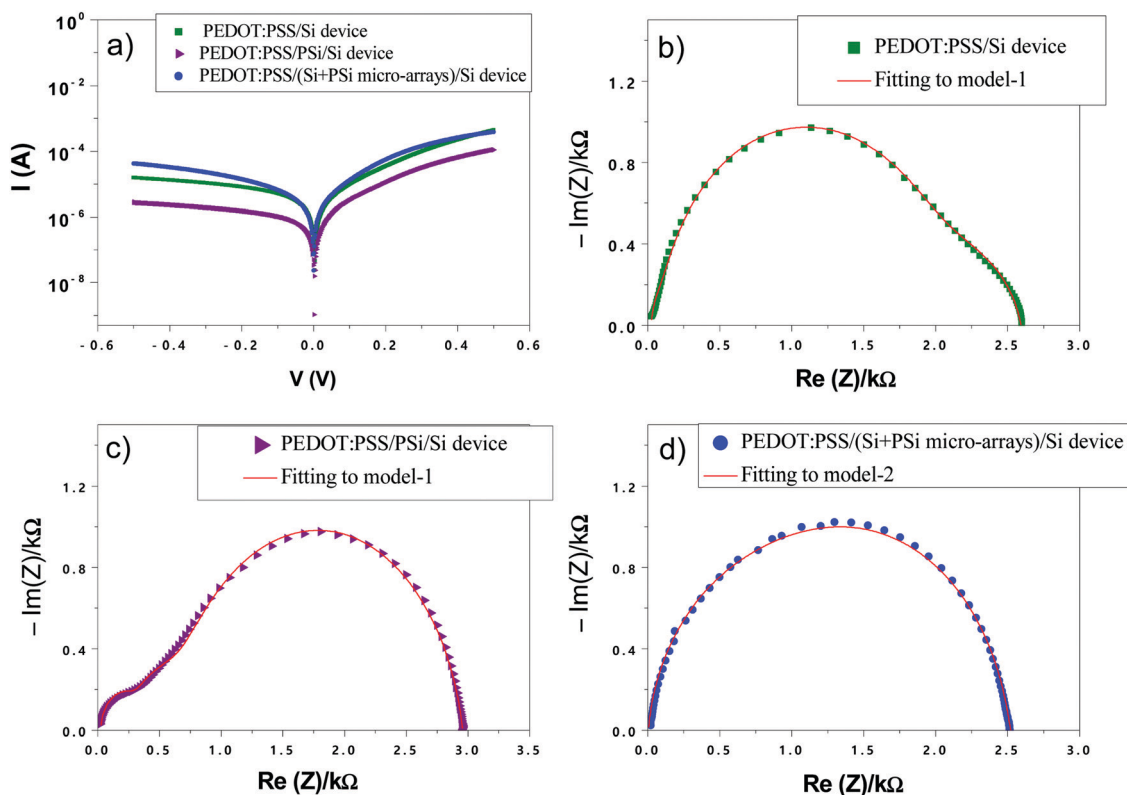


Fig. 6 (a)  $I$ - $V$  curves of the three devices in the dark state. (b) Nyquist plot for PEDOT:PSS/Si devices with the fitting to the equivalent circuit model-1. (c) Nyquist plot for PEDOT:PSS/PSi/Si devices with the fitting to the equivalent circuit model-1. (d) Nyquist plot for PEDOT:PSS/(Si + PSi micro-arrays)/Si devices with the fitting to the equivalent circuit model-2.

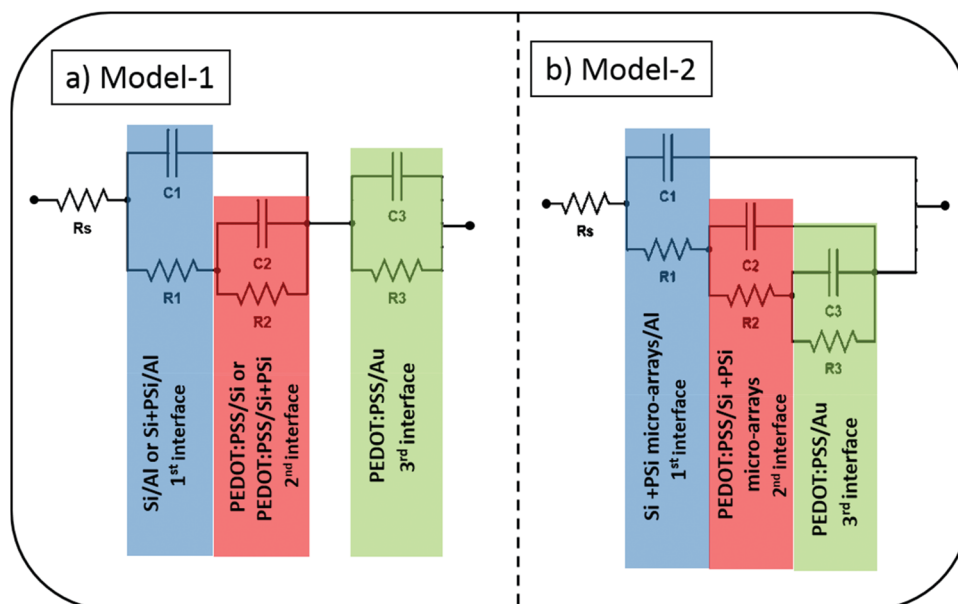


Fig. 7 The equivalent circuit models with the indication of the three interfaces. (a) Model-1 used to fit the Au/PEDOT:PSS/Si/Al and Au/PEDOT:PSS/PSi/Si/Al photodetectors and (b) model-2 applied to fit the Au/PEDOT:PSS/(Si + PSi micro-arrays)/Si/Al photodetectors.

describing a perfect resistor, and 1 a perfect capacitor.<sup>29</sup> The Au/PEDOT:PSS/Si/Al and Au/PEDOT:PSS/PSi/Si/Al photodetectors

were fitted to the same model, given in Fig. 7a and b shows the model corresponding to the Au/PEDOT:PSS/(Si + PSi micro-arrays)/Si/Al

Table 1 Comparison between the electrical parameters obtained from the fitting of the Nyquist plots to the suitable equivalent circuit models

Device structure	$R_s$ ( $\Omega$ )	$R_1$ (k $\Omega$ )	$C_1$ (nF)	$R_2$ (k $\Omega$ )	$Q_1$ $\mu$ F s $^{(a-1)}$	$a$	$C_2$ (nF)	$R_3$ ( $\Omega$ )	$C_3$ (nF)
		1st interface		2nd interface		3rd interface			
Au/PEDOT:PSS/Si/Al	26.14	1.91	23.49	0.55	4.16	0.82	52.7	98.80	36.47
Au/PEDOT:PSS/PSi/Si/Al	26.05	0.55	56.59	2.09	0.75	0.86	27.6	284	8.18
Au/PEDOT:PSS/(Si + PSi micro-arrays)/Si/Al	25.5	0.48	12	1.46	0.11	0.74	0.04	543.6	75.3

photodetectors. Table 1 summarizes the interfaces of the three Si-based photodetectors and the values of the electrical RC elements. Therefore, the  $R_s$  values for the three structures are rather small, which is an indication of the good overall properties of the metallic contacts.

It is important to point out that the modifications in the structure of the active layers have a remarkable effect on the electrical parameters. For instance, the interface PEDOT:PSS/Si + PSi has a lower electrical conduction ( $R_2 = 2.09$  k $\Omega$ ) compared to that of the PEDOT:PSS/Si interface ( $R_2 = 0.55$  k $\Omega$ ). However, the PEDOT:PSS/Si + PSi micro-array interface shows better conduction properties, with  $R_2 = 1.46$  k $\Omega$ . These results are in agreement with those obtained from the analysis of the  $I$ - $V$  curves in the dark (Fig. 6a). For instance, at 0.5 V the Au/PEDOT:PSS/(Si + PSi micro-arrays)/Si/Al devices show values of dark current similar to those of the basic Au/PEDOT:PSS/Si/Al devices. However, Au/PEDOT:PSS/PSi/Si/Al devices show lower values of dark current under the same bias.

### 3.4 Optoelectronic properties and photoresponse

#### 3.4.1 Current-voltage characteristic under illumination.

Fig. 8 depicts the  $I$ - $V$  curves for the Au/PEDOT:PSS/Si/Al photodetectors and the modified structures, *i.e.*, Au/PEDOT:PSS/PSi/Si/Al and Au/PEDOT:PSS/(Si + PSi micro-arrays)/Si/Al, under different light irradiation intensities ranging from 100 mW cm $^{-2}$  to 1 mW cm $^{-2}$ . The experimental results clearly demonstrate the remarkable photovoltaic effect shown by the three devices. In all cases increased incident light power results in a notable increase in both photo-current ( $I_{ph}$ ) and open-circuit voltage ( $V_{oc}$ ). This behavior is attributed to the generation of electron-hole pairs as a result of the absorption of photons.<sup>31</sup> The specific mechanism of photo-carrier generation is discussed in the next section (energy band diagrams).  $I_{ph}$  for the Au/PEDOT:PSS/PSi/Si/Al devices is in general larger than that of the Au/PEDOT:PSS/Si/Al devices. However, under low light irradiation levels (15 mW or lower), both  $I_{ph}$  and  $V_{oc}$  are slightly smaller. This behavior is associated with the reduction in the electrical conductivity by the PSi layer, as given in Fig. 6. At low irradiation levels, the photoresponse decreases and the carrier separation in the active layer is reduced. Complementarily, the  $I$ - $V$  curve of the Au/PEDOT:PSS/PSi/Si/Al device shows lower  $V_{oc}$  values compared to the base structure (Au/PEDOT:PSS/Si/Al).

The reduction in the optical reflectance of the active layer of the photodetectors is not usually enough to enhance the overall photovoltaic performance over a wide range of light irradiation levels.<sup>32</sup> As such, Si + PSi micro-arrays were added to the basic

structure, leading to devices with the structure Au/PEDOT:PSS/(Si + PSi micro-arrays)/Si/Al. These modified devices combine a reduction in the reflectance of the active layer associated with the presence of PSi micro-arrays (Fig. 4b) and limited electrical conduction losses (Fig. 6). As a consequence of the structural modifications of the active layer surface, an outstanding performance for the Au/PEDOT:PSS/(Si + PSi micro-arrays)/Si/Al devices compared to the other fabricated devices is observed, as portrayed in Fig. 8c. Besides, Fig. 8d shows a comparison of the performance of the three devices at a 30 mW incident power. A remarkable increment in the  $I_{ph}$  and the  $V_{oc}$  is observed for the devices with the Au/PEDOT:PSS/(Si + PSi micro-arrays)/Si/Al structure.

**3.4.2 Energy band diagrams.** The specific optoelectronic operation mechanisms of the photodetectors can be further analyzed from the energy band diagrams. Fig. 9a illustrates the energy band diagram that we proposed for the Au/PEDOT:PSS/Si/Al photodetectors. The lowest unoccupied molecular orbital (LUMO) and the highest occupied molecular orbital (HOMO) of PEDOT:PSS are estimated to be 3.5 and 5.0 eV, respectively.<sup>16</sup> As for silicon, the conduction band minimum (CB) and valence band maximum (VB) levels are reported to be 4.05 and 5.15 eV, respectively.<sup>33</sup> The PEDOT:PSS and Si junction results in a small valence band offset ( $\Delta E_v = 0.15$  eV) and a higher conduction band offset ( $\Delta E_c = 0.55$  eV). Upon illumination with light of energy greater than the bandgap energy of Si, absorption of photons would result in the generation of electron-hole pairs that will move in opposite directions. While PEDOT:PSS is a p-type semiconductor with high electrical conduction, it is not considered to be responsible for the generation of photocarriers when exposed to light,<sup>11</sup> as charge carriers are strongly bound. For this reason, PEDOT:PSS is considered to act as a hole transport and electron blocking layer due to its hole selective conductivity.<sup>34,35</sup> Accordingly, photocarriers will be mainly generated in Si.<sup>12</sup> Electrons will drift to the Si side (Al contact), whereas holes will drift to the PEDOT:PSS side (Au contact), and both charge carriers contribute to the total photocurrent.

Fig. 9b shows the proposed energy band diagram of the Au/PEDOT:PSS/PSi/Si/Al photodetectors. The Fermi level for the PSi layer is located close to the middle of the energy gap. This assumption is a consequence of the formation of the nanopores at the dopant sites of Si,<sup>17</sup> which leads to a widening of the energy bandgap of PSi with respect to that of Si (1.12 eV). Under illumination, the generated photocurrent follows the same mechanism as in the Au/PEDOT:PSS/Si/Al devices. Besides, the increase in the number of generated carriers at high irradiation intensities is attributed to the optical absorption enhancement provided by the PSi layer. However, the decrease



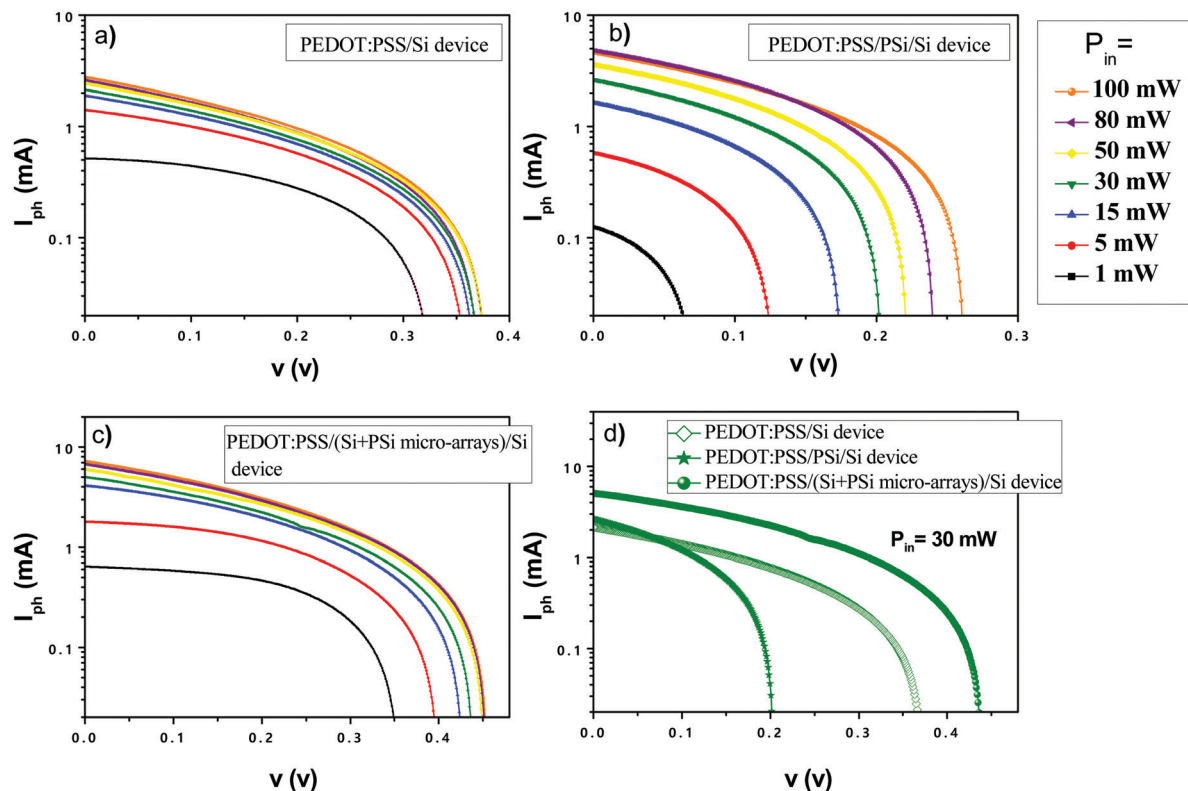


Fig. 8 I-V curves of the three photodetectors under different  $P_{in}$  and at 0 V bias. (a) Au/PEDOT:PSS/Si/Al devices, (b) Au/PEDOT:PSS/PSi/Si/Al devices, and (c) Au/PEDOT:PSS/(Si+PSi micro-arrays)/Si/Al devices. (d) Comparison between the I-V curves for the three photodetectors at  $P_{in} = 30$  mW.

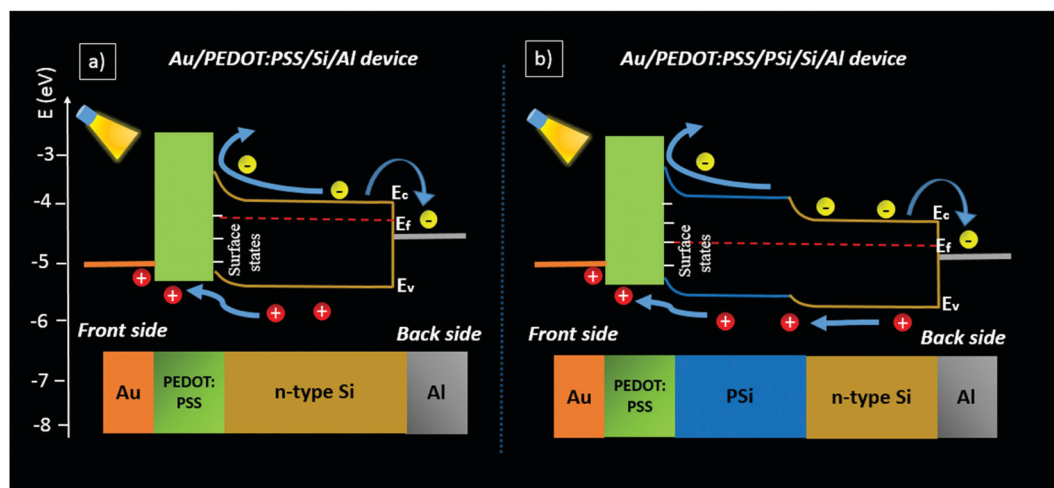


Fig. 9 Proposed energy band diagram for, (a) Au/PEDOT:PSS/Si/Al devices, and (b) Au/PEDOT:PSS/PSi/Si/Al devices.

in the  $V_{oc}$  and  $I_{ph}$  at low intensities is related to the low electrical conductivity of the PSi layer, leading to lower mobility and transport.<sup>36</sup> Also, the surface states between PSi and the PEDOT:PSS layer increase.

As for the Au/PEDOT:PSS/(Si + PSi micro-arrays)/Si/Al photodetectors, their electrical behavior can be considered as a parallel combination of the electrical conduction mechanisms previously

discussed for the Au/PEDOT:PSS/Si/Al and Au/PEDOT:PSS/PSi/Si/Al devices. As a consequence of the combination of the two conduction mechanisms,  $I_{ph}$  and  $V_{oc}$  were greatly enhanced over a wide range of light irradiation levels.

**3.4.3 Time-dependent photoresponse analysis.** Repeatability and reproducibility of the electrical response of photodetectors to pulsed light can be determined from current-time ( $I-t$ ) curves.

Fig. 10a–c show that the self-powered photodetectors show a rapid response when light is switched on, and the photocurrent drops back to zero when it is switched off. Furthermore, it can be observed that the photodetectors show an excellent repeatability and reproducibility to pulsed light over a wide range of irradiation powers since the output signal remains the same over a large number of cycles. Fig. 10 shows how the photocurrent increases for the three devices when the incident power increases. More specifically, the Au/PEDOT:PSS/(Si + PSi micro-arrays)/Si/Al devices show the highest photocurrent values. As discussed above, this result is attributed to the reduction of

reflectance of the active layer due to the presence of PSi and limited electrical conduction losses. The large difference between the dark current and the photocurrent for the three devices indicates that the photodetectors have excellent sensitivity to incident light in a wide range of light intensities (from 100  $\mu\text{W}$  to 100 mW). For instance, at 0 V bias and under 30 mW incident power, the current of the Au/PEDOT:PSS/Si/Al, Au/PEDOT:PSS/PSi/Al and Au/PEDOT:PSS/PSi micro-arrays/Al devices increased dramatically from  $9.3 \times 10^{-4}$ ,  $2.67 \times 10^{-4}$  and  $8.18 \times 10^{-4}$  mA in the dark state to 2.13, 2.5 and 5.17 mA, respectively. Accordingly, the current ratio ( $I_{\text{on}}/I_{\text{off}}$ ) is around  $10^4$ .

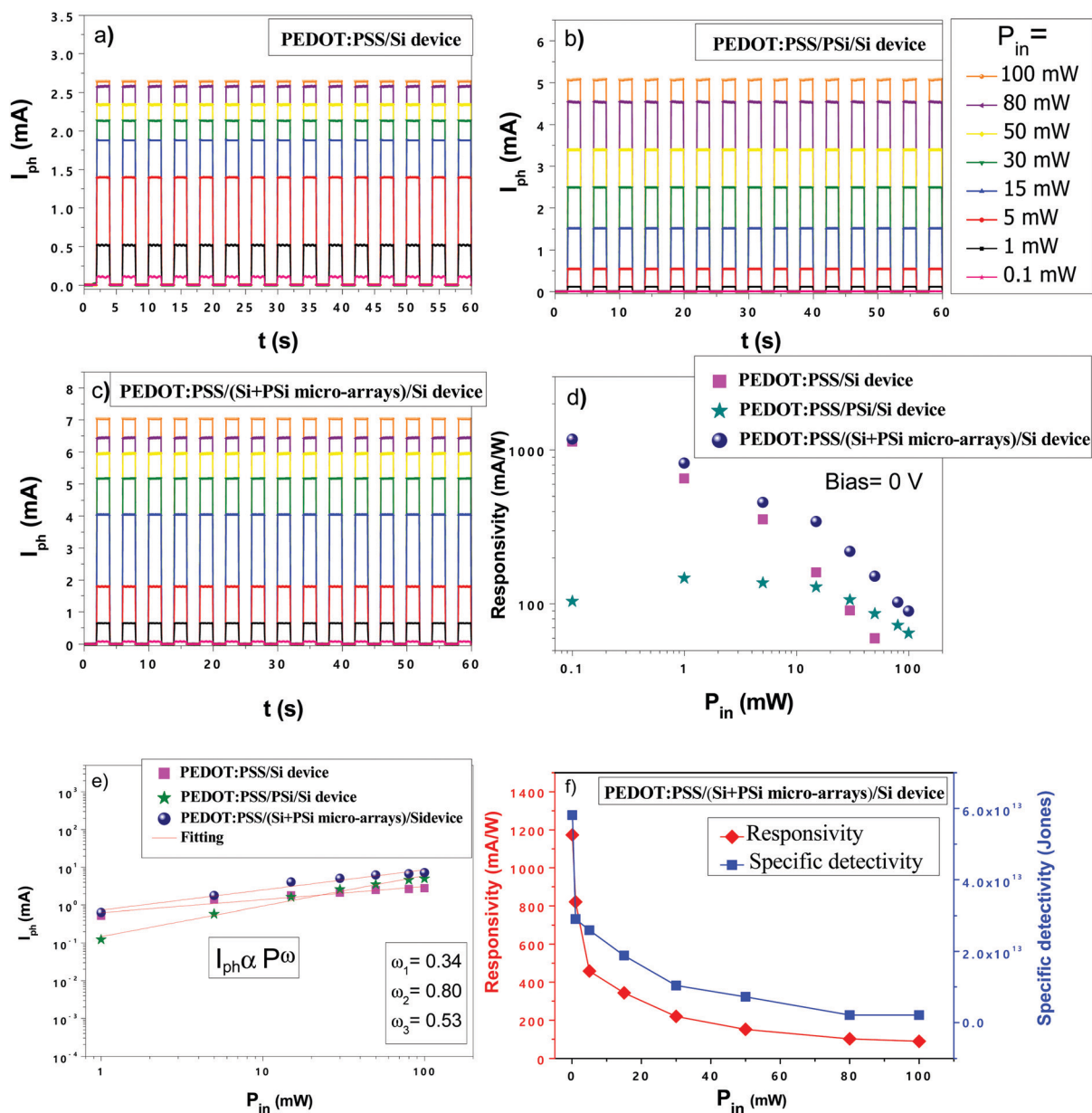


Fig. 10 Time-dependent photo-response ( $I-t$ ) curves measured under irradiation with different  $P_{\text{in}}$  (a) corresponding to Au/PEDOT:PSS/Si/Al photodetectors, (b) corresponding to Au/PEDOT:PSS/PSi/Si/Al photodetectors and (c) corresponding to Au/PEDOT:PSS/(Si + PSi micro-arrays)/Si/Al photodetectors. (d) The dependence of responsivity of the three photodetectors on  $P_{\text{in}}$  at 0 V bias. (e) Logarithmic plot of  $I_{\text{ph}}$  versus  $P_{\text{in}}$  at 0 V bias. (f) The dependence of responsivity and specific detectivity of the Au/PEDOT:PSS/(Si + PSi micro-arrays)/Si/Al photodetectors on  $P_{\text{in}}$ .

Fig. 10d shows the dependence of the responsivity on the power of the incident light. This value can be calculated from the following equation:<sup>14</sup>

$$\text{Responsivity} = \frac{(I_{\text{ph}} - I_{\text{d}})}{P_{\text{in}} \cdot S} \quad (2)$$

where  $I_{\text{ph}}$  is the photocurrent,  $I_{\text{d}}$  is the dark current,  $P_{\text{in}}$  is the incident power density and  $S$  is the active area of the photodetectors (0.785 cm<sup>2</sup> in our case). According to our results shown in Fig. 10d, the Au/PEDOT:PSS/Si/Al devices show high values of responsivity at low irradiation levels, while the Au/PEDOT:PSS/PSi/Si/Al devices show higher values under high levels of irradiation. As for Au/PEDOT:PSS/(Si + PSi micro-arrays)/Si/Al photodetectors, the experimental results confirm a remarkable performance in a wide range of incident powers. For instance, at a low incident power of 100  $\mu\text{W}$ , the responsivity values are 1130.14, 103.60 and 1172.87 mA W<sup>-1</sup> for the Au/PEDOT:PSS/Si/Al, Au/PEDOT:PSS/PSi/Si/Al and Au/PEDOT:PSS/(Si + PSi micro-arrays)/Si/Al devices, respectively. While at high intensity of 100 mW, the responsivity values are 33.61, 64.51 and 89.50 mA W<sup>-1</sup>, respectively (Fig. 10d). From this perspective, the integration between PSi and Si micro-nanostructures results in a remarkable improvement in the optoelectronic response of the photovoltaic photodetectors.

As a consequence of the sensitivity of the photodetectors to the optical signals, additional photoresponse analysis was carried out. Fig. 10e shows the dependence of  $I_{\text{ph}}$  on  $P_{\text{in}}$ , which can be fitted to the following power law:<sup>14</sup>

$$I_{\text{ph}} = A \cdot P_{\text{in}}^{\omega} \quad (3)$$

where  $I_{\text{ph}}$  and  $P_{\text{in}}$  are the photocurrent and the incident light power, respectively,  $A$  is a proportional constant and  $\omega$  is a factor related to the generation and recombination processes in the active layer of the photodetectors.<sup>37</sup> A value of 1 indicates ideal generation of electron-hole pairs. By fitting the data in Fig. 10e to eqn (3), the values of  $\omega$  were found to be 0.34, 0.80 and 0.53 for Au/PEDOT:PSS/Si/Al, Au/PEDOT:PSS/PSi/Si/Al and Au/PEDOT:PSS/(Si + PSi micro-arrays)/Si/Al, respectively. Lower values of  $\omega$  are attributed to carrier recombination due to the presence of defects in the active layer. The highest value corresponds to the Au/PEDOT:PSS/PSi/Si/Al devices, which might be attributed to the dramatic degradation in  $I_{\text{ph}}$  with the reduction of  $P_{\text{in}}$ . This behavior leads to a relation between  $I_{\text{ph}}$  and  $P_{\text{in}}$  close to unity.

The ability of the photodetectors to detect small light signals is a parameter defined by the specific detectivity ( $D^*$ ).  $D^*$  can be calculated by the following equation:<sup>14</sup>

$$D^* = \text{Responsivity} \cdot \sqrt{\frac{A}{(2 \cdot q \cdot I_{\text{d}})}}$$

where  $A$  is the total area of the device (0.785 cm<sup>2</sup> in this work),  $q$  is the elementary charge ( $1.602 \times 10^{-19}$  C) and  $I_{\text{d}}$  is the dark current. Fig. 10f reveals the remarkable efficiency (responsivity and detectivity) of the complementary Au/PEDOT:PSS/(Si + PSi

micro-arrays)/Si/Al devices in a wide range of incident light powers.

It is important to determine the response speed of the photodetectors since it reflects the ability of the device to respond to fast switching optical signals. Fig. 11a–c show the on/off response speed of the Au/PEDOT:PSS/Si/Al, Au/PEDOT:PSS/PSi/Si/Al and Au/PEDOT:PSS/(Si + PSi micro-arrays)/Si/Al photodetectors, respectively. The analysis was carried out by switching 400  $\mu\text{W}$  white light every 2 ms at 50 Hz and 0 V bias. The table in Fig. 11d presents a comparison of the rise ( $t_{\text{r}}$ ) and fall times ( $t_{\text{f}}$ ) for the three detectors. It can be seen that the three devices have the ability to respond to fast light switching with excellent reproducibility and stability. It is also observed that the Au/PEDOT:PSS/Si/Al photodetectors exhibit the fastest response (shorter than 217  $\mu\text{s}$ /387  $\mu\text{s}$  respectively). This behavior is probably due to the small amount of defects in the Si surface, *i.e.*, the active layer, compared with an active layer composed of PSi. Since PSi causes an increase in the number of surface states as demonstrated in the energy band diagrams (Fig. 9). Thus, the surface states increase the rate of carrier recombination, which hinders the response speed of the photodetectors.

Table 2 shows a comparison between the obtained characteristic parameters for the modified devices with previously reported values. The comparison is for photodetectors based on the same materials (Si nanostructures or/and PEDOT:PSS thin films). The results show how the combination of silicon and PSi on the same surface can be an ideal strategy to improve the photovoltaic response of self-powered photodetectors in a wide range of incident powers.

**3.4.4 Spectral responsivity.** Fig. 12a shows the spectral responsivity of the photodetectors in the 300 to 1200 nm wavelength range and at 0 V bias. The experimental results show that the photoresponse spectrum of the Au/PEDOT:PSS/Si/Al devices shows a wideband response in the visible and near-infrared regions, although responsivity diminishes for wavelengths over 1000 nm. This behavior is attributed to the use of radiation with photon energy less than the energy bandgap of the active layer, *i.e.*, Si ( $\sim$ around 1110 nm),<sup>33</sup> resulting in reduced absorption. The spectral responsivity of the Au/PEDOT:PSS/PSi/Si/Al photodetectors is larger in the near-infrared region than in the visible region, which is attributed to the lower transparency and higher dispersion of PSi in the visible region. However, the overall responsivity is noticeably lower, which is attributed to two main reasons. (1) The reduction in the electrical conductivity associated with the presence of a PSi layer. (2) The increase in the surface-to-volume ratio of the PSi layer, which results in increased electron-hole recombination rates. Fig. 12a shows that the maximum responsivity for the Au/PEDOT:PSS/PSi/Si/Al photodetectors is 265.56 mA W<sup>-1</sup> at 1007 nm. This wavelength corresponds to a photon energy of 1.24 eV, which is assumed to be the energy bandgap of the PSi layer. The increase in the energy bandgap values of PSi compared to the bulk Si wafer (1.12 eV) is considered to be a manifestation of quantum confinement effects.<sup>18,19</sup> A similar behavior was previously found for PSi-based photodetectors with a peak responsivity

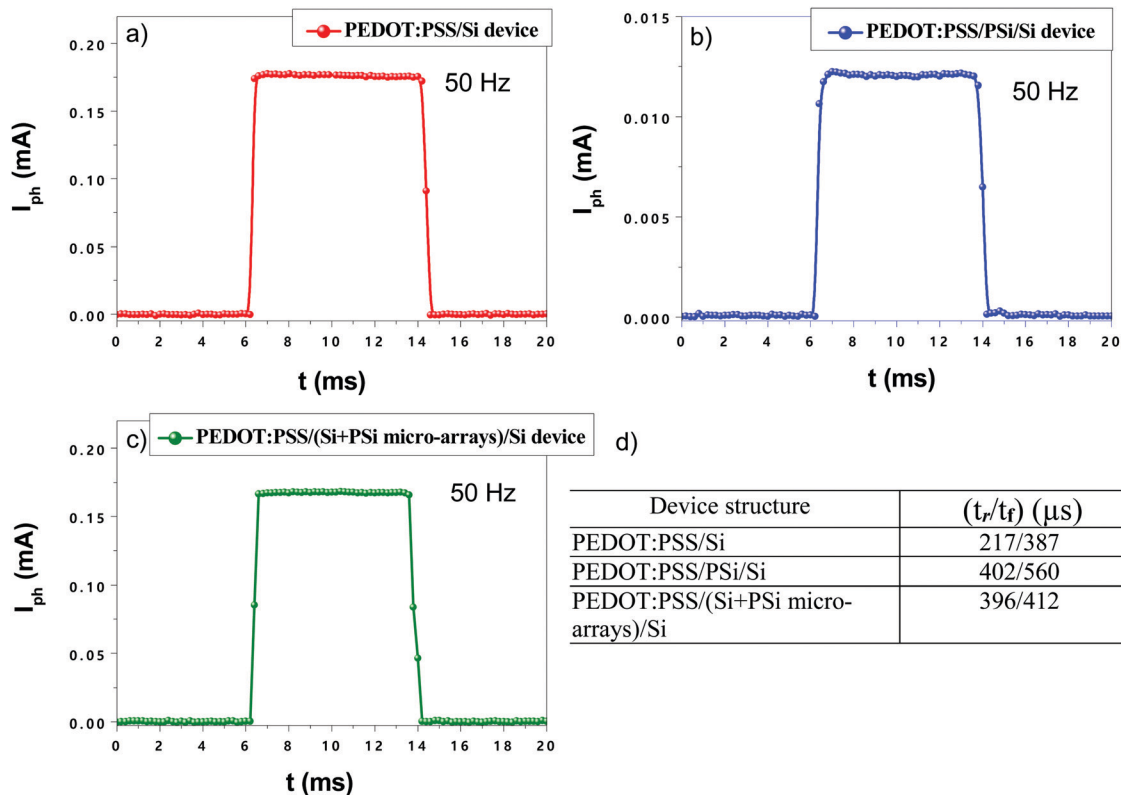


Fig. 11 The response speed of the photodetectors under fast switching ( $400 \mu\text{W}$ ) at 50 Hz and 0 V bias. (a) Response speed of Au/PEDOT:PSS/Si/Al photodetectors, (b) response speed of Au/PEDOT:PSS/PSi/Si/Al photodetectors, and (c) response speed of Au/PEDOT:PSS/(Si + PSi micro-arrays)/Si/Al photodetectors. (d) The obtained values of rise time and fall time of the three photodetectors.

of  $77 \text{ mA W}^{-1}$  at 780 nm, where the diameter of the pores was around 12 nm.<sup>43</sup>

The Au/PEDOT:PSS/(Si + PSi micro-arrays)/Si/Al photodetectors show an improved performance over a broad range of optical spectrum. This behavior is ascribed to two main reasons. First, an optical enhancement in the visible and near-infrared regions due to the presence of a thin layer of PSi in the micro-arrays. Second, an improvement in the electrical conduction associated with the presence of heavily-doped Si regions in the active layer. In this case two parallel conduction mechanisms contribute to the generation of photocarriers. The first generation path is through the PEDOT:PSS/PSi/Si interfaces and the second

occurs through the PEDOT:PSS/Si interface. As such, the output photocurrent is enhanced in all wavelength ranges. Besides, the remarkable enhancement observed in Fig. 8 and 10 confirms the extraordinary sensitivity of the Au/PEDOT:PSS/(Si + PSi micro-arrays)/Si/Al photodetectors to white light in a wide range of incident light powers.

Fig. 12b demonstrates an effective photoresponse of the self-powered photodetectors to monochromatic light of different wavelengths. The modified Au/PEDOT:PSS/PSi/Si/Al photodetectors outperform the Au/PEDOT:PSS/Si/Al devices in the infrared region and *vice versa* in the UV-visible regions. Furthermore, the Au/PEDOT:PSS/(Si + PSi micro-arrays)/Si/Al photodetectors

Table 2 Comparison of the device performances of some reported photodetectors based on Si nanostructures or/and PEDOT:PSS thin films

Device structure	Bias (V)	Responsivity ( $\text{mA W}^{-1}$ )	$D^*$ (Jones)	Rise/fall time ( $\mu\text{s}$ )	Ref.
CuO/Si nanowire arrays	0	0.389 @ 405 nm	$3.00 \times 10^9$	60/80 @1000 Hz	38
ZnO nanostructure array/PSi	3	1980 @ 325 nm	...	86 000/83 000	39
$\text{CH}_3\text{NH}_3\text{PbI}_3$ thin films/PSi pillar array	0	8.13 @ 780 nm	$0.974 \times 10^{13}$	253.3/230.4 @ 800 Hz	14
PEDOT:PSS/ SnO <sub>2</sub> microwires	0	18.2 @ 450 nm	...	...	10
PEDOT:PSS/single Se microtube	0	5.5 @ 610 nm	$1.76 \times 10^{10}$	1000/9780	40
ZnO/PEDOT:PSS	1	13 @ 380 nm	...	270 000/280 000 @ 0.5 Hz	41
(PEDOT:PSS)/Ga <sub>2</sub> O <sub>3</sub>	0	37.4 @ 254 nm	$9.2 \times 10^{12}$	3.3/71.2	11
Graphene/ PEDOT:PSS	0	160 @ 500 nm	$1.33 \times 10^{12}$	...	42
PEDOT:PSS/Si nanowire arrays (820 nm length)	0	37.8 @ 920 nm	$4.1 \times 10^{11}$	3.17/55.4 @ 1000 Hz	12
PEDOT:PSS/(Si + PSi micro-arrays)	0	1172.8 @ white light	$5.81 \times 10^{13}$	396/412 @ 50 Hz	Present work

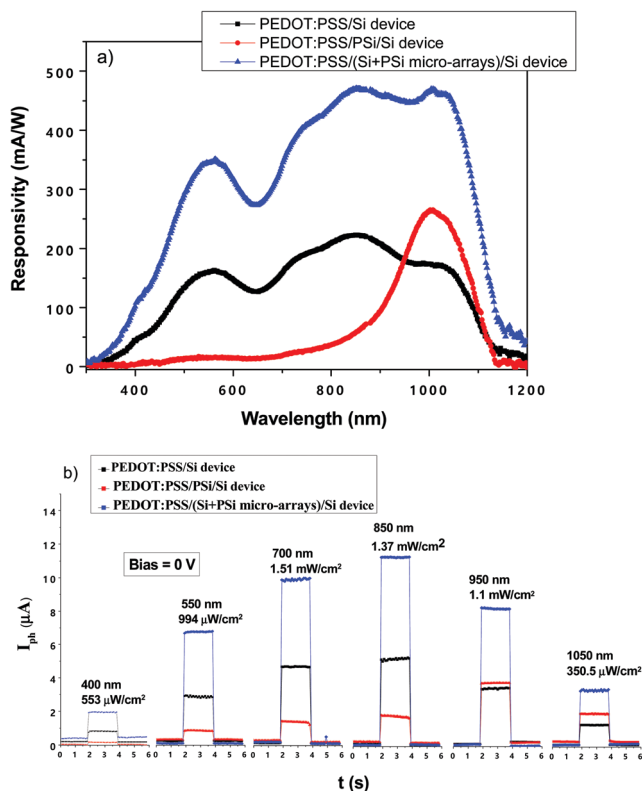


Fig. 12 (a) The spectral responsivity of the three photodetectors in the wavelength range of 300 to 1200 nm at 0 V bias. (b)  $I-t$  curves of the three devices under irradiation with different intensities of monochromatic light at 0 V bias.

always show the best photoresponse in the near-UV to the IR regions.

## 4. Conclusions

The main aim of the current work was to develop highly-stable, reliable, high-efficiency, and fast response broadband self-powered photodetectors. We have investigated three different device configurations of hybrid organic-inorganic photodetectors, namely Au/PEDOT:PSS/Si/Al, Au/PEDOT:PSS/PSi/Si/Al, and Au/PEDOT:PSS/(Si + PSi micro-array)/Si/Al. The structural modifications introduced on the surface of Si have a notable effect on the reflectance, electrical conduction, and photoresponse of the photodetectors. The specific mechanism of photo-carrier generation was studied, and energy band diagrams for the devices were proposed.

It is worth pointing out that the average reflectance in the 250–900 nm wavelength range of the Si + PSi micro-arrays is higher than that of the PSi layer. Besides, the etching of a PSi layer leads to a reduction in the electrical conduction. Meanwhile, the integrated structure of Si + PSi micro-arrays provides dark current values close to those for the devices based on flat Si.

The experimental results reveal that the three configurations exhibit excellent stability and reproducibility over a wide range

of incident light powers. However, the Au/PEDOT:PSS/Si/Al devices show high values of responsivity at low irradiation levels, while the Au/PEDOT:PSS/PSi/Si/Al devices show high values under high levels of irradiation. As for Au/PEDOT:PSS/(Si + PSi micro-array)/Si/Al photodetectors, an outstanding performance over a wide range of incident powers was demonstrated.

As for the spectral responsivity, the Au/PEDOT:PSS/Si/Al devices show a wideband response in the visible and near-infrared regions. The Au/PEDOT:PSS/PSi/Si/Al devices show a narrowband response in the near-infrared region which is attributed to the morphology of the PSi layers. The Au/PEDOT:PSS/(Si + PSi micro-array)/Si/Al photodetectors show a remarkable performance over a broad wavelength range of the optical spectrum. As such, the combination of Si and PSi on the same surface can be an ideal strategy to obtain tunability of the optical behavior of PSi and the rather large electrical conduction of highly-doped Si in the same device, leading to highly-efficient photonic devices.

## Author contributions

Conceptualization (R. Ramadan and R. J. Martín-Palma), formal analysis (R. Ramadan, V. Torres-Costa and R. J. Martín-Palma), funding acquisition (R. Ramadan, V. Torres-Costa and R. J. Martín-Palma), investigation (R. Ramadan, V. Torres-Costa and R. J. Martín-Palma), methodology (R. Ramadan), project administration (R. J. Martín-Palma), supervision (R. J. Martín-Palma), validation (R. Ramadan, V. Torres-Costa and R. J. Martín-Palma), visualization (R. Ramadan), writing – original draft (R. Ramadan), and writing – review & editing (R. Ramadan, V. Torres-Costa and R. J. Martín-Palma).

## Funding

This research was partially funded by the Universidad Autónoma de Madrid, FPI-UAM grant and by the Egyptian Ministry of Higher Education, Missions Section under Egyptian Joint Supervision Grant. This work was part of ATTRACT that has received funding from the European Union's Horizon 2020 Research and Innovation Programme.

## Conflicts of interest

The authors declare no conflict of interest.

## Acknowledgements

The authors are thankful to Mr Luis García Pelayo and Dr Valentin Cconstantin Nistor for their technical support.

## References

- 1 H. S. Nalwa, *Photodetectors and fiber optics*, Elsevier, 2012.
- 2 W. Tian, H. Zhou and L. Li, *Small*, 2017, **13**, 1702107.
- 3 M. Ahmadi, T. Wu and B. Hu, *Adv. Mater.*, 2017, **29**, 1605242.

- 4 Y. Zhao, C. Li and L. Shen, *InfoMat*, 2019, **1**, 164.
- 5 J. Zhou and J. Huang, *Adv. Sci.*, 2018, **5**, 1700256.
- 6 X. Wang, W. Song, B. Liu, G. Chen, D. Chen, C. Zhou and G. Shen, *Adv. Funct. Mater.*, 2013, **23**, 1202.
- 7 L. Li, F. Zhang, W. Wang, Q. An, J. Wang, Q. Sun and M. Zhang, *ACS Appl. Mater. Interfaces*, 2015, **7**, 5890.
- 8 M. Kielar, O. Dhez, G. Pecastaings, A. Curutchet and L. Hirsch, *Sci. Rep.*, 2016, **6**, 39201.
- 9 B. Friedel, P. E. Keivanidis, T. J. Brenner, A. Abrusci, C. R. McNeill, R. H. Friend and N. C. Greenham, *Macromolecules*, 2009, **42**, 6741.
- 10 S. Li, S. Wang, K. Liu, N. Zhang, Z. Zhong, H. Long and G. Fang, *Appl. Phys. A: Mater. Sci. Process.*, 2015, **119**, 1561.
- 11 S. Li, Z. Yan, Z. Liu, J. Chen, Y. Zhi, D. Guo, P. Li, Z. Wu and W. Tang, *J. Mater. Chem. C*, 2020, **8**, 1292.
- 12 Z. Liang, P. Zeng, P. Liu, C. Zhao, W. Xie and W. Mai, *ACS Appl. Mater. Interfaces*, 2016, **8**, 19158.
- 13 J. A. Nelson, *The physics of solar cells*, World Scientific Publishing Company, 2003.
- 14 Y. Cheng, Z. Shi, S. Yin, Y. Li, S. Li, W. Liang, D. Wu, Y. Tian and X. Li, *Sol. Energy Mater. Sol. Cells*, 2020, **204**, 110230.
- 15 D. Samajdar, *Sol. Energy*, 2019, **190**, 278.
- 16 W. Chen, P. Gao, L. Zhou, L.-H. Shi, D.-W. Wang, R. Hao, J. Ye, W.-Y. Yin and E. Li, *IEEE J. Photovolt.*, 2018, **8**, 757.
- 17 D. H. Shin, J. H. Kim, J. H. Kim, C. W. Jang, S. W. Seo, H. S. Lee, S. Kim and S.-H. Choi, *J. Alloys Compd.*, 2017, **715**, 291.
- 18 R. Martín-Palma, L. Pascual, P. Herrero and J. Martínez-Duart, *Appl. Phys. Lett.*, 2002, **81**, 25.
- 19 R. Martín-Palma, L. Pascual, P. Herrero and J. Martínez-Duart, *Appl. Phys. Lett.*, 2005, **87**, 211906.
- 20 J. P. Thomas and K. T. Leung, *Adv. Funct. Mater.*, 2014, **24**, 4978.
- 21 R. J. Martín-Palma, P. D. McAtee, R. Ramadan and A. Lakhtakia, *Sci. Rep.*, 2019, **9**, 7291.
- 22 R. Ramadan, M. Manso-Silván and R. J. Martín-Palma, *J. Mater. Sci.*, 2020, **55**, 5458.
- 23 R. J. Martín-Palma, P. D. McAtee, R. Ramadan and A. Lakhtakia, *Sci. Rep.*, 2019, **9**, 1.
- 24 I. Sagnes, A. Halimaoui, G. Vincent and P. Badoz, *Appl. Phys. Lett.*, 1993, **62**, 1155.
- 25 V. Torres-Costa and R. Martín-Palma, *J. Mater. Sci.*, 2010, **45**, 2823.
- 26 R. C. Anderson, R. S. Muller and C. W. Tobias, *J. Electrochem. Soc.*, 1991, **138**, 3406.
- 27 R. Ramadan and R. J. Martín-Palma, *Energies*, 2020, **13**, 2165.
- 28 J. P. Thomas and K. T. Leung, *J. Mater. Chem. A*, 2016, **4**, 17537.
- 29 M. E. Orazem and B. Tribollet, *Electrochemical impedance spectroscopy*, John Wiley & Sons, 2017.
- 30 D. Ribeiro, C. Souza and J. Abrantes, *Rev. IBRACON Estrut. Mater.*, 2015, **8**, 529.
- 31 F. Scholze, H. Rabus and G. Ulm, *J. Appl. Phys.*, 1998, **84**, 2926.
- 32 W. Ouyang, F. Teng, J. H. He and X. Fang, *Adv. Funct. Mater.*, 2019, **29**, 1807672.
- 33 J. Nelson, *The physics of solar cells*, World Scientific Publishing Company, 2003.
- 34 M. Yi, S. Hong, J.-R. Kim, H. Kang, J. Lee, K. Yu, S. Kee, W. Lee and K. Lee, *Sol. Energy Mater. Sol. Cells*, 2016, **153**, 117.
- 35 S. Rafique, S. M. Abdullah, M. M. Shahid, M. O. Ansari and K. Sulaiman, *Sci. Rep.*, 2017, **7**, 39555.
- 36 H. Zhang, C. Wang, W. Peng, C. Yang and X. Zhong, *Nano Energy*, 2016, **23**, 60.
- 37 Y. Li, Z. Shi, L. Lei, Z. Ma, F. Zhang, S. Li, D. Wu, T. Xu, X. Li and C. Shan, *ACS Photonics*, 2018, **5**, 2524.
- 38 Q. Hong, Y. Cao, J. Xu, H. Lu, J. He and J.-L. Sun, *ACS Appl. Mater. Interfaces*, 2014, **6**, 20887.
- 39 R. Dalvand, S. Mahmud and R. Shabannia, *J. Mater. Sci.: Mater. Electron.*, 2018, **29**, 4999.
- 40 P. Yu, K. Hu, H. Chen, L. Zheng and X. Fang, *Adv. Funct. Mater.*, 2017, **27**, 1703166.
- 41 N. Hernandez-Como, G. Rivas-Montes, F. Hernandez-Cuevas, I. Mejia, J. Molinar-Solis and M. Aleman, *Mater. Sci. Semicond. Process.*, 2015, **37**, 14.
- 42 Z. Liu, K. Parvez, R. Li, R. Dong, X. Feng and K. Müllen, *Adv. Mater.*, 2015, **27**, 669.
- 43 K.-H. Wu, C.-W. Li and J.-H. Liu, *Microelectron. Eng.*, 2015, **148**, 70.

## Abbreviations in chapter 6

PEDOT:PSS	<b>poly(3,4- ethylenedioxythiophene) polystyrene sulfonate</b>
PSi	<b>porous Silicon</b>
P <sub>3</sub> HT	Poly(3-hexylthiophene)
PC <sub>61</sub> BM	Phenyl-C <sub>61</sub> -butyric acid methyl ester
RTP	Rapid thermal processing
IPA	Isopropyl alcohol
DMSO	Dimethylsulfoxide
FESEM	Field emission scanning electron microscope
R <sub>av</sub>	average reflectance
I-t	Time-dependent current
I <sub>ph</sub>	Photocurrent
LUMO	Lowest unoccupied molecular orbital
HOMO	Highest occupied molecular orbital
CB	Conduction band minimum
VB	Valence band maximum
M	Potential constant
$\omega$	Factor related to generation and recombination processes
D*	Specific detectivity
t <sub>r</sub>	Rise time
t <sub>f</sub>	Fall time

## General conclusions

The mechanism behind the enhancement of the optoelectronic properties of photonic devices based on nanostructures depends on their type, shape, density and size. This work deals with the performance of hybrid nanostructures for the development of solar cells and self-powered broadband photodetectors. It was studied the effect of two different hybrid nanostructures. Firstly, hybrid nanostructure of silver nanoparticles (AgNPs) combined with nanostructured porous silicon (nanoPS) for the development of Schottky junction solar cells. Furthermore, hybrid organic-inorganic nanostructures of PEDOT:PSS as an organic layer and nanoPS micro-arrays as the inorganic layer for the development of self-powered broadband photodetectors.

**Chapter 2:** The characteristic features of the electrochemically infiltrated AgNPs in nanoPS layers can be easily optimized by setting the appropriate electrolyte pH value and infiltration current density. From the experimental results, the size of the infiltrated AgNPs decreases upon the reduction in the electrolyte acidity as well as upon increasing the infiltration current density. Additionally, the overall optical reflectance of the hybrid nanoPS+AgNPs structures was studied as a function of the AgNPs fabrication parameters (electrolyte pH values and infiltration current densities). nanoPS layers effectively reduce the overall reflectance of bulk silicon. The reflectance of the hybrid nanoPS+AgNPs structures can be lower than that of nanoPS due to plasmonic effects or higher if a continuous Ag layer is formed.

**Chapter 3:** The reflection and absorption characteristics as functions of the wavelength, angle of incidence, and polarization state of incident light were studied for nanoPS and the hybrid nanoPS+AgNPs layers. Absorption characteristics of the hybrid nanoPS+AgNPs layers can be controlled by selecting the appropriate combination of thickness and porosity of the nanoPS layers, together with the density of infiltrated silver nanoparticles. The wideband optical absorption characteristics of the hybrid nanoPS+AgNPs layers are expected to contribute to increased efficiency of light-harvesting devices and photodetectors given by increased field-of-view for both *s*- and *p*-polarization states of incident light over a broad spectral regime.

**Chapter 4:** The electrical conduction properties of three different metal-insulator-semiconductor (MIS) Schottky barrier diodes based on Si, nanoPS, and nanoPS+AgNPs were



studied aiming at assessing their potential use as photovoltaic solar cells. The structures of the intended diodes are Al/Si/TiO<sub>2</sub>/NiCr, Al/Si/nanoPS/TiO<sub>2</sub>/NiCr and Al/Si/nanoPS+AgNPs/TiO<sub>2</sub>/NiCr. With this objective in mind, the AC and DC electrical conduction properties of the MIS Schottky barrier diodes were studied and analyzed in details. The AC electrical properties were determined using a combination of electrochemical impedance spectroscopy and capacitance-voltage measurements. The DC electrical properties were obtained from current-voltage measurements. In all, the electrical conduction properties of MIS Schottky barrier diodes with the structure Al/Si/TiO<sub>2</sub>/NiCr were improved by including two modifications to the initial design. Firstly, nanoPS layers resulted in improving the electrical behavior of the TiO<sub>2</sub>/NiCr interface. However, the presence of nanoPS layers leads to conduction losses at the Si/nanoPS/TiO<sub>2</sub> interfaces. To overcome this drawback, silver nanoparticles were infiltrated into the nanoPS layers, which led to a notable enhancement in the overall electrical conduction properties of the resulting Al/Si/nanoPS+AgNPs/TiO<sub>2</sub>/NiCr MIS Schottky barrier diodes.

**Chapter 5:** It was analyzed in detail the optoelectronic performance of the three different MIS Schottky junction solar cells, namely Al/Si/TiO<sub>2</sub>/Au, Al/Si/nanoPS/TiO<sub>2</sub>/Au and Al/Si/nanoPS+AgNPs/TiO<sub>2</sub>/Au. A remarkable improvement in the photovoltaic performance of the devices was found upon the addition of nanoPS and AgNPs. To understand the different photogeneration and conduction mechanisms, an energy band model was proposed for the different devices. The Al/Si/nanoPS+AgNPs/TiO<sub>2</sub>/Au devices show the best optoelectronic performance. This performance is attributed to five main factors: (1) Reduction in the recombination rates by improving surface passivation, (2) Improved light trapping by the use of TiO<sub>2</sub> thin film as antireflective coating, (3) Increased light absorption by the nanoPS layer, (4) SPR effects associated to the presence of AgNPs, and (5) Improved electrical conduction of the AL by the presence of AgNPs.

**Chapter 6:** Highly stable, reliable, high-efficiency, and fast response broadband self-powered photodetectors were developed by modifying the surface of the AL with hybrid nanostructures. Three different device configurations of hybrid organic-inorganic photodetectors, namely Au/PEDOT:PSS/Si/Al, Au/PEDOT:PSS/nanoPS/Si/Al, and Au/PEDOT:PSS/(Si+nanoPS micro-array)/Si/Al were investigated. The structural modifications introduced on the surface of Si have a notable effect on the reflectance, electrical conduction, and photoresponse of the

photodetectors. The specific mechanism of photo-carrier generation was studied, and energy band diagrams for the devices were proposed. The experimental results reveal that the three configurations exhibit excellent stability and reproducibility over a wide range of incident light powers. However, the Au/PEDOT:PSS/Si/Al devices show high values of responsivity at low irradiation levels, while the Au/PEDOT:PSS/nanoPS/Si/Al devices show high values under high levels of irradiation. As for Au/PEDOT:PSS/(Si+nanoPS micro-array)/Si/Al photodetectors, an outstanding performance over a wide range of incident powers was demonstrated. As for the spectral responsivity, the Au/PEDOT:PSS/Si/Al devices show a wideband response in the visible and near-infrared regions. The Au/PEDOT:PSS/nanoPS/Si/Al devices show a narrowband response in the near-infrared region which is attributed to the morphology of the nanoPS layers. The Au/PEDOT:PSS/(Si+nanoPS micro-array)/Si/Al photodetectors show a remarkable performance over a broad wavelength range of the optical spectrum. As such, the combination of Si and nanoPS on the same surface can be an ideal strategy to obtain in the same device the tunability of the optical behavior of nanoPS and the rather large electrical conduction of highly-doped Si, leading to highly efficient photonic devices.

## **Conclusiones generales**

El mecanismo responsable de la mejora de las propiedades optoelectrónicas de los dispositivos fotónicos basados en nanoestructuras depende de su tipo, forma, densidad y tamaño. Este trabajo se ha centrado en el estudio del rendimiento de nanoestructuras híbridas para el futuro desarrollo de células solares y fotodetectores de banda ancha autoalimentados. En particular, se ha estudiado el efecto de dos nanoestructuras híbridas diferentes. En primer lugar, la nanoestructura híbrida basada en nanopartículas de plata (AgNPs) combinada con silicio poroso nanoestructurado (nanoPS) para el desarrollo de células solares de unión Schottky. Por otra parte, se han analizado nanoestructuras híbridas orgánico-inorgánico, utilizando PEDOT:PSS para las capas orgánicas y micromatrices de nanoPS para las capas inorgánicas con el objetivo de desarrollar fotodetectores de banda ancha autoalimentados.

**Capítulo 2:** Los rasgos característicos de las nanopartículas de plata infiltradas electroquímicamente en las capas de nanoPS pueden optimizarse fácilmente ajustando los valores de pH del electrolito y de densidad de corriente de infiltración. A partir de los resultados experimentales, se ha determinado que el tamaño de las nanopartículas de plata infiltradas disminuye al reducir la acidez del electrolito, así como al aumentar la densidad de corriente de infiltración. Además, se estudió la reflectancia óptica global de las estructuras híbridas nanoPS+AgNPs en función de los parámetros de fabricación de las nanopartículas de plata (pH del electrolito y densidad de corriente de infiltración). Las capas de nanoPS reducen eficazmente la reflectancia global del silicio monocristalino. La reflectancia de las estructuras híbridas nanoPS+AgNPs puede ser menor que la del nanoPS debido a la aparición de efectos plasmónicos o mayor si se forma una capa continua de plata.

**Capítulo 3.** Se estudiaron los espectros de reflexión y absorción en función de la longitud de onda, el ángulo de incidencia y el estado de polarización de la luz incidente de diversas capas de nanoPS y estructuras híbridas nanoPS+AgNPs. El espectro de absorción de las estructuras híbridas de nanoPS+AgNPs pueden controlarse seleccionando la combinación adecuada de espesor y porosidad de las capas de nanoPS, junto con la densidad de las nanopartículas de plata infiltradas. Se espera que las propiedades de absorción óptica de banda ancha de las capas híbridas nanoPS+AgNPs contribuyan a aumentar la eficiencia de dispositivos de captación de

luz y fotodetectores gracias al aumento del campo de visión para los estados de polarización s y p de la luz incidente en un amplio régimen espectral.

**Capítulo 4.** Se han estudiado las propiedades de conducción eléctrica de tres diodos de barrera Schottky basados en Si, nanoPS y nanoPS+AgNPs con el fin de evaluar su posible utilización como células solares fotovoltaicas. Las estructuras de los diodos fabricados son Al/Si/TiO<sub>2</sub>/NiCr, Al/Si/nanoPS/TiO<sub>2</sub>/NiCr y Al/Si/nanoPS+AgNPs/TiO<sub>2</sub>/NiCr. Con este objetivo en mente, se estudiaron y analizaron en detalle las propiedades de conducción eléctrica (corriente alterna, CA y continua, CC) de dichos diodos de barrera Schottky. Las propiedades eléctricas en CA se determinaron mediante una combinación de espectroscopía de impedancia electroquímica y mediciones de capacidad-voltaje. Las propiedades eléctricas en CC se obtuvieron a partir de mediciones de corriente-voltaje. En conclusión, las propiedades de conducción eléctrica de los diodos de barrera Schottky metal-aislante-semiconductor con la estructura Al/Si/TiO<sub>2</sub>/NiCr se mejoraron al incluir dos modificaciones en el diseño inicial. En primer lugar, las capas de nanoPS llevaron a una mejora del comportamiento eléctrico de la intercara TiO<sub>2</sub>/NiCr. Sin embargo, la presencia de capas de nanoPS provoca pérdidas de conducción en las intercara Si/nanoPS/TiO<sub>2</sub>. Para superar este inconveniente, se infiltraron nanopartículas de plata dentro de las capas de nanoPS, lo que redundó en una notable mejora de las propiedades generales de conducción eléctrica de los diodos de barrera Schottky con la estructura Al/Si/nanoPS+AgNPs/TiO<sub>2</sub>/NiCr.

**Capítulo 5.** Se analizó en detalle el rendimiento optoelectrónico global de células solares de unión Schottky con tres estructuras diferentes, a saber, Al/Si/TiO<sub>2</sub>/Au, Al/Si/nanoPS/TiO<sub>2</sub>/Au y Al/Si/nanoPS+AgNPs/TiO<sub>2</sub>/Au. Se encontró una notable mejora en el rendimiento fotovoltaico de los dispositivos al añadir capas de nanoPS y nanopartículas de plata. Para entender los diferentes mecanismos de fotogeneración y conducción, se propusieron varios modelos de bandas para los diferentes dispositivos. Los dispositivos con la estructura Al/Si/nanoPS+AgNPs/TiO<sub>2</sub>/Au muestran el mejor rendimiento optoelectrónico. Este rendimiento se atribuye a cinco factores principales: (1) reducción de las tasas de recombinación mediante la mejora de la pasivación superficial, (2) mejora de la captación de la luz mediante el uso de una fina película de TiO<sub>2</sub> como recubrimiento antirreflectante, (3) aumento de la absorción de luz debido a la capa de nanoPS, (4) efectos de plasmón de superficie

asociados a la presencia de nanopartículas de plata y (5) mejora de la conducción eléctrica por la presencia de nanopartículas de plata en la capa activa.

**Capítulo 6.** Se desarrollaron fotodetectores autoalimentados de banda ancha altamente estables, fiables, de alta eficiencia y rápida respuesta, modificando la superficie de la capa activa con nanoestructuras híbridas. Se investigaron fotodetectores híbridos orgánico-inorgánicos con tres configuraciones diferentes: Au/PEDOT:PSS/Si/Al, Au/PEDOT:PSS/nanoPS/Si/Al y Au/PEDOT:PSS/(microarray de Si+nanoPS)/Si/Al. Las modificaciones estructurales introducidas en la superficie del silicio muestran un notable efecto sobre la reflectancia, la conducción eléctrica y la fotorrespuesta de los fotodetectores. Se estudió el mecanismo específico de generación de portadores fotogenerados y se propusieron diagramas de bandas de energía para los dispositivos. Los resultados experimentales revelan que las tres configuraciones presentan una excelente estabilidad y reproducibilidad en un amplio rango de potencias de luz incidente. Sin embargo, los dispositivos de Au/PEDOT:PSS/Si/Al muestran altos valores de responsividad a bajos niveles de irradiación, mientras que los dispositivos de Au/PEDOT:PSS/nanoPS/Si/Al muestran altos valores con elevados niveles de irradiación. En cuanto a los fotodetectores con la estructura Au/PEDOT:PSS/(microarray de Si+nanoPS)/Si/Al, se demostró un excelente rendimiento en un amplio rango de potencias de incidencia.

En lo referente a la respuesta espectral, los dispositivos Au/PEDOT:PSS/Si/Al muestran una respuesta de banda ancha en las regiones visible e infrarrojo cercano. Los dispositivos con la estructura Au/PEDOT:PSS/nanoPS/Si/Al muestran una respuesta de banda estrecha en la región del infrarrojo cercano que se atribuye a la morfología de las capas de nanoPS. Los fotodetectores con la estructura Au/PEDOT:PSS/(microarray de Si+nanoPS)/Si/Al muestran un notable rendimiento en un amplio rango de longitudes de onda del espectro óptico. Por ello, la combinación de Si y nanoPS en la misma superficie puede ser una estrategia ideal para obtener en el mismo dispositivo la posibilidad de sintonización del comportamiento óptico del nanoPS y la elevada conducción eléctrica del Si altamente dopado, dando lugar a dispositivos fotónicos de gran eficiencia.

## **Future investigation**

According to the detailed studies through this thesis, we obtained some ideas suitable for future investigation.

- 1- Since we were using highly resistive Si substrates ( $\rho=25-30 \Omega\cdot\text{cm}$ ) for the development of solar cells, the efficiency is quite low. we expect better photovoltaic parameters based on the same hybrid nanoPS+AgNPs nanostructures on Si ( $1-5 \Omega\cdot\text{cm}$ ). According to the previous optimization process for the most suitable resistivity of Si substrate for solar cells was e.g. Si ( $\rho=1-5 \Omega\cdot\text{cm}$ ).
- 2- As for the hybrid structures based on nanoPS micro-arrays, the micro-arrays pattern and the thickness of the nanoPS layer can be optimized. Different micropattern shapes with different ratios between the nanoPS and Si areas will be analyzed in the future studies.
- 3- As a consequence of the remarkable performance of photodetectors based on integrated micro-nanostructures on silicon substrates, we are intended to apply the integrated structure for flexible devices. Flexible photodetectors have received significant interest due to their small size, light weight and their potential use in portable and wearable optoelectronic devices. So, the combination between the optical and electrical properties of two different materials in one device will greatly improve the performance of the flexible optoelectronic devices.
- 4- Regarding the fabrication of flexible optoelectronic devices, there are many different materials that can be used, including organic and inorganic semiconductors. Among them, inorganic semiconductors exhibit superior stability and higher carrier mobility. Thus, the fabrication of thin or ultra thin micro-nanostructures based on inorganic semiconductors allows the development of bendable and conformally shaped optoelectronic devices. Materials like silicon, germanium, silicon carbide, gallium arsenide or metal oxides can be tested in a future study and integration between two different materials could remarkably improve the devices performance. Depending on the intended applications, the type, shape and size of the nanostructured materials can be selected.

## **List of publications in the Thesis**

- 1- R. Ramadan, R. J. Martín-Palma, Effect of electrolyte pH value and current density on the electrodeposition of silver nanoparticles into porous silicon, *Journal of Nanophotonics*, *14*(4), (2020), 040501.
- 2- R. J. Martín-Palma, P. D. McAtee, R. Ramadan, A. Lakhtakia, Hybrid nanostructured porous silicon-silver layers for wideband optical absorption, *Scientific reports*, *9*(1), (2019), 1-8.
- 3- R. Ramadan, R. J. Martín-Palma, Electrical characterization of MIS Schottky barrier diodes based on nanostructured porous silicon and silver nanoparticles with applications in solar cells, *Energies*, *13*(9), (2020), 2165.
- 4- R. Ramadan, M. Manso-Silván, R. J. Martín-Palma, Hybrid porous silicon/silver nanostructures for the development of enhanced photovoltaic devices, *Journal of Materials Science*, *55*(13), (2020), 5458-5470.
- 5- R. Ramadan, V. Torres-Costa, & R. J. Martín-Palma, Self-powered broadband hybrid organic–inorganic photodetectors based on PEDOT: PSS and silicon micro-nanostructures. *Journal of Materials Chemistry C*, *9*(13), (2021), 4682-4694.

## **Publications not included in the Thesis**

- 1- R. Ramadan, J.G. Simiz, M.D. Ynsa, M.M. Silván, Microwave plasma annealing of sol-gel deposited tantalum oxide and zinc oxide films, *Vacuum*, 149 (2018) 336-342.
- 2- R. Ramadan, D. Romera, R.D. Carrascón, M. Cantero, J.-J. Aguilera-Correa, J.P. Garcia Ruiz, J. Esteban, M.M. Silván, Sol-gel-deposited Ti-doped ZnO: Toward cell fouling transparent conductive oxides, *ACS omega*, 4 (2019) 11354-11363.
- 3- R. Ramadan, K. Abdel-Hady, M. Manso-Silván, V. Torres-Costa, R.J. Martín-Palma, Microwave plasma and rapid thermal processing of indium-tin oxide thin films for enhancing their performance as transparent electrodes, *Journal of Photonics for Energy*, 9 (2019) 034001.
- 4- R. Ramadan, R. Fernández-Ruiz, M. Manso Silván, Self-Organized In-Depth Gradients in Highly Ti-Doped ZnO Films: Thermal Versus MW Plasma Annealing, *Coatings*, 10 (2020) 418.
- 5- R. Ramadan, V. Torres-Costa, R.J. Martín-Palma, Fabrication of Zinc Oxide and Nanostructured Porous Silicon Composite Micropatterns on Silicon, *Coatings*, 10 (2020) 529.
- 6- R. Ramadan, C. Rodriguez, V. Torres-Costa, V. Pini, R.J.M. Palma, V. Cebrián, R.C. Membibre, O. Ahumada, M.M. Silván, Bringing immuno-assemblies to optoelectronics: sandwich assay integration of a nanostructured porous-silicon/gold-nanoparticle phototransistor, *Materials Science and Engineering: B*, 271 (2021) 115271.